IRRADIATION EFFECTS ON TITANIUM DIOXIDE ELECTRODES FOR LITHIUM ION BATTERIES

by

Kassiopeia Ann Smith

A dissertation

submitted in partial fulfillment

of the requirements for the degree of

Doctor of Philosophy in Materials Science and Engineering

Boise State University

August 2018

BOISE STATE UNIVERSITY GRADUATE COLLEGE

DEFENSE COMMITTEE AND FINAL READING APPROVALS

of the dissertation submitted by

Kassiopeia Ann Smith

Dissertation Title: Irradiation Effects on Titanium Dioxide Electrodes for Lithium Ion Batteries

Date of Final Oral Examination: 15 June 2018

The following individuals read and discussed the dissertation submitted by student Kassiopeia Ann Smith, and they evaluated her presentation and response to questions during the final oral examination. They found that the student passed the final oral examination.

Hui (Claire) Xiong, Ph.D.	Chair, Supervisory Committee
Janelle P. Wharry, Ph.D.	Member, Supervisory Committee
Darryl Butt, Ph.D.	Member, Supervisory Committee
Brian J. Jaques, Ph.D.	Member, Supervisory Committee

The final reading approval of the dissertation was granted by Hui (Claire) Xiong, Ph.D., Chair of the Supervisory Committee. The dissertation was approved by the Graduate College.

ACKNOWLEDGEMENTS

First, I would like to thank my undergraduate research advisor, Professor David Bahr, who allowed me to begin my research career before I even knew what it meant to be a scientist. With equal weight, I would also like to thank Professor Claire Xiong, and Professor Darryl Butt who accepted me into their groups at Boise State University and supported me through the transition from undergraduate to graduate research responsibilities. Specifically, I thank Claire for providing me many opportunities to develop professional and interpersonal skills throughout my graduate career. Her continued support has made this journey possible.

Furthermore, I would like to thank the rest of my committee, Dr. Janelle Wharry and Dr. Brian Jaques, for their guidance. I have been lucky enough to experience the rare circumstance that each person on my committee has been a true mentor. Thanks also to Dr. Karthik Chinnathambi and Dr. Dmitri Tenne who have provided significant insight and guidance. Finally, I thank the rest of the Electrochemical Energy Materials lab for their help and companionship, as well as all of the office staff because nothing would ever get done without them. I also would like to acknowledge the National Science Foundation (NSF) for the funding they provided for this research.

ABSTRACT

This dissertation presents the mechanisms of irradiation induced defects and the resulting electrochemical response of TiO_2 anode for lithium-ion-batteries. The objective is to realize pathways by which irradiation could be used to enhance the energy density of rechargeable lithium ion batteries in order to provide power to applications under extreme environments. Recent studies suggest that the presence of structural defects (e.g. vacancies and interstitials) in metal oxides may enhance the electrochemical charge storage capacity in electrode materials. One approach to induce defect formation in electrode materials is to use ion irradiation, which has been proven to produce point defects in a target material.

The effect of low energy proton irradiation, at both room temperature and 250˚C, on amorphous and anatase TiO_2 nanotube electrodes, as well as heavy-ion irradiation on single crystal TiO_2 is discussed. Nanotube electrodes, as well as lamella prepared from single crystal samples, were characterized with Raman spectroscopy and transmission electron microscopy to evaluate the structural phenomena that occur during irradiation. Furthermore, various electrochemical tests have been performed to study the irradiation response to lithiation after irradiation. It has been shown in this work that tailoring the defect density in metal oxides through ion irradiation presents new avenues for design of advanced electrode materials.

TABLE OF CONTENTS

LIST OF TABLES

LIST OF FIGURES

LIST OF ABBREVIATIONS

LIB	Lithium Ion Battery
EES	Electrochemical Energy Storage
mAh	milliamp-hour
TiO_2-NT	TiO_2 Nanotube
DPA	Displacements Per Atom
TEM	Transmission Electron Microscope
BF	Bright Field
RT	Room Temperature
HT	High Temperature
GITT	Galvanostatic Intermittent Titration Technique
FWHM	Full-Width Half-Max
HRTEM	High Resolution TEM
SAED	Selected Area Electron Diffraction
NT	Nanotube
EELS	Electron Energy Loss Spectroscopy
SRIM	Stopping Range of Ions in Matter (software)
CV	Cyclic Voltammetry
SEM	Scanning Electron Microscopy
I-V	Current – Voltage
UV	Ultraviolet

CAES	Center for Advanced Energy Studies
MaCS	Materials and Characterization Suite
STEM	Scanning Transmission Electron Microscopy
XRD	X-Ray Diffraction
CBED	Convergent Beam Electron Diffraction
BCA	Binary Collision Approximation
EIS	Electrochemical Impedance Spectroscopy
SEI	Solid Electrolyte Interphase

CHAPTER ONE: INTRODUCTION

This dissertation is composed of four papers that have been published, or are in preparation for publication. Chapter Two, which is currently under review, outlines work in which different point defects are generated in TiO_2 nanotube (TiO_2 NT) electrodes via a heat treatment method under various atmospheres. Annealing electrodes in controlled atmospheres provides evidence of electrochemical property enhancement due to generation of defects. The results provide a basis for comparison with the change in electrochemical response due to defect generation in TiO_2 NT by ion irradiation.

Chapter Three, published in the Journal of Materials Chemistry A, details the effect of low-energy proton irradiation on amorphous TiO_2 NT electrodes. Phase composition alteration due to irradiation and its resulting effect on electrochemical charge storage behavior is discussed. Similar to Chapter Three, Chapter Four presents the effects of low-energy proton irradiation on anatase TiO_2 NT electrodes. Unlike the amorphous TiO_2 NT, anatase TiO_2 NT is resistant to phase transformation during irradiation. Even so, there is an improvement to the electrochemical charge storage behavior due to the increase in charge storage sites, suggesting that defect generation induced by irradiation is beneficial for these electrodes.

Chapter Five, published in the Journal of the American Ceramic Society, focuses on the microstructural evolution in TiO_2 single crystal that occurs during irradiation. This chapter reports the formation of a complex, multi-layered microstructure of single crystal rutile TiO_2 upon 3 MeV Nb^+ ion irradiation. The results present evidence that multiple

defect mechanisms occur during irradiation as a function of ion implantation depth and disorder accumulation.

Each chapter of this dissertation was written to stand alone for the purpose of publication, rather than as one fluid document; however, the overarching theme among these chapters is to study the mechanisms of defect accumulation of TiO_2 electrodes for use as the anode material for lithium ion battery. Better understanding of irradiation effects on metal oxide electrodes may open pathways to designing advanced manufacturing of electrode materials for lithium ion batteries.

Detailed introductions including background and motivation for each chapter are given at the beginning of each chapter article, along with detailed descriptions of experimental procedures. A supplementary broad overview is given in the following sections of this chapter.

1.1 Motivation

Among current battery technologies, lithium ion batteries (LIBs) provide the highest energy density.[1] After their commercialization in the 1990's LIBs have not only dominated the portable electronics market, but also shown promise for large-scale electrochemical energy storage (EES) devices for renewable energy production.[1-4] In order to fulfill growing demands, next-generation LIBs are expected to show increased energy and power density, improved safety, and longer cycle life.[1, 5-8]

Currently, the most common commercial anode is graphite, which has a theoretical capacity of 372 mAh/g.[9, 10] However, the intercalation potential of graphite is 0.1 V *vs* Li/Li^+, increasing the likeliness of lithium plating and eventually dendrite formation. Once lithium dendrites have formed at the electrode surface, there is great risk

of short-circuiting and thermal run away, which has been known to cause several issues with past LIB technology.[11] To combat these problems, the battery community has focused on producing materials that circumvent the electrochemical safety concerns. Titanium dioxide is one promising alternative to graphite, because although it has a marginally lower theoretical capacity (335 mAh/g) it does not suffer lithium dendrite formation due to its higher intercalation potential of ~1.5-1.8 V vs Li/Li^+.

The eight known polymorphs of TiO_2 are rutile, anatase, brookite, TiO_2-B, TiO_2-R, TiO_2-H, TiO_2-II, and TiO_2-III. [12] The ability of a given polymorph to intercalate Li^+ strongly depends on the crystallinity, particle size, morphology, and surface area of the species involved.[13] Among those listed, rutile, anatase, and TiO_2-B are known as promising anodes for lithium ion batteries. While rutile is the most thermodynamically stable phase, lithium uptake at room temperature is limited for bulk materials.[13] Rutile has a tetragonal symmetry, with the space group $P4_2/mnm$, and edge sharing TiO_6 octahedra along the c-direction. During intercalation, lithium ions migrate into the tetrahedral sites. Over time their progress is limited by the repulsive forces between neighboring lithium ions.[12-13] Anatase has a tetragonal structure with the space group $I4_1/amd$ and the TiO_6 octahedra are stacked in one-dimensional zig-zag chains.[13-14] These pathways behave as diffusion channels for lithium ions to intercalate into the structure, allowing for greater lithium ion uptake.[12-13]

TiO_2 is a promising choice for lithium ion battery anodes, as it is relatively inexpensive, abundant, and environmentally benign.[14-16] Additionally, when used as an anode material, TiO_2 has good cycling stability due to the nominal <4% volume change during Li^+ insertion/extraction, compared to the 10% change that occurs in graphite.[17-19]

Despite its benefits, TiO_2 is not commercialized yet for LIBs due to its poor electrical conductivity and lithium ion diffusivity.[14, 20, 21] One way to mitigate these concerns is to nanostructure TiO_2, which results in improved electrochemical performance due to reduced ion diffusion distances, higher conductivity, and superior strain accommodation compared to their bulk counterparts.[20, 21]

A method to further enhance the electrochemical charge storage properties of TiO_2 is to introduce intentional structural defects (e.g. vacancies and interstitials).[22-24] Studies by Xiong et al. [23] along with works by others, [25-30] have suggested that nanoscale transition metal oxides, which have structural defects with local disorder, can offer enhanced capacity and structural stability under stress. Further, researchers have demonstrated that methods such as doping [22, 25] and ion irradiation [22, 25-34] can introduce defects that could enhance the charge storage of metal oxides. One approach to introduce defects in electrode materials is to utilize ion irradiation produce tunable defects in the target material[35].

1.2 Irradiation Effect in TiO_2

It is widely recognized that ion irradiation, i.e. the bombardment of a target with keV-MeV ions, introduces defects and regions of lattice disorder in crystalline solids.[36] This endeavor presents a unique method for introducing defects by ion irradiation, which has potential to transform battery applications, allowing for a new research pathway towards defect-driven electrode materials. EES technologies are being increasingly used under conditions that are, or could be, subject to radiation fields such as satellites and high altitude aircraft, sensor applications for nuclear power production, and nuclear

powered submarines or aircrafts. The ability to tailor conductivity – and hence, battery functionality – with in-service irradiation could be invaluable in these applications.

During ion bombardment, the irradiating particle slows down within the material and collides with lattice atoms. Some collisions transfer enough energy to displace atoms from their original position. This type of knock-on event can displace more and more atoms, resulting in a damage cascade. Eventually the volume immediately surrounding the ion track becomes populated with vacancies, interstitials, and other defects. As the fluence of the irradiating species increases, the damage cascades overlap resulting in the overall disordering of the material. Over time, this irradiation damage may be annealed out of the substrate, which is known as a self-healing, and significantly reduced the retention of defects formed during the damage cascade.[35]

The irradiation dose rate, ion penetration depth, and damage cascade morphologies vary depending on the type of particle used. When a charged particle is incident on the target, the charge of the ion will encounter Coulombic interactions with the positively charged nuclei and the negatively charged electron clouds of the target matrix. Coulombic effects reduce the momentum of the incident particle, and the resulting reduction in momentum limits the depth each particle is able to travel through the matrix.[35] Heavier ions, such as Nb^+, will lose momentum faster than light particles, such as protons. For example, a 200 keV acceleration voltage will allow protons to penetrate up to 1 μm in TiO_2, whereas Nb^+ must have a 3.5 MeV accelerating voltage to reach the same depth. It has also been suggested that different irradiating particles and their respective momentums allow for different morphologies of damage cascades to form.[35] The reduction in momentum and resulting damage profile of various irradiating

particles on a given target material can be calculated using the Stopping and Range of Ions in Matter (SRIM) software.[36]

In recent years, a body of work has been generated on the effects of irradiation on TiO_2. Two different studies conducted by Zheng et al. [23] and Qin et al.[27] examined the improvement of photovoltaic behavior of thin film anatase substrates irradiated with low energy metal ions. Zheng et al. later argued higher fluence irradiations (10^{17} ions cm^{-2}) caused recombination centers to form which actually reduces photocatalytic activity.[37] Additional studies have covered a range of topics from UV enhancement, optical absorption, and water splitting.[38, 39] Aside from experimental results, computational simulations have been conducted, which suggest that rutile has better resistance to amorphization than other TiO_2 polymorphs due to atomic packing densities.[38, 40, 41] Further studies by Uberuagua, Qin, and Lumpkin are in agreement with these studies and have further elucidated on the mechanisms of defect accumulation and amorphization resistance.[40, 42, 43] Aside from polymorph dependence, Li et al. [22] showed that irradiating at higher temperatures allow for point defect mobility, increasing instances of damage recovery. Conversely, room temperature irradiation results in more stable point defect generation which was later supported by Zhang et al.[44] Finally, Hartmann et al.[45] suggests that using lighter irradiation species, such as He^+, is more likely to amorphize target substrates than heavy noble gases such as Xe^{2+} and Ne^+.

1.3 Research Methods

The foundation of this research is the hypothesis that irradiation can improve the electrochemical properties of TiO_2. To test this hypothesis our research goals are to tailor the presence and distribution of defects in metal oxides using irradiation, and to gain a

fundamental understanding of how irradiation alters the ion transport mechanism and intercalation kinetics of TiO_2. We approached these tasks by following the materials science tetrahedron:

i. Processing – Synthesis of TiO_2 nanotubes; controlled irradiated parameters to tailor defect population

ii. Performance – Subjecting the pre- and post- irradiated TiO_2 to electrochemical testing;

iii. Structure – Obtaining fundamental understanding of the irradiation effects on microstructure and ion transport;

iv. Properties – Determining if irradiation can improve the charge capacity of TiO_2 electrodes

1.4 References

[1] J.M. Tarascon, M. Armand, Nature, 414 (2001) 359-367.

[2] B. Dunn, H. Kamath, J.M. Tarascon, Science, 334 (2011) 928-935.

[3] J.M. Tarascon, *Chem. Sus. Chem.*, 1 (2008) 777-779.

[4] M.M. Thackeray, C. Wolverton, E.D. Isaacs, *Eng. Environ. Sci.*, 5 (2012) 7854-7863.

[5] M. Armand, J.M. Tarascon, Nature, 451 (2008) 652-657.

[6] N.S. Choi, Z.H. Chen, S.A. Freunberger, X.L. Ji, Y.K. Sun, K. Amine, G. Yushin, L.F. Nazar, J. Cho, P.G. Bruce, *Ang. Chem. Int.*, 51 (2012) 9994-10024.

[7] J.B. Goodenough, Y. Kim, *Chem. Mater.*, 22 (2010) 587-603.

[8] J.M. Tarascon, *Philos. Trans. R. Soc., A*, 368 (2010) 3227-3241.

[9] V. Etacheri, R. Marom, R. Elazari, G. Salitra, D. Aurbach, *Energy Environ. Sci.*, 4 (2011) 3243-3262.

[10] Z.G. Yang, J.L. Zhang, M.C.W. Kintner-Meyer, X.C. Lu, D.W. Choi, J.P. Lemmon, J. Liu, *Chem. Rev.,* 111 (2011) 3577-3613.

[11] Q.S. Wang, P. Ping, X.J. Zhao, G.Q. Chu, J.H. Sun, C.H. Chen, *J. Power Sources,* 208 (2012) 210-224.

[12] L. Kavan, M. Gratzel, S. E. Gilbert, C. Klemenz, H. J. Scheel, *J. Amer. Chem. Soc.,* 118 (1996) 6716-6723.

[13] Z. Wang, D. Choi, S. Kerisit, K. Rosso, D. Wang, J. Zhang, G. Graff, J. Liu, *J. Power Sources,* 192 (2009) 588-598.

[14] K. Lee, A. Mazare, P. Schmuki, *Chem. Rev.,* 114 (2014) 9385-9454.

[15] W.H. Ryu, D.H. Nam, Y.S. Ko, R.H. Kim, H.S. Kwon, *Electrochim Acta*, 61 (2012) 19-24.

[16] D. Bresser, B. Oschmann, M.N. Tahir, F. Mueller, I. Lieberwirth, W. Tremel, R. Zentel, S. Passerini, *J Electrochem Soc,* 162 (2015) A3013-A3020.

[17] M. Fehse, E. Ventosa, *Chem. Plus. Chem.,* 80 (2015) 785-795.

[18] J. Kim, J. Cho, *J Electrochem Soc*, 154 (2007) A542-A546.

[19] Y. Qi, S.J. Harris, *J Electrochem Soc*, 157 (2010) A741-A747.

[20] D. Deng, M.G. Kim, J.Y. Lee, J. Cho, *Energy Environ. Sci*., 2 (2009) 818-837.

[21] Y. Li, J.D. Luo, X.Y. Hu, X.F. Wang, J.C. Liang, K.F. Yu, J *Alloy Compd*, 651 (2015) 685-689.

[22] B.P. Hahn, J.W. Long, D.R. Rolison, *Acc. Chem. Res.,* 46 (2013) 1181-1191.

[23] B. Koo, H. Xiong, M.D. Slater, V.B. Prakapenka, M. Baasubramanian, P. Podsiadlo, C.S. Johnson, T. Rajh, E.V. Shevchenko, *Nano Lett.,* 12 (2012) 2429-2435.

[24] B. Koo, S. Chattopadhyay, T. Shibata, V.B. Prakapenka, C.S. Johnson, T. Rajh, E.V. Shevchenko, *Chem. Mater.*, 25 (2013) 245-252.

[25] D.R. Rolison, L.F. Nazar, *MRS Bull*, 36 (2011) 486-493.

[26] H.A. Shukur, M. Sato, I. Nakamura, I. Takano, *Adv Mater Sci Eng*, (2012) 1-7.

[27] L.Z. Qin, B. Liao, X.L. Dong, X.Y. Wu, X.G. Hou, A.D. Liu, *Nucl. Instrum. Methods Phys. Res., Sect. B*, 267 (2009) 1077-1080.

[28] N. Matsunami, M. Uebayashi, K. Hirooka, T. Shimura, M. Tazawa, *Nucl. Instrum. Methods Phys. Res., Sect. B*, 267 (2009) 1654-1657.

[29] R. Fromknecht, I. Khubeis, S. Massing, O. Meyer, *Nucl. Instrum. Methods Phys. Res., Sect. B*, 147 (1999) 191-201.

[30] O. Meyer, I. Khubeis, R. Fromknecht, S. Massing, *Nucl. Instrum. Methods Phys. Res., Sect. B*, 136 (1998) 436-441.

[31] O. Meyer, I. Khubeis, R. Fromknecht, S. Massing, *Nucl. Instrum. Methods Phys. Res., Sect. B*, 127 (1997) 624-628.

[32] S.K. Zheng, T.M. Wang, C. Wang, G. Xiang, *Nucl. Instrum. Methods Phys. Res., Sect. B*, 187 (2002) 479-484.

[33] S.K. Zheng, T.M. Wang, W.C. Hao, R. Shen, *Vacuum*, 65 (2002) 155-159.

[34] D. Su, F. Wang, C. Ma, N. Jiang, *Nano Energy*, 2 (2013) 343-350.

[35] G.s. Was, Fundamentals of Radiation Materials Science: Metals and Alloys, Springer, 2007.

[36] J. F. Ziegler, 2013.

[37] S.K. Zheng, Wang, T. M., Wang, C., Xiang, G. , *Nucl. Instrum. Methods Phys. Res., Sect. B*, 187 (2002) 479-484.

[38] H.A. Shukur, M. Sato, I. Nakamura, I. Takano, *Adv Mater Sci Eng*, 2012 (2012) 1-7.

[39] R. Fernandes, N. Patel, R. Dholam, M. Adami, A. Miotello, *Surf. Coat. Technol.*, 203 (2009) 2579-2583.

[40] G.R. Lumpkin, K.L. Smith, M.G. Blackford, B.S. Thomas, K.R. Whittle, N.A. Marks, N.J. Zaluzec, *Phys. Rev. B: Condens. Matter*, 77 (2008).

[41] H. Rath, P. Dash, T. Som, P.V. Satyam, U.P. Singh, P.K. Kulriya, D. Kanjilal, D.K. Avasthi, N.C. Mishra, *J. Appl. Phys.*, 105 (2009) 074311.

[42] B.P. Uberuaga, X.M. Bai, *J. Phys.: Condens. Matter*, 23 (2011).

[43] M.J. Qin, E.Y. Kuo, K.R. Whittle, S.C. Middleburgh, M. Robinson, N.A. Marks, G.R. Lumpkin, *J. Phys.: Condens. Matter*, 25 (2013) 355402.

[44] J. Zhang, J. Lian, F. Namavar, J. Wang, H. Haider, K. Garvin, R.C. Ewing, *J. Phys. Chem. C*, 115 (2011) 22755-22760.

[45] T. Hartmann, L. M. Wang, W. J. Weber, N. Yu, K. E. Sickafus, J. N. Mitchell, C. J. Wetteland, M. A. Nastasi, M. G. Hollander, N. P. Baker, C. R. Evans, J. R. Tesmer and C. J. Maggiore, *Nucl. Instrum. Methods Phys. Res., Sect. B*, 1998, **141**, 398-403.

CHAPTER TWO: DEFECT GENERATION IN TIO_2 NANOTUBE ANODES VIA HEAT TREATMENT IN VARIOUS ATMOSPHERES FOR LITHIUM-ION BATTERIES

This chapter has been submitted for publication.

Reference:

A. Savva, K. Smith, M. Lawson, S. Croft, A. Weltner, C. Jones, H. Bull, P. Simmonds, L. Li and H. Xiong, “Defect Generation in TiO_2 Nanotube Anodes via Heat Treatment in Various Atmospheres for Lithium-Ion Batteries” *Submitted to Phys. Chem. Chem. Phys.,* (2018)

Defect Generation in TiO_2 Nanotube Anodes via Heat Treatment in Various Atmospheres for Lithium-Ion Batteries

Andreas I. Savva[a]

Kassiopeia A. Smith[a]

Matthew Lawson[a]

Sterling R. Croft[a]

Ariel E. Weltner[a]

Chris D. Jones[a]

Hailey Bull[a]

Paul J. Simmonds[a]

Lan Li[a]

Hui Xiong[a]

Submitted for publication in:

Physical Chemistry Chemical Physics

June, 2018

[a] *Micron School of Materials Science and Engineering, Boise State University, 1910 University DR., Boise, ID 83725, USA*

2.1 Abstract

The generation of point defects in metal oxides such as TiO_2 has been shown in previous studies to improve its electrochemical charge storage capacity. In this paper, ordered TiO_2 nanotubes were grown on a Ti substrate via electrochemical anodization and subsequently annealed at 450°C for 4 h under various atmospheres to create different point defects. Oxygen-deficient environments such as Ar and N_2 were used to develop oxygen vacancies, while a water vapor atmosphere was used to generate titanium vacancies. Computational models by density functional theory predicted that the presence of oxygen vacancies would cause electronic conductivity to increase, while the presence of Ti vacancies could lead to decreased conductivity. The predictions were confirmed by two-point electrical conductivity measurements and Mott-Schottky analysis. Raman spectroscopy was also conducted to confirm the presence of defects. The annealed samples were then evaluated as anodes in lithium-ion batteries. The oxygen-deficient samples had an improvement in capacity by 10% and 25% for Ar- and N_2-treated samples, respectively, while the water vapor -treated sample displayed a capacity increase of 24% compared to the stoichiometric control sample. Electrochemical impedance spectroscopy studies revealed that the water vapor -treated sample's increased capacity was a consequence of its higher Li diffusivity. The results suggest that balanced electrical and ionic conductivity in nanostructured metal oxide anodes can be tuned through defect generation using heat treatments in various atmospheres for improved electrochemical properties.

2.2 Introduction

There has been growing demand for improved performance in electrode materials for lithium-ion batteries as electric vehicles and electric grid storage become more prevalent. Graphite is commonly used as the anode in lithium-ion batteries and has a theoretical capacity of 372 mAh/g.[1-3] Despite its widespread use, there are concerns about its safety and long-term stability as its lithiation potential (~0.1 V vs. Li/Li^+) is close to that of lithium plating, which could lead to dendrite formation and short-circuiting.[2, 4] Titanium dioxide (TiO_2) is a promising alternative as it is cheap, environmentally friendly, abundant, and has comparable theoretical capacity with graphite (335 mAh/g), along with a higher lithiation potential (~1.5-1.8 V vs. Li/Li^+).[2, 5-8] TiO_2 has multiple polymorphs (anatase, TiO_2-B, rutile, brookite, etc.), and anatase TiO_2 is most commonly used in lithium-ion batteries, as its tetragonal structure has a high degree of octahedral sites for Li intercalation, [4, 7, 9-10] Yet in practice only 0.5 Li per Ti can intercalate in bulk anatase, resulting in a much lower capacity compared to its theoretical value. This is primarily due to its poor electrical conductivity and lithium diffusivity.[1-2, 6] Nanostructured TiO_2 can alleviate these issues, as it can shorten the distance that Li ions and electrons need to travel.[1-2, 5-6, 8]

The generation of point defects in TiO_2 and other metal oxides has been shown to improve their functionalities in a few applications. Through the introduction of defects, metal oxides have demonstrated superior properties for applications in photocatalysts, solar cells, and batteries.[11-18] These defects can be induced through methods such as substitutional doping or ion irradiation.[19-22] Another approach to create point defects is through annealing under different atmospheres.[11, 17, 23-26] If TiO_2 is annealed under

oxygen-deficient environments (e.g., under pure Ar or N_2), oxygen vacancies can form and generate free electrons, as well as reduce Ti (**Eq. 1, Eq. 2**) [12, 14, 26-28] and can be expressed in the classical Kröger-Vink notation as follows:

$$TiO_2 \rightarrow 2V_O^{\cdot\cdot} + O_{2(g)} + Ti_{Ti}^{x} + 4e^- \quad (1)$$

$$TiO_2 \rightarrow 2V_O^{\cdot\cdot} + O_{2(g)} + Ti_{Ti}^{\prime} + 3e^- \quad (2)$$

Oxygen vacancy formation may result in higher electronic conductivity, improved rate capability, and higher capacity.[12, 14, 16, 23, 26-27] Under heat treatments where oxygen is present, any oxygen vacancies already present in the sample will be eliminated, making TiO_2 more stoichiometric (**Eq. 3**).

$$O_{2(g)} + V_O^{\cdot\cdot} \rightarrow O_O^{x} \quad (3)$$

Cation vacancies may be stabilized if water vapor is added to an oxygen-rich annealing environment.[28] The water vapor may protonate existing oxygen sites and cause a positive charge, which would subsequently stabilize cation vacancies present in the sample (**Eq. 4**). It has been shown in TiO_2 and other metal oxides that cation vacancies may provide more sites for lithium intercalation and therefore increase capacity.[13, 21, 28-30] Furthermore, during Li intercalation, the Li ions can exchange with protons without affecting the charge balance, which would provide additional sites to store Li, and thus also increase capacity (**Eq. 5**).[28]

$$V_{Ti}^{\prime\prime\prime\prime} + 2V_{\ddot{O}} + O_2 + 2H_2O \rightarrow V_{Ti}^{\prime\prime\prime\prime} + 4OH_O^{\cdot} \quad (4)$$

$$(OH)_O^{\cdot} + Li^+ \rightarrow (OLi)_O^{\cdot} + H^+ \quad (5)$$

Herein, we report a systematic investigation of anatase TiO_2 nanotubes as an anode in lithium-ion batteries after they are subjected to different atmospheric heat treatments to generate point defects. Density functional theory (DFT) calculations were

conducted to predict the effects that oxygen and cation vacancies would have on the electrical properties of TiO_2 by creating theoretical band structures and partial charge models. TiO_2 nanotube electrodes were prepared via electrochemical anodization and subsequently annealed under various atmospheres (O_2, Ar, N_2, and water vapor). The nanotube thin film samples were subjected to two-point conductivity measurements and Mott-Schottky analysis to determine how each annealing condition affected the electrical conductivity of the nanotubes. Raman spectroscopy was used to confirm the presence of the various point defects, while x-ray diffraction (XRD) and scanning electron microscopy (SEM) were used to observe any crystallographic or morphological changes in the nanotubes as a consequence of the heat treatments. Electrochemical testing was also conducted to elucidate how the resulting point defects improved battery performance. The characterizations and testing revealed that the Ar and N_2 treatments increased the electrical conductivity of the samples due to oxygen vacancy formation, while the water vapor treatment created Ti vacancies, which lowered the electrical conductivity. Nevertheless, both the N_2- and water vapor -treated samples exhibited the largest specific capacity increase among tested samples. In addition, the N_2-treated samples had the best rate capability, while the water vapor -treated samples had the largest Li diffusivity. Our results suggested that both electronic conductivity and ionic conductivity in intercalation electrode materials need to be considered for understanding their charge storage and transport properties, and the type of defects has a critical influence on the charge storage and transport mechanism in metal oxide electrodes.

2.3 Methods

2.3.1 Anodization of Ti Foil

Ti foil (Alfa Aesar, 0.032 mm thick) was cut into 4 x 4.5 cm pieces and sonicated in acetone, isopropanol, and DI water for 5 minutes each. The foil was then air-dried and the back was protected with acrylic sheeting and packing tape for uniform current distribution during anodization. The prepared foil was anodized in a solution of 0.27 M NH_4F in formamide, with Pt mesh as the counter electrode, for 30 minutes at 15 V and 0.2 A. After anodization was complete, the foil was dipped in DI water to remove excess solution and then sonicated in isopropanol and DI water for three 1-second bursts each. The foil then had its backing carefully peeled off and was dried for several hours in a vacuum oven at approximately 70°C to remove any residual moisture.

2.3.2 Annealing of TiO_2 Nanotubes

Four 15 mm discs were punched out of each sample using a Precision Disk Cutter (MTI). One disc from each sample was sacrificed for active weight measurements by using scotch tape to strip the nanotubes from the Ti substrate. The other three discs were annealed in an OTF-200X tube furnace (MTI) at 450°C for 4 h under O_2 (80% Ar, 20% O_2), Ar (99.9%), N_2 (99.9%), and water vapor (80% Ar, 20% O_2). The water vapor atmosphere was generated by bubbling O_2 gas (80% Ar, 20% O_2) through a water bath heated to 80°C. The gas flow rate was held constant (one bubble per second) with minimal variation between atmospheric treatments.

2.3.3 Electrochemical Measurements

Coin cells (Hohsen 2032) were assembled in an Ar-filled glovebox (Mbraun) with an O_2 concentration less than 0.5 ppm. The annealed TiO_2 discs were the working

electrodes and Li metal (FMC Lithium) was used as the counter electrode with microporous polyolefin separators (Celgard 2325). The electrolyte was 1.2 M $LiPF_6$ (Tomiyama) in ethylene carbonate/ethyl methyl carbonate (3:7 weight ratio). The cells were then cycled from 0.9 to 2.5 V vs. Li/Li^+ at a theoretical C rate of C/20 (16.75 mA/g) using an automated battery tester (Arbin). For the rate study, the cells were cycled in the same voltage window at theoretical C rates of C/20, C/10, C/5, C/2, 1C, and 5C. The cells were placed in a ThermoFisher Heratherm incubator during cycling at a constant temperature of 25°C.

Mott-Schottky analysis was performed using the SPEIS program on a Bio-Logic VMP-300 in a three-electrode cell. Samples were masked with Kapton tape with a 15 mm diameter area left exposed. A Pt mesh was used as the counter electrode in an aqueous 1 M KOH solution. An Ag/AgCl reference electrode was used. Samples were subsequently analyzed in a frequency range from 100 kHz to 100 mHz with an excitation voltage of 10 mV from 0.1 to -1 V vs. Ag/AgCl in 0.05 V increments. Electrochemical impedance spectroscopy (EIS) was done on a Bio-Logic VMP-300 using a three-electrode cell (EL-CELL). Samples were analyzed in a frequency range from 100 kHz to 5 mHz at open circuit voltages by applying a sinusoidal voltage with an amplitude of 5 mV.

2.3.4 Characterizations

XRD was done using a Rigaku MiniFlex 600 with a 600 W generator and Cu target; 2θ was scanned from 20-85°. The instrumental broadening was accounted for by scanning a LaB_6 standard and subtracting the peak width from the resulting experimental data. The nanotube morphology was observed via SEM using a FEI Teneo field emission microscope operating at 5 kV. Raman spectroscopy was completed with a Horiba

Scientific LabRam HR Evolution spectrometer using a 442 nm He:Cd laser with signal accumulation of 30 s scans. After instrument calibration, the samples were scanned at room temperature with an incident laser power of 100 mW from 100-1000 cm^{-1}. Samples were viewed at a magnification of 100x and scattered light was collected with a thermoelectrically cooled Si CCD detector.

Two-point electrical conductivity measurements were used to determine the out-of-plane conductivity of the nanotubes. A silver paint contact was placed on the nanotube surface with another on the back of the Ti foil; copper wire was attached to the bottom to serve as a contact point for the instrument. The contacts were about 2 mm in diameter and a current of 10 μA was applied to each sample. A porosity of 0.46 was used to calculate the electrical conductivity (**Supporting Information**). A Keithley 237 High Voltage Source Measure Kit was used to apply the current to each sample and a Keithley 2000 Multimeter was used to record the resulting resistance.

2.3.5 Computational Modeling

To predict the electronic structure and properties of the anatase TiO_2, density functional theory (DFT) was performed using VASP.[31] The exchange-correlation energies were described using the PBE (Perdew-Burke-Ernzerhof) pseudopotentials and GGA (Generalized Gradient Approximation).[32] A cut-off energy of 380 eV was chosen to account for the plane-wave basis set. To incorporate a rich electronic structure, the unit cell of the anatase phase was expanded into a 3 x 3 x 1 supercell with a Γ-centered 5 x 5 x 7 k-point mesh sampling in the Brillouin zone. The electronic structures and properties of pristine, oxygen-deficient, and Ti-deficient anatase TiO_2 were calculated from their respective ground state structures with residual forces of 0.1 eV/Å and an electronic

convergence of $1x10^{-6}$ eV. The band structures of these systems were also determined. To account for the strongly correlated *d* orbital effect on titanium, the DFT + U scheme was applied with an on-site Coulomb potential of 8.0 eV, and the partial charge densities were also generated 2 eV above and below the Fermi energy to further study how the electron density distribution was affected by various defects.[33]

2.4 Results and Discussion

Computational modeling was conducted to predict the electronic properties of anatase TiO_2 and the effects of oxygen and titanium vacancies. For the pristine anatase structure, the bandgap was found to be approximately 3.2 eV, agreeing well with literature reported values via experiments and theoretical calculations (Figure 2.1a).[34-38] There were significant changes to the band structure after an oxygen atom was removed from the anatase supercell, which resulted in an oxygen vacancy concentration of 1.39%. The Fermi energy shifted into the conduction band (viz., the conduction band shifted below the Fermi energy), and a mid-gap state appeared about 0.8 eV below the conduction band (Figure 2.1b). The Fermi energy shift and the development of a mid-gap state were expected, as previous experimental studies had shown similar results.[36, 39-40] The new mid-gap state is indicative of Ti^{3+} defect states, which have developed due to the introduction of oxygen vacancies, and subsequently act as electron donors for n-type semiconducting characteristics.[35, 40] These changes could potentially cause an increase in the electrical conductivity for the oxygen-deficient case due to n-type semiconductor behavior.

Since our computational model was in agreement with literature for the oxygen-deficient structure, the same approach was used for the Ti vacancy scenario. 4 H^+ ions

were inserted into the O sites around the vacancy to stabilize it and more accurately represent the defects introduced during water vapor treatment. A defect concentration of 2.77% was achieved upon the removal of a Ti atom from the supercell. The resulting band structure changes for Ti-deficient anatase were not as drastic compared to the introduction of an oxygen vacancy, but they were still significant. The Fermi energy shifted down into the valence band (viz., the valence band shifted above the Fermi energy) and a new band appeared less than 0.2 eV above the valence band Fig 2.1c). These changes imply that a large concentration of Ti vacancies in TiO_2 may result in p-type semiconductor behavior. However, it was unclear from this result whether the oxygen or Ti vacancies would have a larger impact on the electrical conductivity.

In order to further investigate the defect influence on the electronic properties, partial charge density (i.e., band decomposed) calculations were conducted for the valence band maximum (VBM) and conduction band minimum (CBM) states, as shown in Figure 2.2. The figure depicts available charge states for a given energy range. The energy range from -2.0 eV to 0 eV was used for the VBM, while 0 eV to 2.0 eV was used for the CBM. In comparison to pristine anatase TiO_2 (Figure 2.2a), the partial charge density with the O vacancy at the VBM is highly localized around the vacancy site (Figure 2.2b). Figure 2.2c shows that the partial charge density with the Ti vacancy at the VBM decreases at the O sites but they remain at the Ti sites. In addition, the CBM analysis indicates that the partial charge density with the O vacancy is more localized both at the Ti and O sites in Figure 2.2e than that for pristine anatase TiO_2 (Figure 2.2d) and the Ti vacancy case (Figure 2.2f). The computational results suggest that the oxygen

vacancy could potentially cause an increase in electrical conductivity while the Ti vacancy would decrease it.

To validate these predictions, TiO_2 nanotubes were annealed under O_2, Ar, N_2, and water vapor at 450°C for 4 h to generate the appropriate defects. The samples were then characterized to determine whether the electrical properties had been altered as a result of the various atmospheric heat treatments. Mott-Schottky characterizations enabled the quantitative measurement of the samples' charge carrier densities. It is important that the appropriate frequency be selected for analysis of Mott-Schottky tests. The charge carrier density of the sample was determined from space charge capacitance (C_{sc}), which was obtained from *Z''*, the imaginary contribution to impedance and the frequency *f* (**Eq. 7)**.[41-42].

$$C_{sc} = -\frac{1}{2\pi f Z''} \quad (7)$$

If the frequency was too low, surface state capacitance (C_{ss}) would contribute to the total capacitance, incorrectly shifting results towards higher carrier density values.[41] In addition, the real contribution to impedance, *Z'*, would also vary with frequency.[41] As a consequence, Bode plots in the frequency range of 100 kHz-100 mHz were used to determine the frequency at which *Z'* becomes constant (**Supporting Information**). The plot for each atmosphere indicated that *Z'* plateaus at a frequency of about 500 Hz; the curves at 1.3 kHz were therefore used to calculate the charge carrier density for each sample. The following equation (**Eq. 8**) relates the charge carrier density to the capacitance of the Mott-Schottky plot, where q is the charge of an electron, ε is the dielectric constant (31 for anatase),[24, 43] ε_0 is the vacuum permittivity constant, N_D is the

charge carrier density, A is the geometric surface area, V_{fb} is the flat-band potential, V is the applied potential, k is Boltzmann's constant, and T is the temperature.[42, 44]

$$C_{sc}^{-2} = \left(\frac{2}{q\epsilon\epsilon_0 N_D A^2}\right)\left(V - V_{fb} - \frac{kT}{q}\right) \quad (8)$$

Eq. 8 is then differentiated with respect to the voltage and manipulated to the below form (**Eq. 9**) where the slope of the plot's linear region $\frac{dC^{-2}}{dV}$ is used to obtain the charge carrier density.

$$N_D = \frac{2}{q\epsilon\epsilon_0 A^2}\left(\frac{dC^{-2}}{dV}\right)^{-1} \quad (9)$$

Each Mott-Schottky curve (Figure 2.3) had a positively sloped linear region, confirming the n-type semiconductor behavior expected for TiO_2.[42, 44-47] According to **Eq. 9**, as the slopes become less steep, the charge carrier densities will increase. From the Mott-Schottky plot, the O_2 and water vapor samples have the lowest carrier densities, followed by Ar and N_2 (Table 2.1). These results corroborate well with the computational models. Annealing under oxygen-deficient conditions should result in the generation of oxygen vacancies, which would result in the presence of more free electrons in the TiO_2 nanotube structure. Since TiO_2 is a n-type semiconductor, its charge carriers are electrons, which means an increase in electrons would lead to a shallower slope in the Mott-Schottky plots. The slight positive shift of the flat-band potential for the oxygen-deficient treatments also suggests that oxygen vacancies may have formed.[11, 47] The water vapor sample has a small decrease in charge carrier density compared to the O_2 control at 1.3 kHz, which is also consistent with results from the simulations.

Electrical conductivity measurements were subsequently done to compare with the conclusions drawn from the Mott-Schottky analysis. Using a two-point

measurement,[48] the out-of-plane conductivities of the annealed nanotubes were found (Table 2.2). The oxygen-deficient atmospheres increased electrical conductivity, with the N_2 treatment changing by two orders of magnitude. In contrast, the water vapor treatment caused the electrical conductivity to decrease. These results were consistent with the Mott-Schottky data, as changes in charge carrier density should correlate with the electrical conductivity. Our conductivities were also comparable with previously reported two-point measurements on anatase TiO_2 nanotubes.[23, 48] The conductivity measurements and Mott-Schottky analysis corroborate well with the theoretical models. The Ar and N_2 treatments increase the electrical conductivity and charge carrier density of the anatase TiO_2 nanotubes, suggesting that the oxygen-deficient atmospheric annealing treatments have indeed created oxygen vacancies. On the other hand, the water vapor treatment displays a slight decrease in its electrical conductivity, which implies that Ti vacancies may have formed.

It is interesting to note that the Ar-treated samples have lower conductivities and carrier densities compared to the N_2-treated samples. Although it is beyond the scope of this paper, the variation in conductivity as a result of the two different oxygen-deficient treatments may be due to their reactivity. Since Ar is a noble gas, it will not interact with any oxygen atoms that have been released from TiO_2. Any oxygen atoms that do not combine to form O_2 will likely reenter the TiO_2 structure. However, N_2 could form a variety of nitrogen oxides with the outgassed oxygen atoms, especially given the high annealing temperature. The consumption of additional oxygen atoms as a consequence of nitrogen oxide formation could explain the increase in oxygen vacancies and

conductivity. Further research would have to be conducted to verify this proposed mechanism.

Additional characterizations were used to determine the morphological and crystallographic effects of the atmospheric heat treatments, as well as to further confirm the presence of the generated point defects. SEM images of the TiO_2 nanotubes after treatment show that the nanotubes maintain their structural integrity regardless of annealing conditions, with an average outer tube diameter of approximately 60 -65 nm and tube wall thickness of about 10 nm (Figure 2.4). Each of the annealed samples was subsequently characterized using XRD. As expected, the resulting XRD spectra for each sample matched well with anatase TiO_2 (Supporting Information). Strong Ti peaks were also present due to the Ti substrate.

In addition, there was a slight presence of rutile (110) peak in the XRD of the O_2 and water vapor samples, but not so much in the N_2 or Ar samples, which is consistent with previous reports on the inhibition of anatase-rutile transformation in oxygen-deficient environments.[15, 18, 22, 47] The weight percentage of the rutile phase was found using the equation developed by Spurr et al.[49] to be 16%, 9%, and 6% for the O_2-, water vapor -, and N_2-treated samples, respectively, while there was no rutile phase present in the Ar-treated sample. The presence of rutile is likely concentrated primarily in the barrier layer between the nanotubes and the Ti substrate as reported previously.[50] However, it is unlikely that the rutile phase has a significant effect on the electrical conductivity of the samples treated by different atmospheres during annealing. While rutile has a higher electrical conductivity[51] compared to anatase due to a smaller band gap (3.0 eV in rutile *vs.* 3.2 eV in anatase), the percentage of rutile does not match the

conductivity trend obtained from the two-point measurements. Furthermore, the charge carrier densities, which were obtained via Mott-Schottky analysis, only match the electrical conductivity trend and not the trend of rutile composition of the samples. This is significant as Mott-Schottky analysis is a surface technique, which indicates that the electrical conductivity trends are more reflective of the composition of the tubes at the surface (viz. anatase TiO_2) than the composition at the nanotube-substrate interface. Thus, the presence of rutile in the barrier layer has a negligible effect on the electrical properties of the anatase TiO_2 nanotubes.

Upon refining the XRD spectra, there were no significant changes in the unit cell parameters for samples annealed in different atmospheres compared to the O_2 control sample. This indicates that the changes in unit cell for the TiO_2 nanotubes as a consequence of the various heat treatments were negligible.

The annealed samples were also characterized using Raman spectroscopy (Figure 2.5). Each sample clearly had the associated spectrum for anatase TiO_2, with peaks present at approximately 144 cm^{-1}, 395 cm^{-1}, 517 cm^{-1}, and 636 cm^{-1}. These peaks correspond to the $E_g(1)$, $B_{1g}(1)$, $B_{1g}(2)+A_{1g}$, and $E_g(3)$ vibrational modes, respectively. [23, 52-54] A small peak at 196 cm^{-1} associated with the $E_g(2)$ vibrational mode was also present in all four samples.[52, 54] As seen in Figure 2.5, there are some differences in the annealed samples compared to the O_2 control sample. The N_2 sample has a slight blueshift of the $E_g(1)$ peak of about 1.77 cm^{-1}, in addition to some peak broadening of about 1.32 cm^{-1}. Strain, phonon confinement, and nonstoichiometry could all contribute to the development of the observed blueshift and broadening.[53-58] Williamson-Hall plots were used to determine whether strain was present in the samples; it was found that the

strain was insignificant and thus did not contribute to the Raman peak shift (**Supporting Information**).

Dispersion caused by phonons will occur if the crystallite size is small enough (viz., less than 10-20 nm).[23, 27, 53] Using the Scherrer equation,[59] the crystallite size for the N_2 sample was found to be 48 nm. Since this value is larger than the critical limit of 20 nm, the broadening and shift of the $E_g(1)$ mode is not a consequence of phonon confinement. Thus, it is most probable that the observed changes in the $E_g(1)$ mode are due to the formation and proliferation of oxygen vacancies. Similar results have been reported in a number of studies on non-stoichiometric TiO_2 nanostructures.[23, 27, 58, 60] Furthermore, the observed Raman shift for the N_2 sample is also in agreement with the computational models and enhanced electrical conductivity.

The other peaks of the N_2 sample are not shifted or broadened to any significant extent. The samples annealed under Ar and water vapor have negligible peak shift and broadening for all vibrational modes. This is expected for the water vapor sample, as no oxygen vacancies are expected to form. It also suggests that the Ti vacancy concentration is not large enough to have an effect on the Raman spectrum of anatase TiO_2. The lack of peak shift is slightly surprising in the case of Ar, as it is also an oxygen-deficient atmosphere. However, the lower concentration of O vacancies for the Ar-treated sample may be responsible for the lack of $E_g(1)$ blueshift; this result is also consistent with the conductivity and Mott-Schottky measurements. It should be noted that the N_2 and Ar samples have lower peak intensities compared to the O_2 and water vapor samples, as this decrease in intensity could indicate some disorder due to defect generation.

The annealed samples were subsequently used as anodes in lithium-ion batteries to determine their electrochemical performance. The O_2-treated control sample displayed an initial charge of 197.6 mAh/g, which stabilized to 186.9 mAh/g at C/20 after 30 cycles (Figure 2.6). The capacity of the control sample was consistent with previously reported values for anatase TiO_2 nanotubes in Li-ion systems.[9, 61-62] There was a marked increase in specific capacity when the electrode was annealed in oxygen-deficient environments. The initial charge capacity for the Ar-treated sample was 218.0 mAh/g which decreased to 206.4 mAh/g after 30 cycles, while the N_2-treated sample had initial charge capacity of 246.6 mAh/g and dropped to 232.7 mAh/g after 30 cycles. The water vapor -treated sample exhibited a similar increase in capacity to the N_2 sample. The initial charge capacity was 246.5 mAh/g and maintained 231.3 mAh/g after 30 cycles. The Coulombic efficiency after 30 cycles for all atmospheric treatments was fairly consistent, as the values for O_2 control, Ar, N_2, and water vapor were 98.8, 97.7, 98.1, and 97.1%, respectively.

The changes in specific capacity as a consequence of atmospheric heat treatment were consistent with the aforementioned characterizations. The improved electrical conductivity displayed by the nanotubes due to the generation of oxygen vacancies in the Ar- and N_2-treated samples facilitated an increase in specific capacity. The disparity between the Ar- and N_2-treated samples is still present, as the N_2 treatment has a significantly higher capacity compared to the Ar-treated sample. This difference is consistent with the electrical conductivity measurements and gives additional support to the claim that annealing under Ar generates fewer oxygen vacancies compared to N_2. It is important to note that the water vapor treatment resulted in capacity comparable to the N_2

treatment, which suggests that the slight decrease in electrical conductivity has a negligible effect on the anode's charge storage properties and the effect of the Ti vacancies on increased charge storage sites is more significant.

The voltage profiles of each sample were studied to determine whether there were any fundamental differences in electrochemical behavior (Figure 2.7). The shape of the voltage profiles and dQ/dV plots (Supporting Information) were quite similar for each of the annealed samples. For all samples, a wide discharge two-phase plateau begins at about 1.78 V, which is followed by a much smaller plateau at approximately 1.5 V. The charge profile displays a change of slope near 1.6 V and its wide two-phase plateau region begins at approximately 1.87 V. The plateau regions for the charge and discharge profiles are consistent with the Li deintercalation and intercalation potentials for anatase TiO_2. [8-9, 61, 63-64] The presence of these plateaus indicates the addition and removal of Li ions to and from the octahedral interstitial sites.[8, 61, 64] The onset of the wide discharge plateau at 1.78 V corresponds to the transition of Li-poor anatase TiO_2 to $Li_{0.5}TiO_2$ (*Imma*) and the following plateau at 1.5 V then describes the transition of $Li_{0.5}TiO_2$ to $LiTiO_2$ ($I4_1/amd$) with further lithium intercalation.[65-67] From the voltage profiles, it is apparent that the broadening of the anatase intercalation plateaus is responsible for the increase in capacity for the oxygen-deficient and water vapor atmospheres. The dQ/dV plots also correspond well to the voltage profiles (**Supporting Information**). One peak during charging was located at about 1.9 V with a faint plateau around 1.7 V, while two peaks were located at 1.5 and 1.75 V during discharge.

Further characterizations were conducted to investigate the contradictory trends presented by the electrical conductivity measurements and electrochemical performance

for the water vapor -treated sample. EIS was used to measure the Li diffusivity of the annealed samples **(**Figure 2.8a). The equivalent circuit shown in Figure 2.8b was fit to the experimentally obtained data to obtain the Li diffusivity (Table 2.3). The calculated diffusivities were comparable to values already reported in literature.[68-70] A term accounting for possible parasitic side reactions (*R2*) was included in the equivalent circuit to fit more closely with the experimental data, as the tested materials were uncycled and thus more sensitive to degradation.[71] From the fitting, it was found that the water vapor -treated sample had the largest Li diffusivity. The improvement of the Li diffusivity was particularly significant, as it was two orders of magnitude larger than the diffusivity of the O_2 control sample. The increased Li diffusivity helps justify the high specific capacity exhibited by the water vapor -treated sample. While Ti vacancies stabilized by the water vapor treatment decreased electrical conductivity, their presence facilitated Li ion diffusion.

Rate capability studies were also conducted to determine how the formation of the oxygen and Ti vacancies would affect the electrochemical performance of the TiO_2 nanotubes at elevated current rates (Figure 2.9). At C/20, the charge capacities for the N_2- and water vapor -treated samples were almost identical at 231.9 and 230.6 mAh/g, respectively. However, the performance began to change as the C rate was increased. At C/2, their behavior noticeably differs, as the N_2-treated sample had a charge capacity of 176.9 mAh/g, while the water vapor treatment had a lower capacity of 166.0 mAh/g. The most dramatic decrease in capacity occurred at the highest current rate of 5C. The N_2 treatment caused capacity to decrease to 103.5 mAh/g, but the water vapor -treated sample had its capacity drop sharply to 80.4 mAh/g, which was comparable to the O_2

control capacity of 80.5 mAh/g. The Ar-treated sample maintained its slightly higher capacity with respect to the control case at all C rates until 5C. All samples exhibited good capacity recovery after being subjected to the highest current rate. The results of the rate study suggest that the electrical conductivity of the samples plays a larger role in their performance at higher rates. The higher Li diffusivity in the water vapor -treated sample does not enable it to perform well at higher C rates, but the N_2-treated sample has adequate capacity at rates up to 5C. This indicates that a synergistic effect from both electronic and ionic conductivity is necessary to achieve high rate capability in intercalation oxide electrodes.

2.5 Conclusion

Oxygen and titanium vacancies can be generated in TiO_2 nanotubes by annealing under oxygen-deficient (Ar and N_2) and water vapor atmospheres. Oxygen vacancies cause the electrical conductivity of the samples to increase, while Ti vacancies result in a slight decrease of electrical conductivity as predicted by DFT calculations and evaluated through two-point electrical conductivity measurements and Mott-Schottky analysis. The formation of these defects was confirmed by Raman spectroscopy. Both kinds of defects result in an improvement in the specific capacity of the TiO_2 nanotubes when they are used as anodes in a Li-ion battery. The Ar- and N_2-treated samples have an increase in capacity by 10% and 25%, respectively, while the water vapor treatment results in a 24% capacity increase. The increase in capacity in Ar-and N_2-treated samples can be explained by increased electrical conductivity due to oxygen vacancies. On the other hand, the improved electrochemical properties in water vapor -treated sample can be attributed to facilitated Li ion diffusion caused by Ti vacancies. The capacity increase due to Ti

vacancy formation suggests that electrical conductivity may not be the most significant indicator as to whether battery performance can be improved. Both electronic and ionic conductivity in intercalation oxide electrode materials need to be considered to understand their charge storage and transport properties.

2.6 Figures and Tables

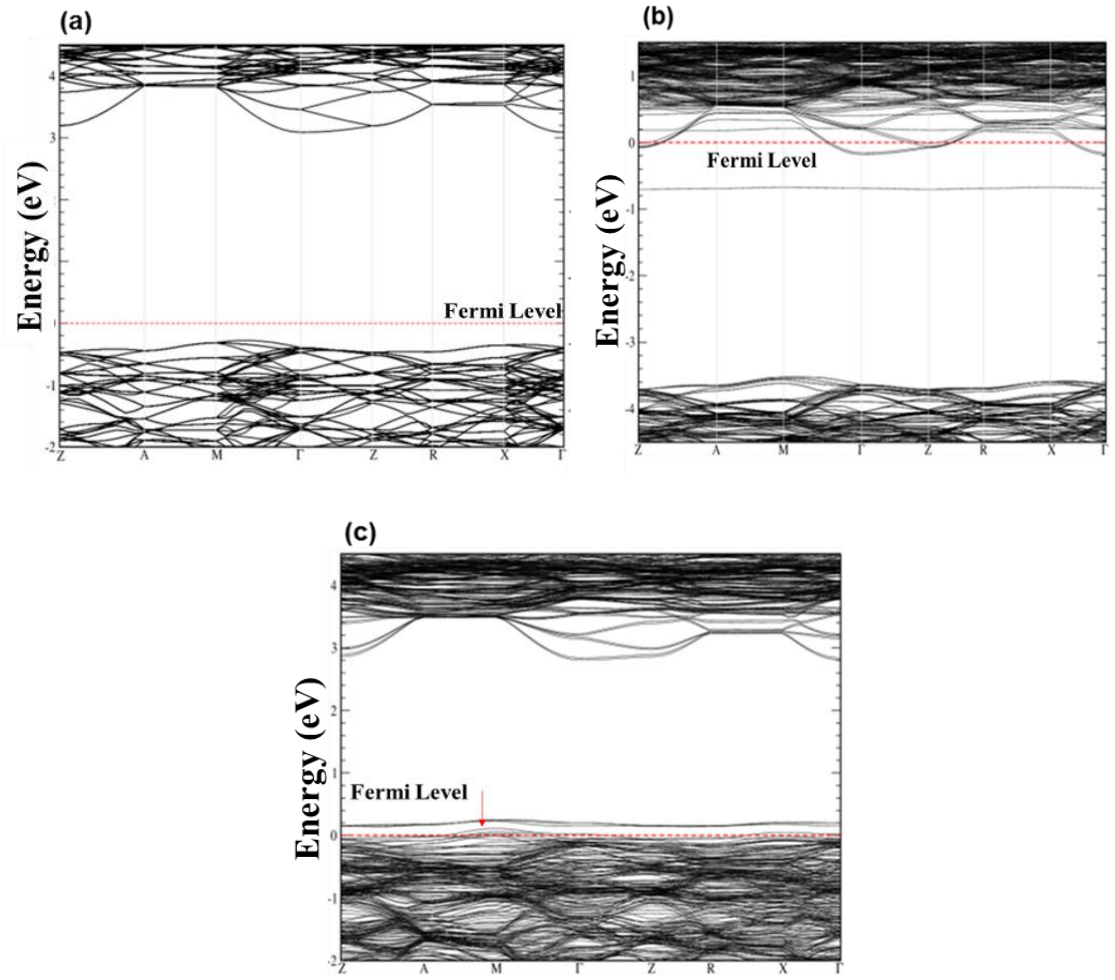

Figure 2.1. Theoretical band structures of a) pristine anatase TiO_2, b) anatase TiO_2 with O vacancy, and c) anatase TiO_2 with Ti vacancy stabilized with 4 protonated O sites. Red line indicates the Fermi energy. (In Submission)

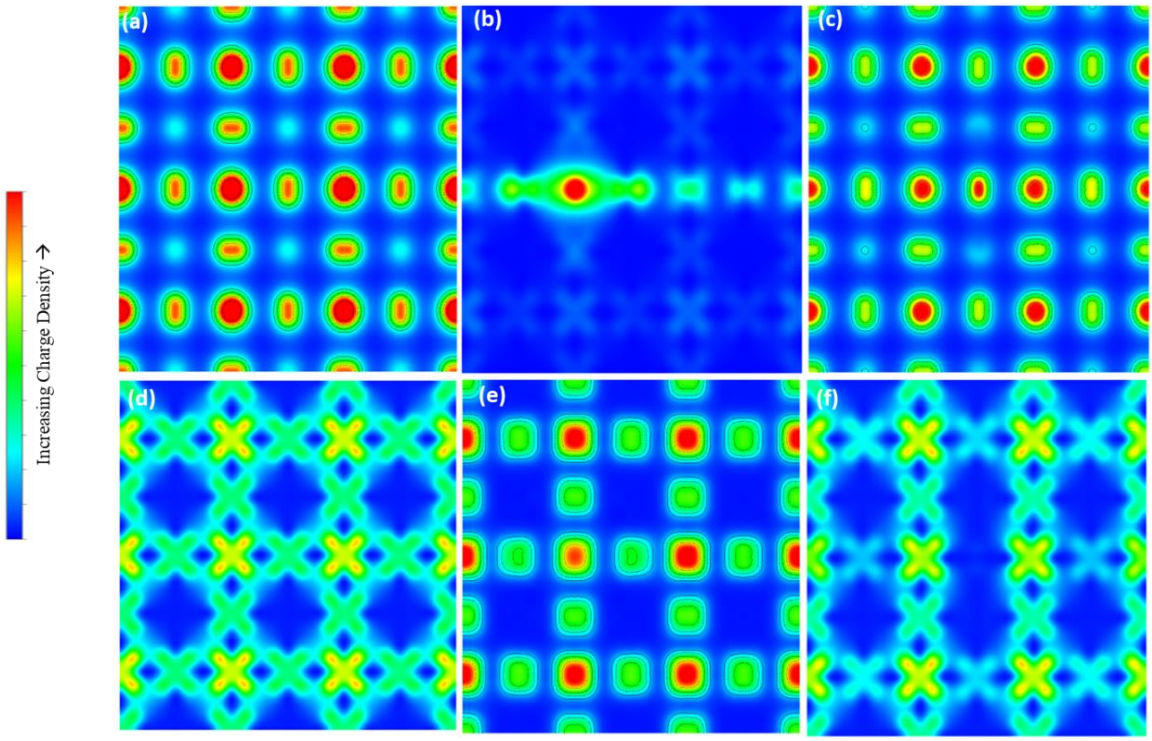

Figure 2.2. Partial charge density calculations for pristine anatase TiO_2 (a & d), anatase TiO_2 with O vacancy (b & e), anatase TiO_2 with Ti vacancy (c & f). Images a-c refer to the valence bands, d-f are the conduction bands. 2D images projected along the *c* axis. (In Submission)

Table 2.1: Charge carrier densities and flat-band potentials of anatase TiO_2 nanotubes annealed under different atmospheres. (In Submission)

Atmosphere	Charge Carrier Density (cm-3)	Flat-Band Potential (V)
O_2	2.01×10^{19}	-0.715
Ar	3.31×10^{19}	-0.688
N_2	8.06×10^{19}	-0.650
water vapor	1.49×10^{19}	-0.716

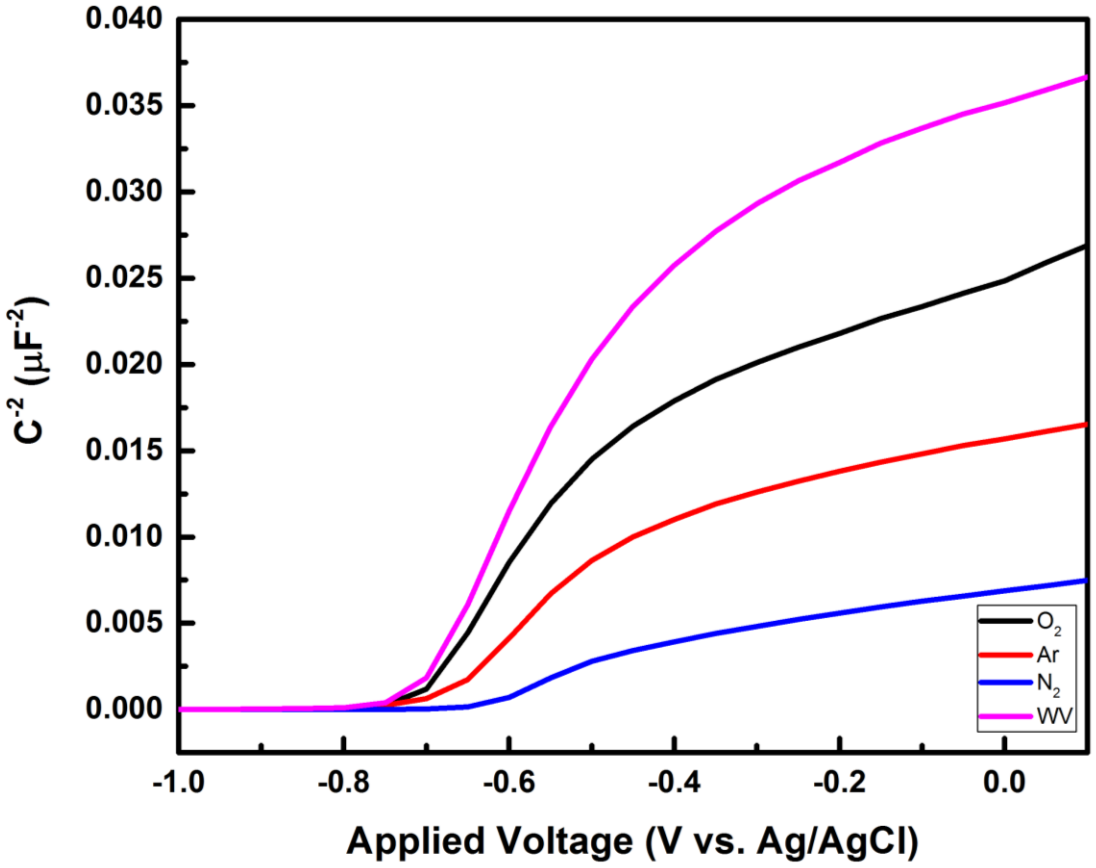

Figure 2.3. Mott-Schottky plots at 1.3 kHz of anatase TiO2 nanotubes annealed under different atmospheres. (In Submission)

Table 2.2: Electrical conductivity of TiO_2 nanotubes annealed under different atmospheres. (In Submission)

Atmosphere	Electrical Conductivity (S/m)
O_2	3.28×10^{-2}
Ar	6.86×10^{-2}
N_2	1.41
water vapor	6.33×10^{-3}

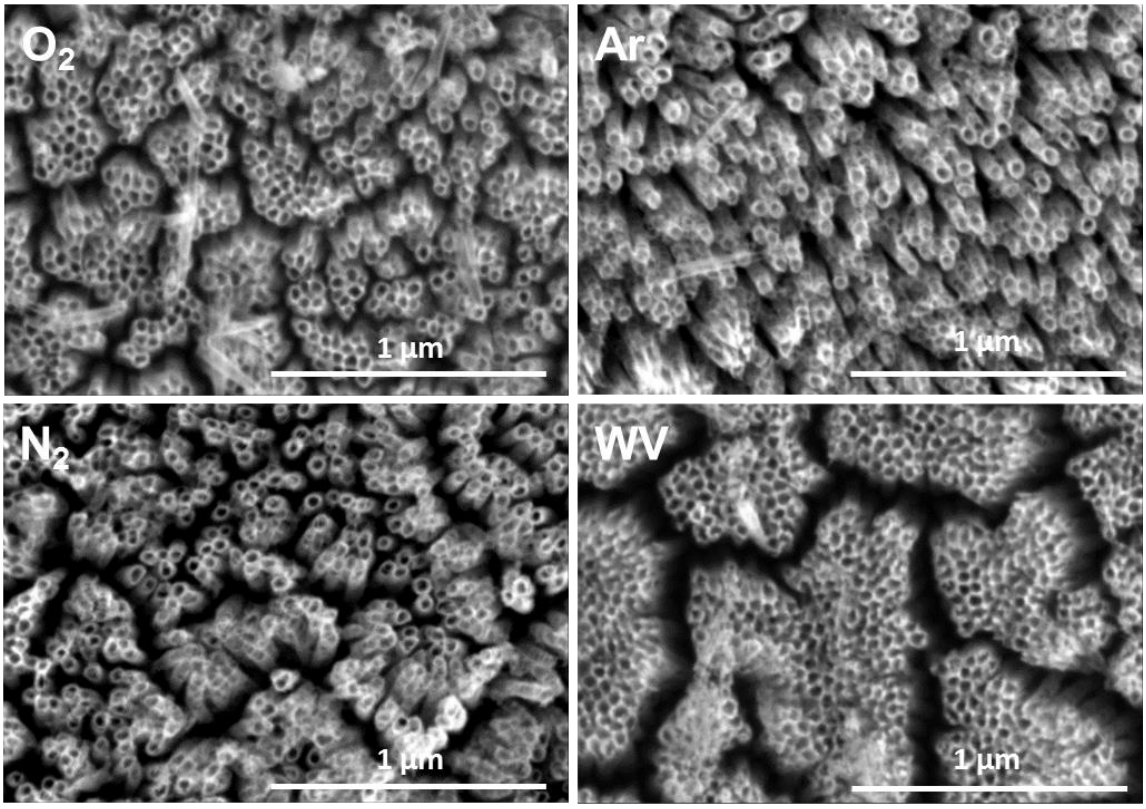

Figure 2.4. SEM images of anatase TiO_2 nanotubes annealed under different atmospheres. (In Submission)

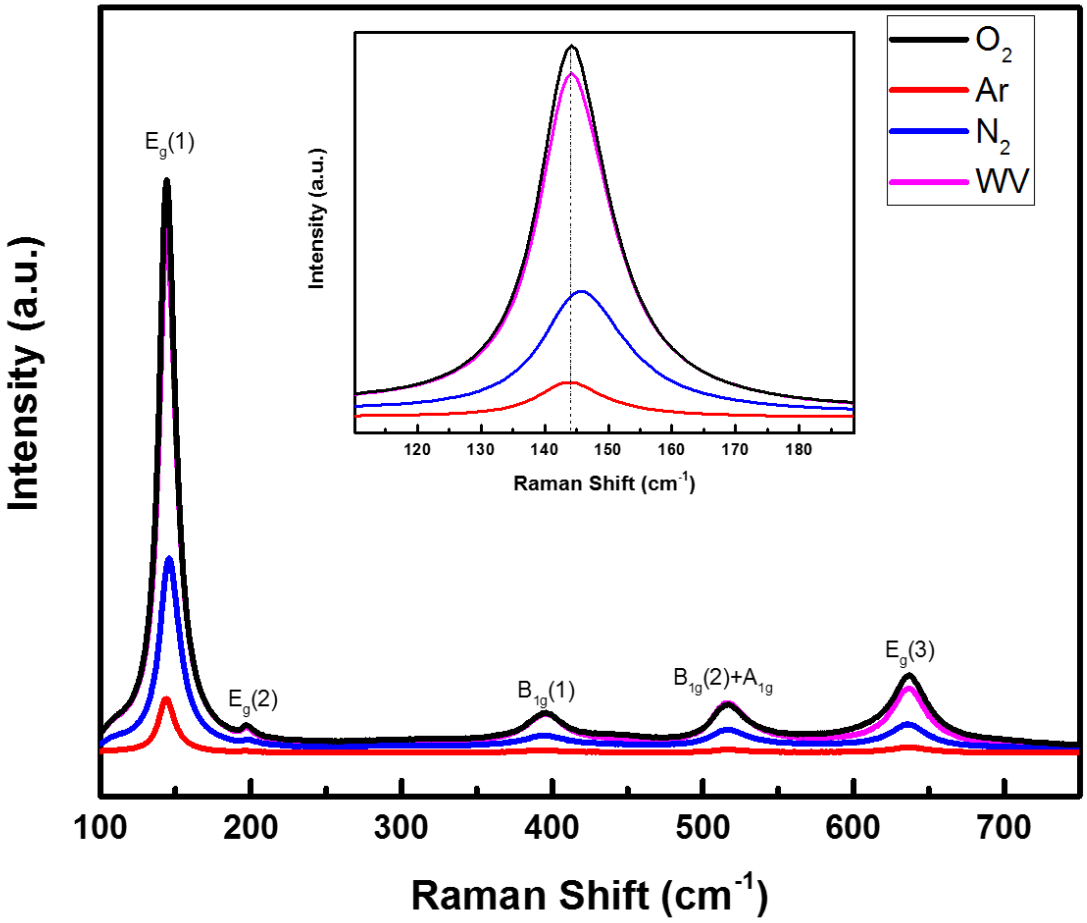

Figure 2.5. Raman spectroscopy of anatase TiO_2 nanotubes annealed under different atmospheres. Inset: Enlarged region near $E_g(1)$ peak. (In Submission)

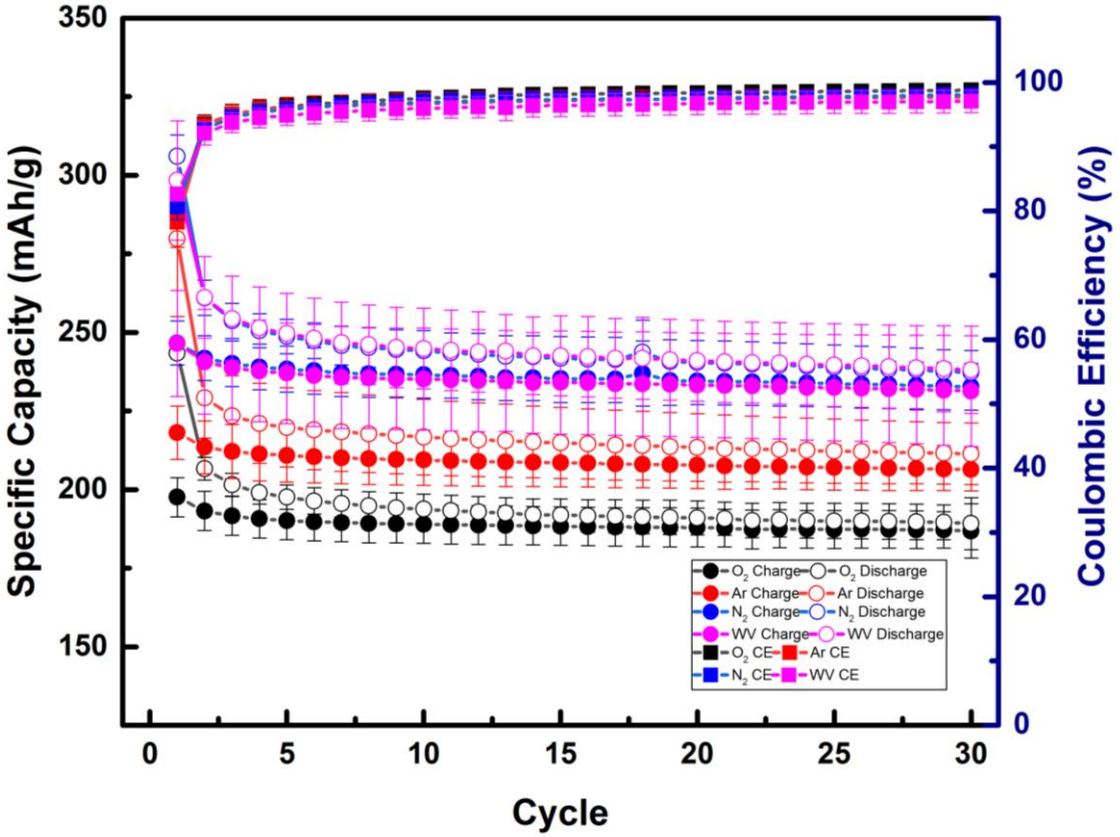

Figure 2.6. Specific capacities of anatase TiO_2 nanotube electrodes annealed under different atmospheres. Cells were cycled from 0.9 to 2.5 V at a theoretical C rate of C/20. (In Submission)

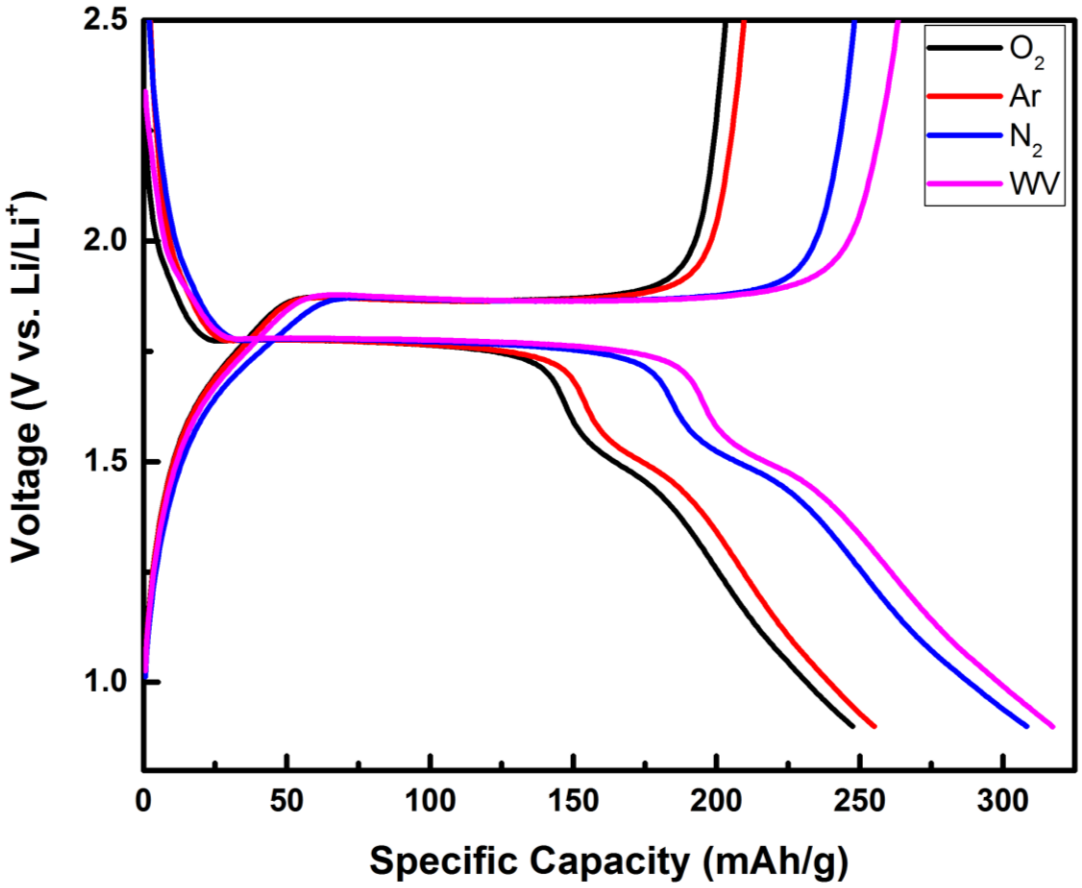

Figure 2.7. 1st cycle voltage profiles of anatase TiO_2 nanotube electrodes annealed under different atmospheres. Cells were cycled at a theoretical C rate of C/20. (In Submission)

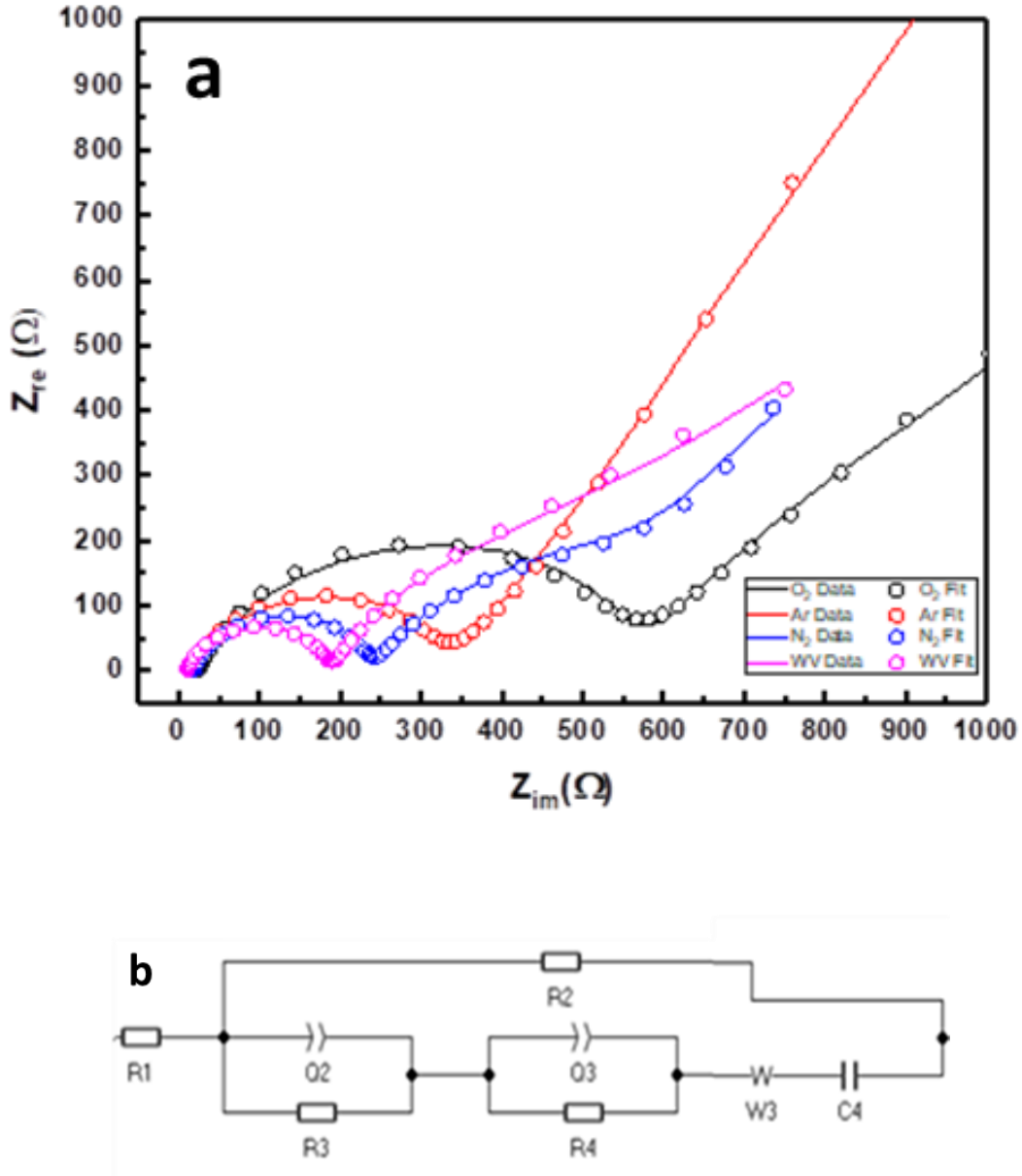

Figure 2.8. (a) Nyquist plots of anatase TiO_2 nanotubes annealed under different atmospheres. (b) Equivalent circuit used to fit impedance data. (In Submission)

Table 2.3: Li diffusivities obtained from Warburg factors derived from EIS fitting. (In Submission)

Atmosphere	Li Diffusivity (cm^2/s)
O_2	2.20×10^{-13}
Ar	2.32×10^{-13}
N_2	4.30×10^{-12}
water vapor	1.04×10^{-11}

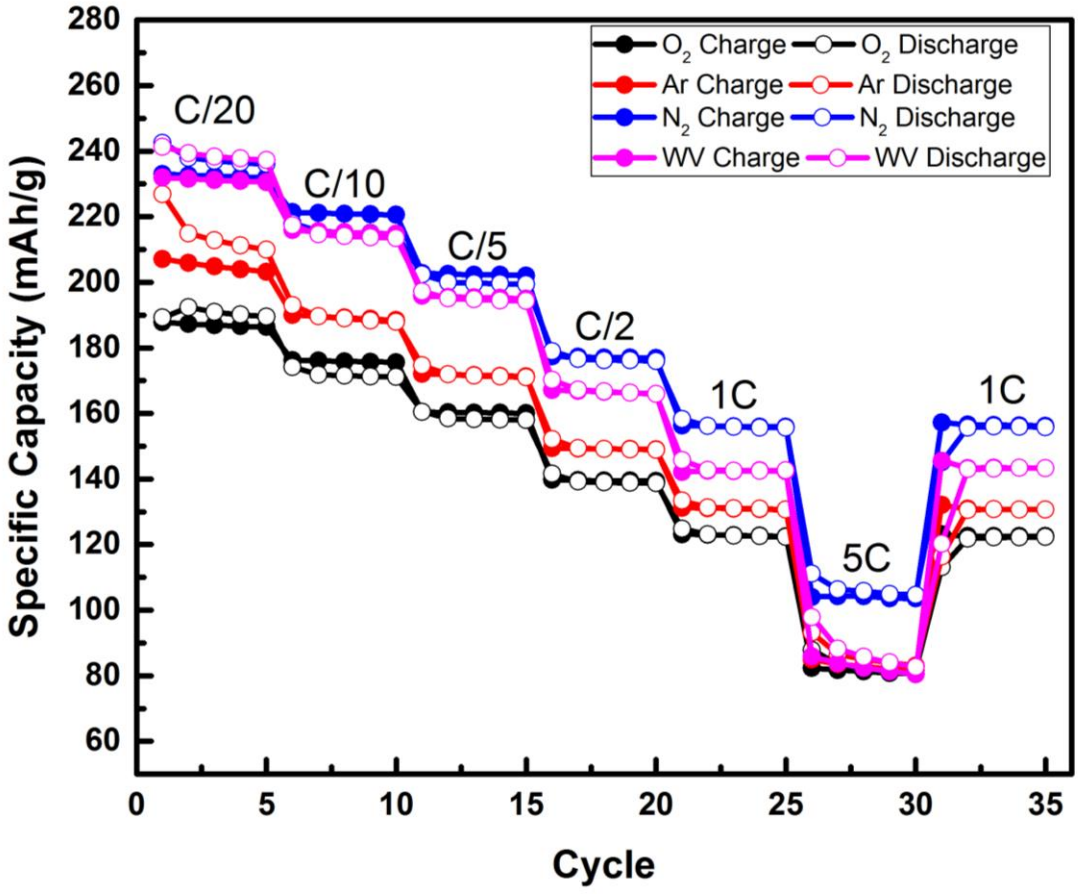

Figure 2.9. Rate study of anatase TiO_2 nanotube electrodes annealed under different atmospheres. (In Submission)

2.7 References

1. D. Deng, M. G. Kim, J. Y. Lee and J. Cho, *Energ Environ Sci*, 2009, 2, 818-837.
2. K. Lee, A. Mazare and P. Schmuki, *Chem Rev*, 2014, 114, 9385-9454.
3. R. M. Gao, Z. Jiao, Y. Wang, L. Q. Xu, S. S. Xia and H. J. Zhang, C*hem Eng J*, 2016, 304, 156-164.
4. M. Fehse and E. Ventosa, *Chempluschem*, 2015, 80, 785-795.
5. D. Bresser, B. Oschmann, M. N. Tahir, F. Mueller, I. Lieberwirth, W. Tremel, R. Zentel and S. Passerini, *J Electrochem Soc*, 2015, 162, A3013-A3020.
6. Y. Li, J. D. Luo, X. Y. Hu, X. F. Wang, J. C. Liang and K. F. Yu, J *Alloy Compd*, 2015, 651, 685-689.
7. G. S. Zakharova, C. Jahne, A. Popa, C. Taschner, T. Gemming, A. Leonhardt, B. Buchner and R. Klingeler, *J Phys Chem C*, 2012, 116, 8714-8720.
8. W. H. Ryu, D. H. Nam, Y. S. Ko, R. H. Kim and H. S. Kwon, *Electrochim Acta*, 2012, 61, 19-24.
9. J. Kim and J. Cho, *J Electrochem Soc*, 2007, 154, A542-A546.
10. S. K. Panda, Y. Yoon, H. S. Jung, W. S. Yoon and H. Shin, *J Power Sources*, 2012, 204, 162-167.
11. T. Su, Y. L. Yang, Y. Na, R. Q. Fan, L. Li, L. G. Wei, B. Yang and W. W. Cao, *ACS Appl Mater Inter*, 2015, 7, 3754-3763.
12. G. M. Wang, Y. Yang, D. D. Han and Y. Li, *Nano Today*, 2017, 13, 23-39.
13. B. Koo, H. Xiong, M. D. Slater, V. B. Prakapenka, M. Baasubramanian, P. Podsiadlo, C. S. Johnson, T. Rajh and E. V. Shevchenko, *Nano Lett*, 2012, 12, 2429-2435.
14. J. X. Qiu, S. Li, E. Gray, H. W. Liu, Q. F. Gu, C. H. Sun, C. Lai, H. J. Zhao and S. Q. Zhang, *J Phys Chem C*, 2014, 118, 8824-8830.

15. D. W. Liu, P. Xiao, Y. H. Zhang, B. B. Garcia, Q. F. Zhang, Q. Guo, R. Champion and G. Z. Cao, *J Phys Chem C*, 2008, 112, 11175-11180.

16. G. M. Wang, H. Y. Wang, Y. C. Ling, Y. C. Tang, X. Y. Yang, R. C. Fitzmorris, C. C. Wang, J. Z. Zhang and Y. Li, *Nano Lett*, 2011, 11, 3026-3033.

17. A. Ghicov, H. Tsuchiya, J. M. Macak and P. Schmuki, *Phys Status Solidi A*, 2006, 203, R28-R30.

18. R. S. Hyam, J. Lee, E. Cho, J. Khim and H. Lee, *J Nanosci Nanotechno*, 2012, 12, 8908-8912.

19. K. A. Smith, A. I. Savva, C. J. Deng, J. P. Wharry, S. Hwang, D. Su, Y. Q. Wang, J. Gong, T. Xu, D. P. Butt and H. Xiong, *J Mater Chem A*, 2017, 5, 11815-11824.

20. B. P. Uberuaga and X. M. Bai, *J Phys-Condens Mat*, 2011, 23.

21. B. P. Hahn, J. W. Long, A. N. Mansour, K. A. Pettigrew, M. S. Osofsky and D. R. Rolison, *Energ Environ Sci*, 2011, 4, 1495-1502.

22. S. J. Liu, Q. Ma, F. Gao, S. H. Song and S. Gao, *J Alloy Compd*, 2012, 543, 71-78.

23. A. Z. Liao, C. W. Wang, J. B. Chen, X. Q. Zhang, Y. Li and J. Wang, *Mater Res Bull*, 2015, 70, 988-994.

24. X. H. Lu, G. M. Wang, T. Zhai, M. H. Yu, J. Y. Gan, Y. X. Tong and Y. Li, *Nano Lett*, 2012, 12, 1690-1696.

25. L. X. Sang, Z. Y. Zhang and C. F. Ma, *Int J Hydrogen Energ*, 2011, 36, 4732-4738.

26. P. Xiao, D. W. Liu, B. B. Garcia, S. Sepehri, Y. H. Zhang and G. Z. Cao, *Sensor Actuat B-Chem*, 2008, 134, 367-372.

27. M. Salari, K. Konstantinov and H. K. Liu, *J Mater Chem*, 2011, 21, 5128-5133.

28. K. E. Swider-Lyons, C. T. Love and D. R. Rolison, *Solid State Ionics*, 2002, 152, 99-104.

29. H. Xiong, H. Yildirim, P. Podsiadlo, J. Zhang, V. B. Prakapenka, J. P. Greeley, E. V. Shevchenko, K. K. Zhuravlev, S. Tkachev, S. K. R. S. Sankaranarayanan and T. Rajh, *Phys Rev Lett*, 2013, 110.

30. B. P. Hahn, J. W. Long and D. R. Rolison, *Accounts Chem Res*, 2013, 46, 1181-1191.

31. G. Kresse and J. Furthmuller, *Physical Review B*, 1996, 54, 11169-11186.

32. J. P. Perdew, K. Burke and M. Ernzerhof, *Physical Review Letters*, 1996, 77, 3865-3868.

33. A. I. Liechtenstein, V. I. Anisimov and J. Zaanen, *Physical Review B*, 1995, 52, R5467-R5470.

34. M. Landmann, E. Rauls and W. G. Schmidt, *J Phys-Condens Mat*, 2012, 24.

35. Z. S. Lin, A. Orlov, R. M. Lambert and M. C. Payne, *J Phys Chem B*, 2005, 109, 20948-20952.

36. I. Nakamura, N. Negishi, S. Kutsuna, T. Ihara, S. Sugihara and E. Takeuchi, *J Mol Catal a-Chem*, 2000, 161, 205-212.

37. S. N. Phattalung, S. Limpijumnong and J. Yu, *Appl Catal B-Environ*, 2017, 200, 1-9.

38. S. Livraghi, M. C. Paganini, E. Giamello, A. Selloni, C. Di Valentin and G. Pacchioni, *J Am Chem Soc*, 2006, 128, 15666-15671.

39. F. Dong, W. R. Zhao, Z. B. Wu and S. Guo, *J Hazard Mater*, 2009, 162, 763-770.

40. R. Sanjines, H. Tang, H. Berger, F. Gozzo, G. Margaritondo and F. Levy, *J Appl Phys*, 1994, 75, 2945-2951.

41. B. Roh and D. D. Macdonald.

42. N. Baram and Y. Ein-Eli, *J Phys Chem C*, 2010, 114, 9781-9790.

43. H. Tang, K. Prasad, R. Sanjines, P. E. Schmid and F. Levy, *J Appl Phys*, 1994, 75, 2042-2047.

44. I. Hanzu, T. Djenizian and P. Knauth, *J Phys Chem C*, 2011, 115, 5989-5996.

45. S. Z. Islam, A. Reed, N. Wanninayake, D. Y. Kim and S. E. Rankin, *J Phys Chem C*, 2016, 120, 14069-14081.

46. L. K. Tsui and G. Zangari, *Electrochim Acta*, 2014, 121, 203-209.

47. V. K. Mahajan, M. Misra, K. S. Raja and S. K. Mohapatra, *J Phys D Appl Phys*, 2008, 41.

48. A. Tighineanu, T. Ruff, S. Albu, R. Hahn and P. Schmuki, *Chem Phys Lett*, 2010, 494, 260-263.

49. R. A. Spurr and H. Myers, *Anal Chem*, 1957, 29, 760-762.

50. O. K. Varghese, D. W. Gong, M. Paulose, C. A. Grimes and E. C. Dickey, J *Mater Res*, 2003, 18, 156-165.

51. M. D. Earle, *Phys Rev*, 1942, 61, 56-62.

52. T. Ohsaka, F. Izumi and Y. Fujiki, *J Raman Spectrosc*, 1978, 7, 321-324.

53. D. Georgescu, L. Baia, O. Ersen, M. Baia and S. Simon, *J Raman Spectrosc*, 2012, 43, 876-883.

54. S. Sahoo, A. K. Arora and V. Sridharan, *J Phys Chem C*, 2009, 113, 16927-16933.

55. V. Swamy, A. Kuznetsov, L. S. Dubrovinsky, R. A. Caruso, D. G. Shchukin and B. C. Muddle, *Phys Rev B*, 2005, 71.

56. J. C. Parker and R. W. Siegel, *J Mater Res*, 1990, 5, 1246-1252.

57. J. C. Parker and R. W. Siegel, *Appl Phys Lett*, 1990, 57, 943-945.

58. M. J. Scepanovic, M. U. Grujic-Brojcin, Z. D. Dohcevic-Mitrovic and Z. V. Popovic, *Mater Sci Forum*, 2006, 518, 101-106.

59. P. Scherrer, *Göttinger Nachrichten Math. Phys*., 1918, 2, 98-100.

60. J. G. Wang, P. Zhang, X. Li, J. Zhu and H. X. Li, *Appl Catal B-Environ*, 2013, 134, 198-204.

61. J. W. Xu, C. H. Jia, B. Cao and W. F. Zhang, *Electrochim Acta*, 2007, 52, 8044-8047.

62. K. Zhu, Q. Wang, J. H. Kim, A. A. Pesaran and A. J. Frank, *J Phys Chem C*, 2012, 116, 11895-11899.

63. H. T. Fang, M. Liu, D. W. Wang, T. Sun, D. S. Guan, F. Li, J. G. Zhou, T. K. Sham and H. M. Cheng, *Nanotechnology*, 2009, 20.

64. H. Han, T. Song, E. K. Lee, A. Devadoss, Y. Jeon, J. Ha, Y. C. Chung, Y. M. Choi, Y. G. Jung and U. Paik, *ACS Nano*, 2012, 6, 8308-8315.

65. U. Lafont, D. Carta, G. Mountjoy, A. V. Chadwick and E. M. Kelder, *J. Phus. Chem. C.*, 2010, 114, 1372-1378.

66. D. Bresser, E. Paillard, E. Binetti, S. Krueger, M. Striccoli, M. Winter and S. Passerini, *J. Power Sources*, 2012, 206, 301-309.

67. A. Moretti, G. T. Kim, D. Bresser, K. Renger, E. Paillard, R. Marassi, M. Winter and S. Passerini, *J. Power Sources*, 2013, 221, 419-426.

68. J. X. Duan, H. Y. Hou, X. X. Liu, C. X. Yan, S. Liu, R. J. Meng, Z. L. Hao, Y. Yao and Q. S. Liao, *J. Por. Mater.*, 2016, 23, 837-843.

69. A. Auer, E. Portenkirchner, T. Gotsch, C. Valero-Vidal, S. Penner and J. Kunze-Liebhauser, *ACS Appl. Mater. Inter.*, 2017, 9, 36828-36836.

70. M. Bratic, D. Jugovic, M. Mitric and N. Cvjeticanin, *J. Alloys Compd.*, 2017, 712, 90-96.

71. D. Aurbach, M. D. Levi, E. Levi, H. Teller, B. Markovsky, G. Salitra, U. Heider and L. Heider, *J. Electrochem. Soc.*, 1998, 145, 3024-3034.

2.8 Supporting Information

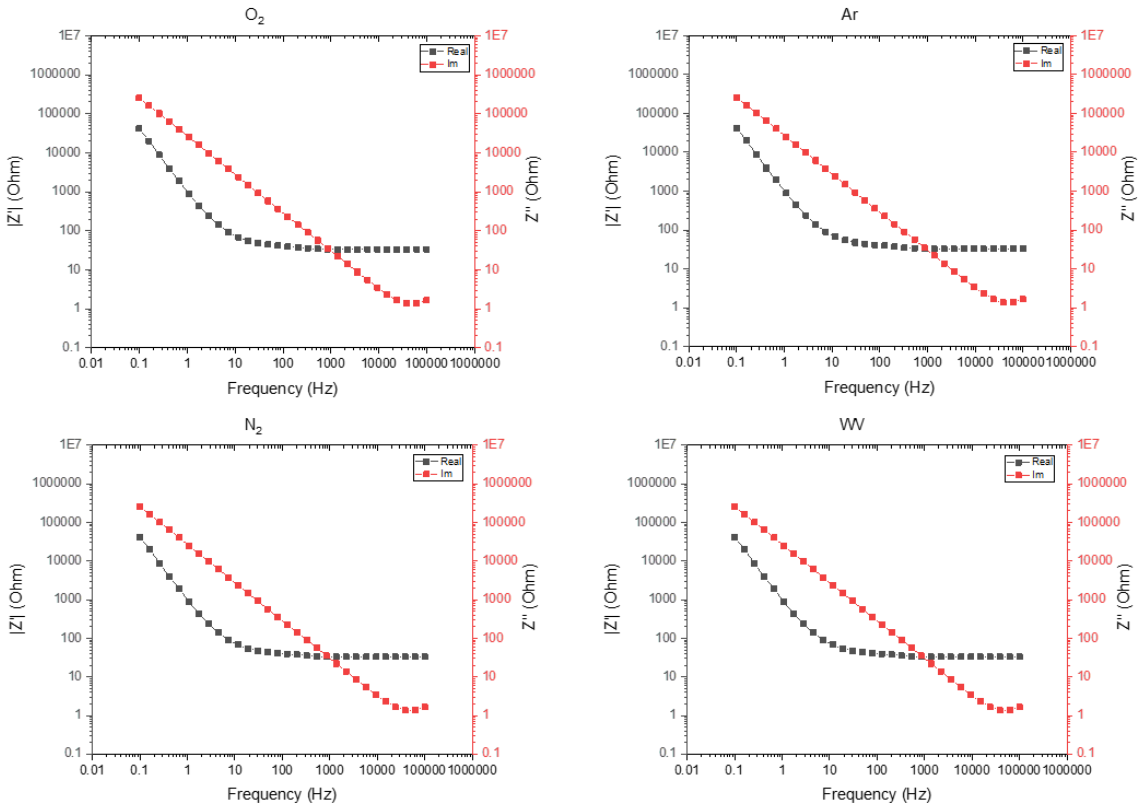

Figure S2.1. Bode plots of anatase TiO_2 nanotubes annealed in various atmospheres.

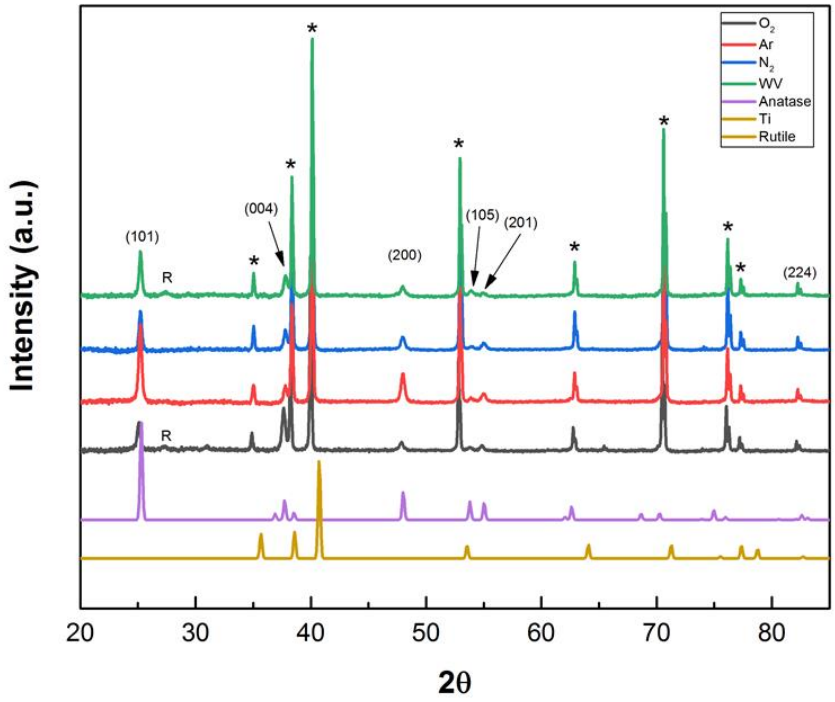

Figure S2.2. XRD spectra of anatase TiO_2 nanotubes annealed in different atmospheres. R indicates rutile (110) peak. * indicates metallic Ti.

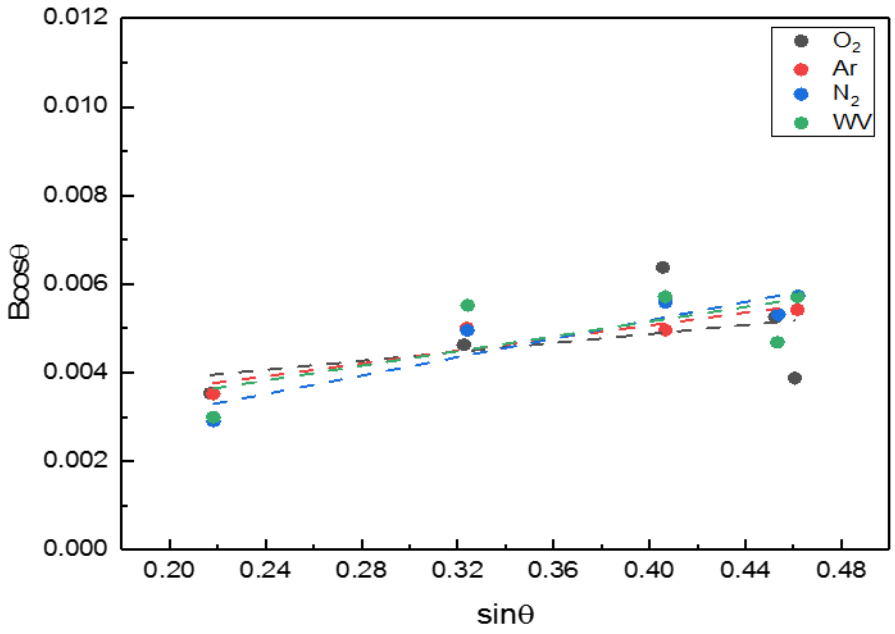

Figure S2.3. Williamson-Hall plots of anatase TiO_2 nanotubes annealed in different atmospheres.

Scherrer Equation: $L = \frac{K\lambda}{B\cos\theta}$ (S1)

Williamson-Hall Equation: $B\cos\theta = 4\epsilon\sin\theta + \frac{K\lambda}{L}$ (S2)

Table S2.1. Slope and strain values obtained from Williamson-Hall plots of anatase TiO_2 nanotubes annealed in different atmospheres. Crystallite size for each sample was calculated using the Scherrer equation.

Atmosphere	O_2	Ar	N_2	water vapor
Slope	0.00506	0.00718	0.01041	0.00831
Strain (%)	0.001265	0.001795	0.0026025	0.0020775
Crystallite Size (nm)	39	39	48	46

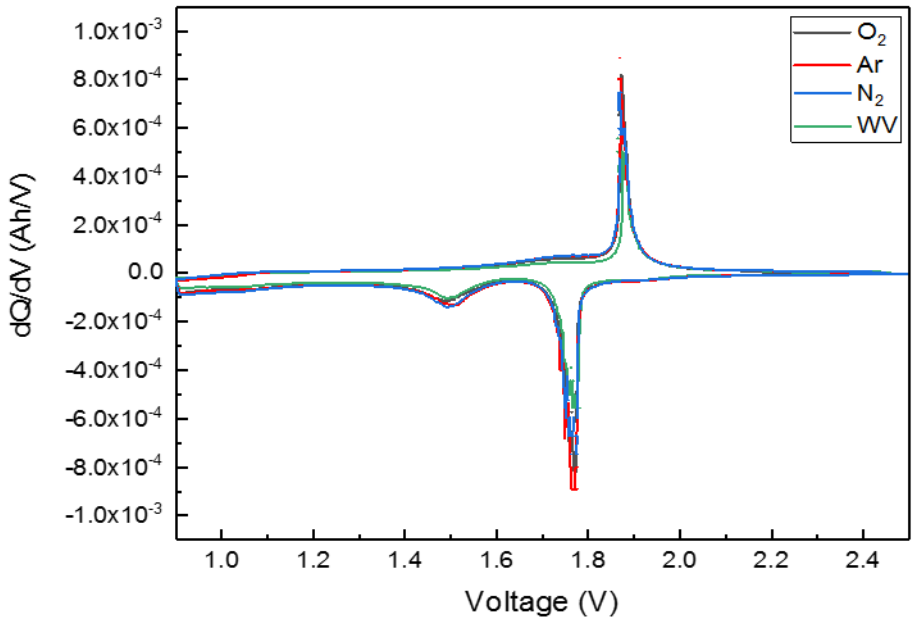

Figure S2.4. 1st cycle dQ/dV plots of anatase TiO_2 nanotubes annealed in different atmospheres.

CHAPTER THREE: EFFECTS OF PROTON IRRADIATION ON STRUCTURAL AND ELECTROCHEMICAL CHARGE STORAGE PROPERTIES OF TIO_2 NANOTUBE ELECTRODE FOR LITHIUM-ION BATTERIES

This chapter is published by The Royal Society of Chemistry in the *Journal of Materials Chemistry A* and should be referenced appropriately.

Reference:

K. Smith,[a] A. Savva,[a] J. Wharry,[b] S. Hwang,[c] D. Su,[c] Y. Wang,[d] D. Butt,[e] and H. Xiong[a] , " Effects of Proton Irradiation on TiO_2 Nanotube Electrode for Lithium-ion Batteries." *J. Mat. Chem. A.* **5** 11815-11824 (2017).

*This chapter includes modifications from the originally published version.

Effects of Proton Irradiation on Structural and Electrochemical Charge Storage Properties of TiO_2 Nanotube Electrode for Lithium-Ion Batteries

Kassiopeia A. Smith[a]

Andreas I. Savva[a]

Changjian Deng[a]

Janelle P. Wharry[b]

Sooyeon Hwang[c]

Dong Su[c]

Yongqiang Wang[d]

Jue Gong[e]

Tao Xu[e]

Darryl P. Butt[f]

Hui Xiong[a]

[a]*Micron School of Materials Science and Engineering, Boise State University, Boise ID 83725*

[b]*School of Nuclear Engineering, Purdue University, West Lafayette, IN 47907*

[c]*Center for Functional Materials, Brookhaven National Laboratory, Upton, NY*

[d]*Ion Beam Materials Laboratory, Los Alamos National Laboratory, Los Alamos, NM*

[e]*Department of Chemistry & Biochemistry, Northern Illinois University, Dekab, IL*

[f]*College of Mines and Earth Sciences, University of Utah, Salt Lake City, Utah*

3.1 Abstract

The effects of proton irradiation on nanostructured metal oxides have been investigated. Recent studies suggest that the presence of structural defects (e.g. vacancies and interstitials) in metal oxides may enhance the material's electrochemical charge storage capacity. A new approach to introduce defects in electrode materials is to use ion irradiation as it can produce a supersaturation of point defects in the target material. In this work we report the effect of low-energy proton irradiation on amorphous TiO_2 nanotube electrodes at both room temperature and high temperature (250 ˚C). Upon room temperature irradiation the nanotubes demonstrate an irradiation-induced phase transformation to a mixture of amorphous, anatase, and rutile domains while showing a 35% reduction in capacity compared to anatase TiO_2. On the other hand, the high temperature proton irradiation induced a disordered rutile phase within the nanotubes as characterized by Raman spectroscopy and transmission electron microscopy, which displays an improved capacity by 20% at ~ 240 mAh g-1 as well as improved rate capability compared to non-irradiated anatase sample. Voltammetric sweep data was used to determine the contributions from diffusion-limited intercalation and capacitive processes and it was found that the electrodes after irradiation has more contributions from diffusion in lithium charge storage. Our work suggests that tailoring the defect generation through ion irradiation within metal oxide electrodes could present a new avenue for design of advanced electrode materials.

3.2 Introduction

Titanium-based oxide materials have attracted intense attention as promising anode materials for Li-ion batteries due to their excellent cycling stability, low cost,

abundance and environmentally benign nature.[1-4] Ti-based oxide is one of the few metal oxide materials that intercalates Li ions at relatively low voltages as anodes (~ 1.5 – 1.8 V vs. Li/Li^+) for a decent output voltage between cathodes and has been found as a safe alternative to the graphite anode. In addition, TiO_2 has a comparable theoretical specific capacity at 335 mAh/g or 1.0 Li per TiO_2, compared to graphite (theoretical capacity: 372 mAh/g). The cycling stability of TiO_2 is superior compared to other conversion-type metal oxide anodes such as iron oxide. Among various TiO_2 polymorphs investigated for their electrochemical properties, researchers have found that rutile (space group $P4_2/mnm$), anatase ($I4_1/amd$), brookite (*Pbca*) and TiO_2-B (*C2/m*) shows lithium electrochemical reactivity.

The first attempts at using TiO_2 as a durable and safe electrode material focused on microcrystalline TiO_2 materials such as rutile, anatase and TiO_2-B.[5] These electrodes showed moderate specific capacities (the maximum Li uptake of 0.5 Li/Ti for anatase and TiO_2-B, and no activity for rutile)[5] due to the limited room temperature reactivity and conductivity at microscale. Such limitation in room temperature reactivity of bulk TiO_2 have spurred rapid development in nanostructured TiO_2 materials, leading to significant improvements in electrochemical properties.[2, 6-13] Nanosizing of TiO_2 has significantly improved the electrochemical reactivity toward Li at room temperature due to enhanced kinetics.[2, 6-16] Upon lithium insertion, the donated charge is distributed between the Ti and O ions, leading to structural deformation.

Recent studies have investigated enhanced electrochemical charge storage in electrodes that contain intentional structural defects (e.g. vacancies and interstitials).[17-19] Our recent work, along with that of others, has suggested that nanoscale transition metal

oxides, which have structural defects with local disorder, can offer enhanced capacity and structural stability under stress.[17, 20-25] Further, researchers have demonstrated that synthetic methods such as doping[17, 26] and ion irradiation[17, 26-35] can introduce defects that could enhance the charge storage of metal oxides. A new approach to introduce defects in electrode materials is to utilize irradiation to produce a supersaturation of defects in the target material.[36]

It is widely recognized that ion irradiation, i.e. the bombardment of a target with keV–MeV ions, introduces defects and regions of lattice disorder in solids.[36] Furthermore, electron and light ion irradiation (e.g. proton) have been shown by molecular dynamics to predominantly produce point defects in rutile and anatase TiO_2.[37, 38] Through these theoretical studies, it was found that grain boundaries in both polymorphs behave as sinks for all types of point defects.[37] From this, it may be inferred that nanostructured materials could have high radiation resistance owing to their large volume fraction of grain boundaries. Nevertheless, the defect properties and the defect dynamics are largely unknown in irradiated nanostructured TiO_2 materials. The nature of structural changes upon irradiation also depends on the incoming ion species. Hartmann et al.[39] observed amorphization of single crystal rutile TiO_2 at room temperature when irradiated with He^+ ions, but found that temperatures under 200 K were necessary to amorphize the same materials under heavy noble gas ions. It was suggested that He^+ ions create a number of small cascades which allow point defects to accumulate in the target material.

In the present work, we investigated the effect of proton irradiation both at room temperature and at elevated temperature on amorphous TiO_2 nanotube (TiO_2-NT)

electrodes. TiO_2 has been widely studied as an anode material for Li-ion batteries. However, to the best of the authors' knowledge no work has been done to study the electrochemical charge storage properties of ion-irradiated nanostructured TiO_2. In addition, no work has been done to investigate the ion irradiation effect on nanoscale amorphous ceramics. Recently Schmuki et al.[40] explored proton irradiation induced defects of anatase TiO_2-NT films for photocatalytic H_2 evolution. It was shown that proton implantation into anatase TiO_2-NT induced specific defects and created intrinsic co-catalytic centers for improved photocatalytic activity. Hence, proton irradiation could be an effective tool for defect-driven materials with enhanced functionality.

In this work, we conducted proton implantation at an energy of 200 keV with an average dose of 0.17 displacements per atom (dpa) on amorphous TiO_2-NT electrodes both at room temperature and at 250˚C. Structural characterizations by Raman spectroscopy and transmission electron microscopy (TEM) suggest that proton irradiation induces phase transformation in the amorphous TiO_2-NT electrode. For the sample irradiated at room temperature (RT), irradiation a phase transformation from amorphous to a mixture of disordered anatase and rutile phase was observed. On the other hand, for the sample irradiated at 250˚C (HT) we observed a phase transformation to a primarily disordered rutile phase.

It is interesting to note that no work has been shown for synthesis of rutile TiO_2-NT prepared by anodization. In general, anatase TiO_2-NT can be prepared by thermally annealing as-prepared amorphous TiO_2-NT at approximately 450 ˚C.[41] However, the same thermal treatment is not viable to synthesize rutile TiO_2-NT as the tubes tend to collapse at the phase transition temperature for rutile (> 600˚C). Therefore, the proton

implantation approach might open a new synthetic pathway to create anodized rutile TiO_2-NT. We have also conducted electrochemical characterization of the irradiated TiO_2-NT electrodes, where we observe the charge storage behavior of the TiO_2-NT electrode change. Galvanostatic intermittent titration technique (GITT) measurements were conducted and it was found that the sample irradiated at 250˚C exhibits enhanced diffusion compared to the RT sample. The sample irradiated at 250˚C also demonstrates improved capacity at low rate and superior rate capability compared to both the RT irradiated sample and the anatase TiO_2-NT. Our results suggest that by tailoring the irradiation condition it is possible to create nanostructured metal oxide electrodes with enhanced functionality.

3.3 Experimental

3.3.1 Materials

TiO_2 nanotubes were synthesized by electrochemical anodization described previously.[24, 68] To summarize, pure titanium foil (0.0127mm, 99.8%, Alfa Aesar) was cleaned by a three step sonication in acetone, isopropyl alcohol and D.I. water before anodization. The back of the Ti foil was protected by tape to ensure uniform current distribution. The anodization was carried out in a two-electrode cell with Pt mesh as the counter electrode. The anodization was carried out for 10 minutes under a constant voltage of 15 V in an electrolyte of 0.36 M ammonium fluoride (Aldrich) in 95 vol % formamide (Fisher) and 5 vol % DI water. The anodized samples were then ultrasonically cleaned in DI water for 30 seconds. Anatase TiO_2 was made by annealing the as-prepared TiO_2 NTs in a mixture of ultra-pure 20% O_2/balance Ar gas at 450°C for 4 hours.

3.3.2 Irradiation

The TiO_2-NT films were irradiated with 200 keV protons in a 200 kV Varian ion implanter at Los Alamos National Laboratory. The accelerator beam line was maintained at 1.8×10^{-7} torr throughout the experiment. Specimens were mounted onto a copper irradiation stage, which was electrically isolated from the accelerator beam line, to allow for accurate charge collection. Thermocouples were mounted onto the copper stage and used to control the temperatures throughout the implantation. During irradiation, the focused proton beam was raster-scanned across samples, with the resulting beam current density of 9.3×10^{12} ions cm^{-2}, yielding a dose rate of 3.2×10^{-6} dpa s^{-1}.

The damage depth profile and displacement damage were calculated using the Stopping and Range of Ions in Matter (SRIM-2013) program using the "Detailed Calculation" mode and the displacements were obtained from the resulting vacancy.txt file. One downside of this software is the inability to model precise nano-structures, so for these calculations a compact layer of TiO_2 (density of 3.89 g cm^{-3}) was used. Displacement energy for titanium and oxygen were set to 25 and 28 eV respectively. The 200 keV proton flux produces a relatively uniform damage profile through ~1 μm (Figure 3.1), which ensured that the entire length of the nanotubes would receive a consistent irradiation dose. Using the "Detailed Calculation" mode the number of displacements per ion-angstrom was 3.6×10^{-3} vacancies per ang-ion at the peak implantation depth, which was converted to a fluence of 2.18×10^{17} ions cm^{-2} to reach the average accumulated proton dose of 0.17 dpa.

3.3.3 Electrochemical Testing

Li half-cells were assembled in coin-type cells (Hohsen 2032) with Li metal foil (FMC Lithium) as the negative electrode, a 2325 type polymer separator, and 1.2 M $LiPF_6$ in ethylene carbonate/ethyl methyl carbonate (3:7 weight ratio) electrolyte (Tomiyama) . Half-cells were cycled galvanostatically at varying currents between 2.5 and 0.9 V vs. Li/Li^+ using an automated Maccor battery tester at ambient temperatures. Three-electrode cells were made using ECC-Ref cells (EL-Cell) with Lithium metal as both counter and reference electrode. GITT and cyclic voltammetry (CV) measurements were carried out in three-electrode cells using a Bio-Logic Science Instruments potentiostat/galvanostat. GITT measurements consisted of a series of current pulses of 8μA for 30 min and a 2 h rest period until the voltage reached a cut-off value of 1 V. CV measurements for all samples were performed with the potential window of 0.9-2.5 V at the scan rates of 0.5, 1, 2, 5, and 10 mV s^{-1}. All cell assembly and disassembly operations were performed in an Ar-filled glovebox with oxygen levels below 0.5 ppm. The mass of the TiO_2 nanotube films was determined by peeling off the nanotube film from the Ti substrate using adhesive tape and measuring the weight difference. The remaining substrate was examined by SEM to ensure no residual TiO_2 nanotubes were left on the substrate.

3.3.4 Electron Microscopy

Scanning electron microscopy (SEM) images were recorded with a FEI Teneo field emission microscope operating at 5 kV. Transmission electron microscopy (TEM) images, including HRTEM, SAED, and EELS spectra, were recorded with JEOL JEM-2100F operating at 200 kV and Gatan GIF Tridiem at Brookhaven National Laboratory.

3.3.5 Raman Spectroscopy

Raman spectroscopy was conducted using a Horiba Scientific LabRAM HR Evolution spectrometer using the 442 nm He:Cd laser with signal accumulations of three 30s scans. After instrument calibration, samples were scanned at room temperature under ambient conditions. The incident laser power was 100 mW, and samples were viewed at a magnification of 100x. Scattered light was collected with a thermoelectrically cooled Si CCD detector. Data was acquired using the LabSpec 6 Spectroscopy Suite software, and analyzed using OriginPro software.

3.3.6 Electrical Conductivity Measurements

Gold pads (2mm in diameter) were thermally evaporated on top of the masked TiO_2-nanotubes-on-Ti substrates at a grazing angle of 30 degree to limit the gold-nanowire contact only at the apex of the nanotubes without touching the metal Ti at the bottom, thus to avoid any short circuits. The conductance of different substrates were studied from the current-voltage (I-V) curves measured by connecting the gold pads and Ti substrates using a Gamry reference 600 potentiostat.

3.4 Results and Discussion

Densely packed, vertically oriented TiO_2-NTs were synthesized by an electrochemical anodization method described previously.[24] TiO_2-NTs are inherently connected to the Ti substrate - the current collector - eliminating the need for conductive carbon additives and polymer binders which are typically used in electrodes for lithium-ion batteries. The SEM top-view image in Figure 3.2a shows the TiO_2-NT after the anodization. The as-prepared TiO_2-NT film is ~1 μm in length (Supporting Information Figure S3.1) and has an outer diameter of ~ 60 nm with a ~ 10 nm wall thickness. The

stability of the TiO_2-NT morphology after proton irradiation was investigated by SEM. Figure 3.2b shows the top-view SEM image of the TiO_2-NT film after proton irradiation at room temperature, exhibiting structural integrity of the nanotubes after irradiation. The inset of Figure 3.2b is a representative TEM image of the tube morphology after irradiation, showing no degradation.

TiO_2-NT films were ion implanted with protons (p^+) at an energy of 200 keV with a fluence of 2.18×10^{17} ions/cm^2 to achieve the average accumulated proton dose of 0.17 dpa. For these experiments, implantations were carried out either at room temperature or at 250°C. Figure 3.1 shows the damage depth distribution for compact TiO_2 according to Monte Carlo simulations using SRIM 2013.[42] In these calculations, the implantation leads to an implant zone reaching approximately 1.3 μm below the sample surface with a maximum of p^+ implanted in a depth of 1.25 μm. The simulation is done based on compact or bulk materials, and it has been suggested by Schmuki et al.[40] that the actual damage depth in TiO_2-NT film may be greater due to the porosity of the film. The nanotube length was chosen such that there is minimum variation in irradiation along the full length of the tube, i.e., tube length is less than the depth of the damage peak.

The as-prepared anatase and irradiated samples were evaluated using Raman spectroscopy for their phase composition as well as the degree of order-disorder at short range. Raman spectroscopy is a powerful tool used to investigate the structure and order-disorder transition of TiO_2 and its polymorphs.[43-49] Anatase has a tetragonal structure (space group $I4_1$ / amd) and is comprised of two TiO_2 units per primitive cell, leading to six Raman active modes in the vibrational spectrum: three E_g modes centered around 144, 196, 639 cm^{-1} (designated at $E_{g(1)}$, $E_{g(2)}$ and $E_{g(3)}$ here, respectively), two B_{1g} modes

centered around 397 and 519 cm^{-1} (designated at $B_{1g(1)}$, and $B_{1g(2)}$ here, respectively), and an A_{1g} mode at 513 cm^{-1}. Due to the overlap of $B_{1g(2)}$ and A_{1g} modes the symmetry assignment of the two modes has been difficult. On the other hand, rutile (space group $P4_2$ /mnm) has only four Raman active modes: B_{1g} (143 cm^{-1}), E_g (447 cm^{-1}), A_{1g} (612 cm^{-1}), and B_{2g} (826 cm^{-1}). The rutile spectra also exhibits several broad combination bands exhibited around 250 cm^{-1}, 360 cm^{-1}, 550 cm^{-1}, and 680 cm^{-1}.[50, 51] Note that the $E_{g(1)}$ mode of anatase and B_{1g} mode of rutile appear around the same frequency. Consequently in a two-phase sample, the 144 cm^{-1} peak can have the contribution from both modes.

Figure 3.3 shows the Raman spectra of non-irradiated anatase, as-prepared amorphous and the irradiated TiO_2-NT samples. The broad Raman spectra of the as-prepared TiO_2-NT is indicative of its amorphous nature, which contains a variety of phonon scattering centers. In the non-irradiated anatase control sample, five well-defined peaks are observed at around 143.3, 196.5, 395, 514.5, and 637.2 cm^{-1}, corresponding to the vibration modes of anatase phase. The presence of well-defined, high intensity peaks in the pristine anatase NT suggests high order crystallinity with little disorder.

In Raman spectroscopy, the phonon confinement model links the *q* vector selection rule for the excitation of Raman active phonons with the degree of ordering and crystallite size.[48, 49, 51] In an ideal crystal with long-range order, there would be phonon conservation so that only the optic zones near the Brillouin zone (BZ) center are observable, allowing for sharp and well defined peaks. However, when a material lacks long range order, or in this case is nanocrystalline, the selection rule is relaxed resulting in peak broadening and possible shifts as a result of the increased range of *q* vectors.[50-53]

In first-order Raman scattering, the modification of Raman line shape for a given phonon mode as a function of crystallite size is determined by the behavior of the dispersion slope away from the BZ center (scattering vector $q \approx 0$). A negative slope would cause a red-shifted Raman peak, while a positive slope would result in a blue-shifted Raman peak, in addition to an asymmetric peak broadening when the crystallite size is reduced.[48]

Upon proton irradiation, both the HT and RT samples show an increase in crystallinity from the original amorphous state. The peaks present after irradiation are broad compared to a purely crystalline structure, indicating a disordered lattice.[45] In anatase TiO_2 nanocrystals, it has been found that $B_{1g(1)}$ (396 cm^{-1}) and $E_{g(3)}$ (639 cm^{-1}) modes are the most sensitive to the presence of defects compared to the most intense $E_{g(1)}$ (144 cm^{-1}) mode.[45] In the sample irradiated at room temperature (TiO_2-NT (RT)), the $E_{g(1)}$ and the $E_{g(3)}$ peaks of the anatase structure are observable but weak due to the lack of long range order. Two broad peaks are present at 435.4 and 607.5 cm^{-1}. The peak at 435.4 cm^{-1} can have contribution from both the $B_{1g(1)}$ mode in anatase and E_g mode in a new rutile phase. The peak at 607.5 cm^{-1} is assigned to the A_{1g} mode of a new rutile phase. We have also observed the phase transformation in the TEM study, which will be discussed later. It is well known that irradiation can create point defects (vacancies and interstitials) in materials. This result suggests an irradiation-assisted phase transformation from amorphous to anatase and rutile, which is consistent with observations of thermal spike-induced nano-phase transformations in localized regions within ion tracks in ceramic materials.[54-57] Because these irradiation-assisted phase transformations are by

nature highly localized and nanoscopic, in contrast to a bulk annealing-induced phase transformation, a combination of disordered and ordered phases can be found.

For the irradiated sample at 250˚C (TiO_2-NT (HT)), there is a distinct peak at 148.9 cm^{-1}, which can be ascribed to either anatase or rutile phase. The full width at half maximum (FWHM) of the peak is 20 cm^{-1} and is broader than the FWHM of the $E_{g(1)}$ peak of the pure anatase TiO_2 sample. The strongest rutile vibrational mode A_{1g} [50] is present at 607 cm^{-1} and is more defined in the TiO_2-NT (HT) sample compared to the TiO_2-NT (RT) sample. In fact, the overall spectrum begins to more closely resemble the rutile structure including several rutile combinational bands which are centered at approximately 250, 350, 540, and 680 cm^{-1}.[50] Much like the room temperature irradiation case, these results can also be explained by thermal spikes from ion irradiation. However, the higher irradiation temperature, in combination with the thermal spikes, can more effectively provide sufficient thermal energy to induce the rutile phase transformation. It should be noted that no result on rutile TiO_2 nanotubes formed by anodization has been reported and the proton irradiation at higher temperature could open a new avenue for rutile nanotube synthesis. In both cases after irradiation the peaks are broad and have low intensities suggesting the presence of disordered anatase and rutile.[45, 49]

The electrical conductivities of the pristine anatase and irradiated TiO_2-NT samples were evaluated using a two-point conductivity measurement.[58] There is no significant difference between non-irradiated amorphous and irradiated TiO_2-NT samples and their conductivities are significantly lower (~ 2 magnitude of order) than that of the non-irradiated anatase. The results indicate that although irradiation can increase charge

carrier density[40] the mobility of those carriers is not necessarily increased, therefore increase in electrical conductivity is not observed in irradiated samples.

TEM was used to study the phase evolution of proton irradiated TiO_2-NT samples. Low magnification (4a, d, g), high resolution TEM (HRTEM) (4b, e, h) and SAED pattern (4c, f, i) images of the non-irradiated anatase and proton implanted nanotubes are shown in Figure 3.4. The low magnification images show that even after irradiation, the overall tube structure is well maintained and there is no visual evidence of loss of structural integrity. Since TiO_2 NT samples were acquired by scraping them from the substrate for TEM observation, full length is not observed under this technique. Figure 3.4b shows that the anatase sample is composed of randomly oriented nanocrystals, which have anatase structure according to SAED at Fig. 3.4c. After irradiation at RT, HRTEM image shows that there is no long-range order in the RT sample and it still appears predominantly amorphous (Fig. 3.4e). SAED of TiO_2-NT (RT) sample (Fig. 3.4f) presents faint rings originating from both anatase and rutile structures, implying that the amorphous structure of TiO_2 has transformed to a partially crystalline structure with short-range-ordered anatase and rutile after irradiation at RT. On the other hand, proton implantation at high temperature leads to the phase transformation to rutile as presented by SAED (Fig. 3.4i). The HRTEM image shows that the NT sample has crystalline phase with a number of defects. In other words, phase transformation to rutile is accompanied with evolution of defects within NT samples during irradiation at high temperature.

Structural and chemical properties of TiO_2-NT before and after proton implantation are further characterized with electron energy loss spectroscopy (EELS)

(Figure 3.5). Ti $L_{2,3}$ edge of crystalline TiO_2 is composed of well-separated L_3 and L_2 edges, which originated from the 2p core-hole spin-orbit coupling. Each L_3 and L_2 edge is also divided into two edges by the strong crystal-field splitting.[59] Crystal-field splitting in L_3 and L_2 edges of anatase and HT irradiated samples demonstrates that these samples have a similar chemical state of Ti^{4+} while the different feature of oxygen K-edge is originated from the different crystal structure.[60] The strong prepeak splitting in the oxygen K-edge spectra of the HT and anatase samples is due to the Ti *3d*-O *2p* hybridization split by the local octahedral crystal field.[59, 60] The three-peak feature near 540 eV in the HT sample resembles the oxygen 2*p*- Ti *4s* and *4p* hybridization of rutile phase.[60] After proton implantation at RT, crystal-field splitting in Ti $L_{2,3}$ edge is indistinct, which reflects the presence of amorphous phase.[61]

Figure 3.6 compares the charge/discharge profiles of the irradiated and control TiO_2 samples cycled between 0.9 and 2.5 V (vs Li/Li^+) at a low current rate. Lithium insertion in electrode materials can proceed via a two-phase structural transition or single-phase solid solution charge storage behavior. The voltage profile (Figure 3.6) accounts for the structural behavior during lithium insertion/extraction. Anatase TiO_2 exhibits a two-phase region which occurs at the characteristic plateau of approximately 1.7 V vs Li/Li^+ , indicating the coexistence of a Li-poor phase $Li_{0.05}TiO_2$, which maintains the original anatase structure (space group:$I4_1/amd$) and a Li-rich phase $Li_{0.5}TiO_2$ (space group: *Imma*).[62]

After irradiation, both the HT and RT samples display sloping curves, indicating single-phase solid solution behavior. The RT sample consists of a mixture of anatase, rutile, and amorphous regions, which could impede the diffusion of Li ions. This may

explain why it has the lowest capacity (~130 mAh g^{-1}) among the three samples. The HT sample displays the highest capacity (~240 mAh g^{-1}) of the three, suggesting enhanced lithium charge storage of the disordered rutile nanotubes after irradiation at 250˚C (Figure 3.7). The capacities of all three samples are quite reversible after 20 cycles at low current rate. It was noticed that the Coulombic efficiency of both irradiated samples at the initial cycle is much lower (~ 40 -42%) than that of the non-irradiated anatase sample (~ 78%). The low Coulombic efficiency could be ascribed to the defects induced by proton irradiation, which are highly reactive with the electrolyte and could lead to more side reactions.

The rate capability study (Figure 3.8) confirms the superior diffusion of Li ions in the HT sample compared to both the RT sample and the non-irradiated anatase samples. This is especially apparently at the highest rate, where the HT irradiated sample exhibits a reversible capacity of 130 mAh/g when cycled at 2 A/g, whereas the anatase sample has a capacity of approximately 85 mAh/g when cycled at 1 A/g. The RT sample also exhibits lower performance of only 20 mAh/g but at a higher current density of 4 A/g. From the GITT analysis (Supporting Information Figure S3.2), the HT irradiated TiO_2 exhibits a range of Li^+ diffusivity of ~$1x10^{-13}$ to ~$2x10^{-14}$ cm^2 s^{-1} during Li insertion from 2 – 1V, whereas the RT irradiated TiO_2 exhibits an inferior Li^+ diffusivity of ~$3x10^{-14}$ to $4x10^{-15}$ cm^2 s^{-1} in the same range.

This result corroborates well with results from the rate capability study. In addition, the Li^+ diffusivity of the disordered rutile HT sample is between that of the Li diffusion along the *c*-axis (10^{-6} cm^2 s^{-1}) and that of the *ab*-plane (10^{-15} cm^2 s^{-1})[2, 63],

suggesting the unique disordered rutile structure of the HT sample may unblock Li^+ diffusion pathways which were previously restricted by the rigid crystalline structure.

Lithium storage mechanism was investigated by sweep cyclic voltammetry (Figure 3.9 and supporting information S3). A pair of redox peaks (Figure 3.9b) at ~1.7 V in cathodic scan and 2.15 V in anodic scan was observed in non-irradiated anatase TiO_2-NT sample, which is consistent with previous works.[64] However, the peaks become broader and indistinct in the voltammograms of both irradiated samples. Furthermore, the capacitive and diffusion contributions to electrochemical charge storage in TiO_2 of each sample were analyzed with varying scan rates according to[65]:

$$i = av^b \tag{1}$$

where the measured current i obeys a power law relationship with scan rate v. Both a and b are adjustable parameters. The b value can be determined from plotting log(i) versus log(v). A b value of 0.5 indicates that a process is limited by diffusion according to the following equation[66]:

$$i = nFAC^* D^{1/2} v^{1/2} \left(\frac{\alpha nF}{RT}\right)^{1/2} \pi^{1/2} \chi(bt) \tag{2}$$

where n is number of electrons involved in the electrode reaction, F is faraday constant, A is the surface area of the electrode material, C^* is the surface concentration, D is the diffusion coefficient, R is the gas constant, α is the transfer coefficient, T is the temperature, and $\chi(bt)$ is the normalized current for a totally irreversible system in cyclic voltammetry. A current response following eq 2 is indicative of a diffusion-controlled faradaic intercalation process[64, 67]. On the other hand, a b =1 suggests that the charge storage is dominated by a capacitive

process where the current is correlated to the capacitance by the following equation[65]:

$$i_c = \nu C_d A \quad (3)$$

where C_d is the capacitance. For non-irradiated anatase TiO_2-NT electrode, at the peak potential of 1.7 V the *b*-value is 0.55, which indicates the process is primarily the diffusion-limited intercalation reaction and is consistent with previous work[64]. At potentials higher or lower than the peak potential, the *b*-values are in the range of 0.7 - 0.9, indicating that the capacitive process becomes dominant. For the irradiated HT TiO_2-NT electrode, the *b*-values are fairly constant at around 0.7, which suggests that the lithium charge storage is controlled by both diffusion and capacitive processes. The *b*-values of irradiated RT TiO_2-NT electrode are lower than those of the HT sample and are centered on 0.6, which indicate that the charge storage in RT electrode is dominated by diffusion-limited intercalation. The mixed amorphous and crystalline domains in this material hinder the lithium diffusion, which explains the inferior rate capability of the electrode.

The capacitive contribution in the electrode can be estimated through the following analysis[64]:

$$i(V) = k_1 v + k_2 v^{1/2} \quad (4)$$

where the current response *i(V)* is a combination of capacitor-like and diffusion controlled behaviors[64]. $k_1 v$ and $k_2 v^{1/2}$ correspond to the capacitive and diffusion-controlled contribution[64], respectively. By determine the k_1 and k_2 through linear fitting of $i(V)/ v^{1/2}$ versus $v^{1/2}$ as a function of potential, it is possible to calculate the contributions from diffusion-controlled intercalation and capacitor-like processes. The

capacitive contribution for non-irradiated anatase, HT proton irradiated, and RT proton irradiated nanotubes were 33%, 27% and 17% of the total capacity, respectively. The results suggest that after irradiation there is more contribution from diffusion-limited intercalation to the lithium charge storage and there is a wide site energy distribution caused by the defects induced through proton irradiation, which corresponds to the sloping characteristics of the voltage profiles of irradiated samples.

3.5 Conclusions

In this study, the effect of irradiation on amorphous TiO_2 nanotube substrates was observed. It was found that while structural integrity is maintained, phase transformations occur upon proton irradiation at both room temperature and high temperature. Results from Raman spectroscopy and TEM indicate that under room temperature proton irradiation, short-range-ordered crystallites are formed and the final structure is a mixture of anatase, amorphous and rutile domains. Under high temperature proton implantation, a phase transformation occurs resulting in a primarily disordered rutile phase. Both high temperature and room temperature irradiated samples exhibits single-phase solid solution lithium intercalation. The room temperature irradiated sample has a reduced capacity possibly due to the combination of anatase, rutile and amorphous phases present resulting in reduced ion mobility. On the other hand, high temperature irradiation results in improved capacity, likely due to the disordered rutile structure. GITT results suggest that Li^+ diffusivity in the high temperature irradiated sample is higher than that of the room temperature irradiated sample, which is further confirmed by the enhanced rate capability of the high temperature sample. Analysis on capacitive and diffusion contribution in

lithium charge storage of irradiated TiO_2-NT suggests that there is more contribution from diffusion-limited intercalation after irradiation.

3.6 Figures and Tables

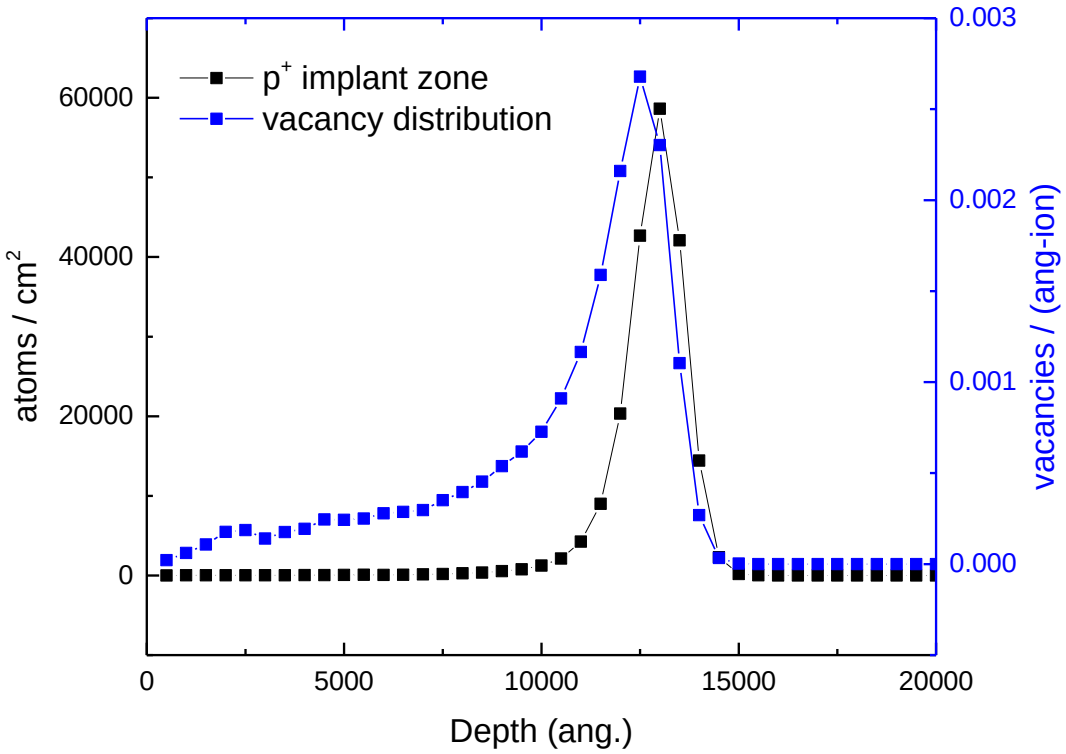

Figure 3.1. Depth distribution calculation of implanted ions (H^+ ions) and resulting damage profile (Ti-, O- recoil) for anatase TiO_2. (*J. Mat. Chem. A.* 5 11815-11824, 2017)

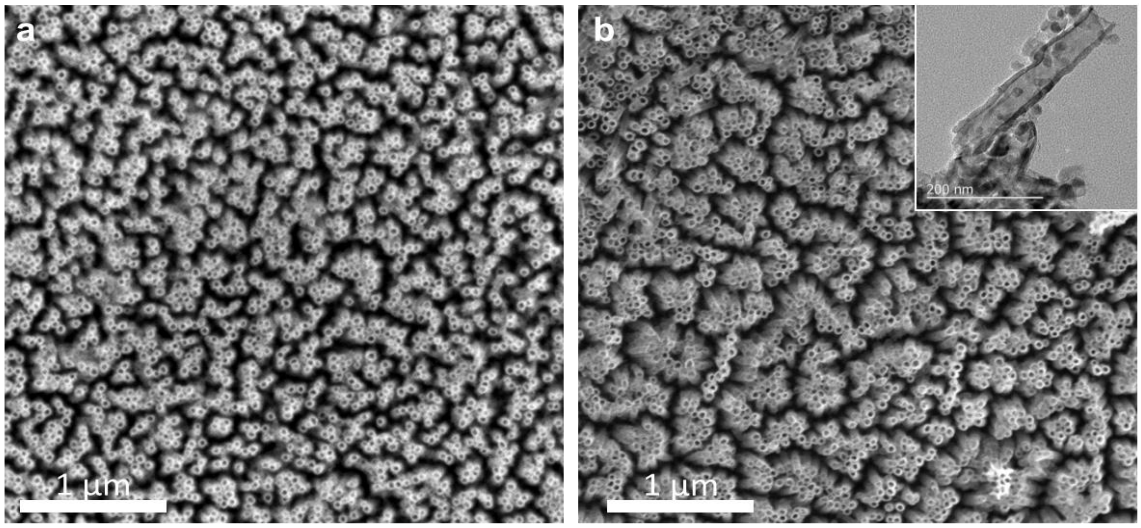

Figure 3.2. (a) SEM top view of TiO_2-NT film before irradiation and (b) after irradiation (inset: TEM image of tube after irradiation). (*J. Mat. Chem. A.* 5 11815-11824, 2017)

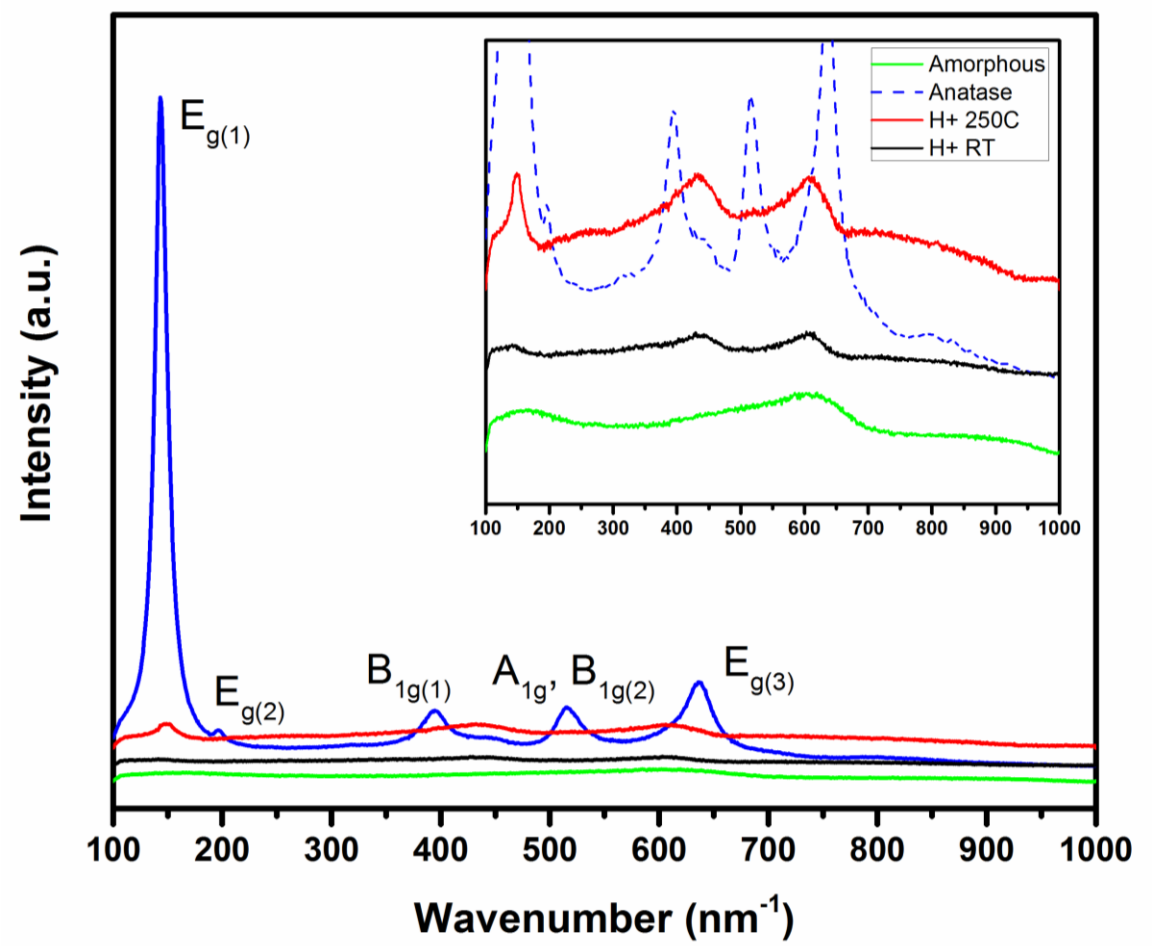

Figure 3.3. Raman spectra of non-irradiated anatase TiO_2 nanotubes (blue), non-irradiated amorphous (green), HT-TiO_2 proton irradiated nanotubes (red), and RT-TiO_2 proton irradiated nanotubes (black). Inset is the zoomed in view. (*J. Mat. Chem. A.* 5 11815-11824, 2017)

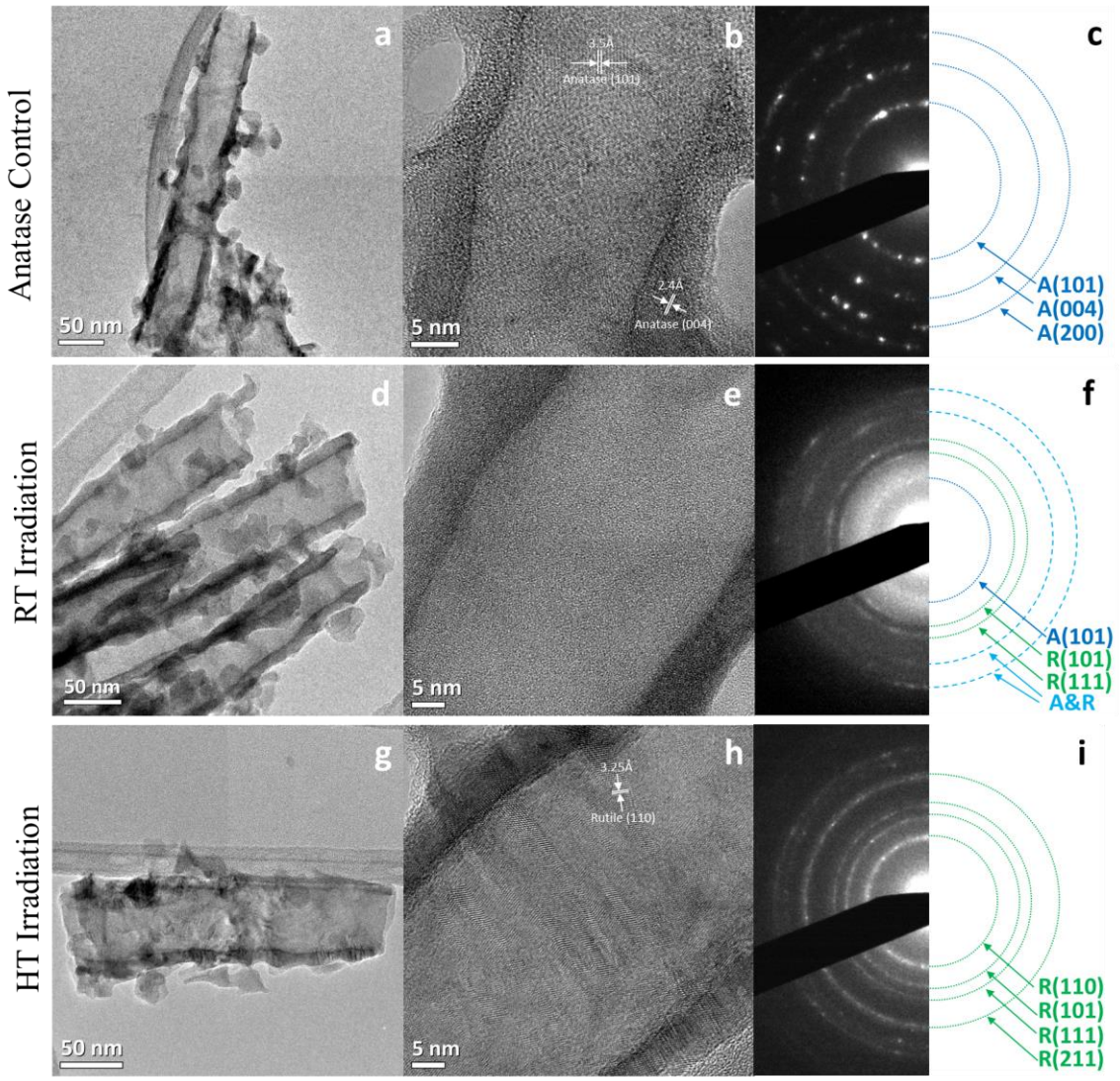

Figure 3.4. Low magnification TEM (4a, 4d, 4g) of non-irradiated anatase TiO_2 nanotubes, RT proton irradiated nanotubes, and HT irradiated nanotubes, respectively, showing retained structural morphology after irradiation. HRTEM of the non-irradiated anatase TiO_2 nanotubes, RT proton irradiated nanotubes, and HT irradiated nanotubes (4b, 4e, 4h, respectively), and their corresponding SAED (4c, 4f, 4i, respectively). (*J. Mat. Chem. A.* 5 11815-11824, 2017)

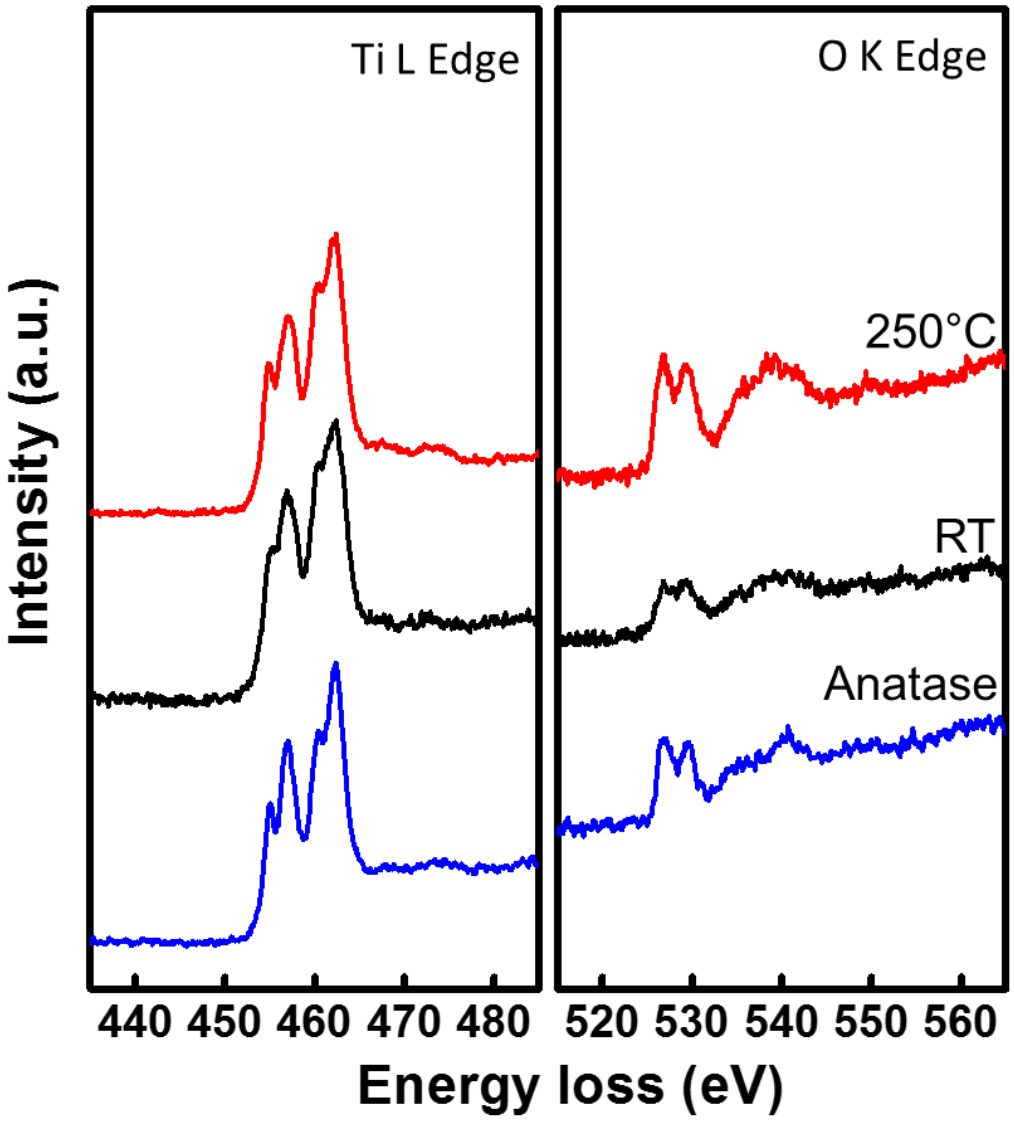

Figure 3.5. Electronic energy loss spectra (EELS) of the non-irradiated anatase TiO2, RT proton irradiated TiO2 and HT proton irradiated TiO2 nanotube samples. (J. Mat. Chem. A. 5 11815-11824, 2017)

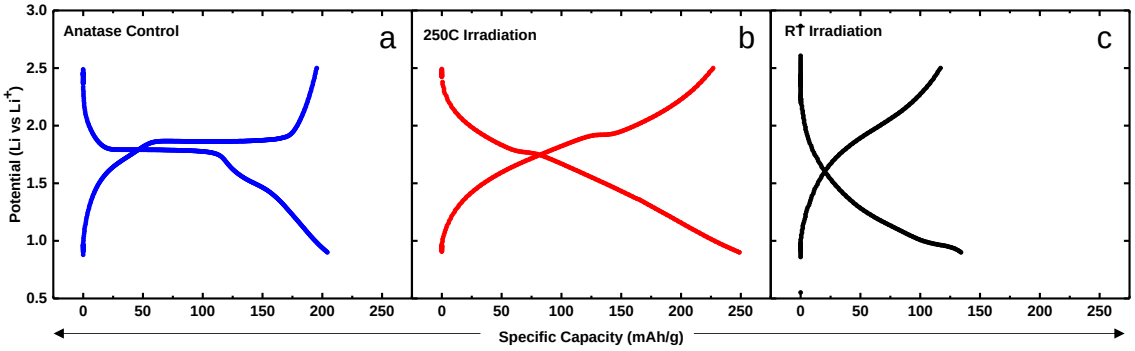

Figure 3.6. Charge/discharge curves of the non-irradiated anatase nanotube anode (a), the HT proton irradiated TiO_2 nanotubes (b), and the RT proton irradiated TiO_2 nanotubes (c). (*J. Mat. Chem. A.* 5 11815-11824, 2017)

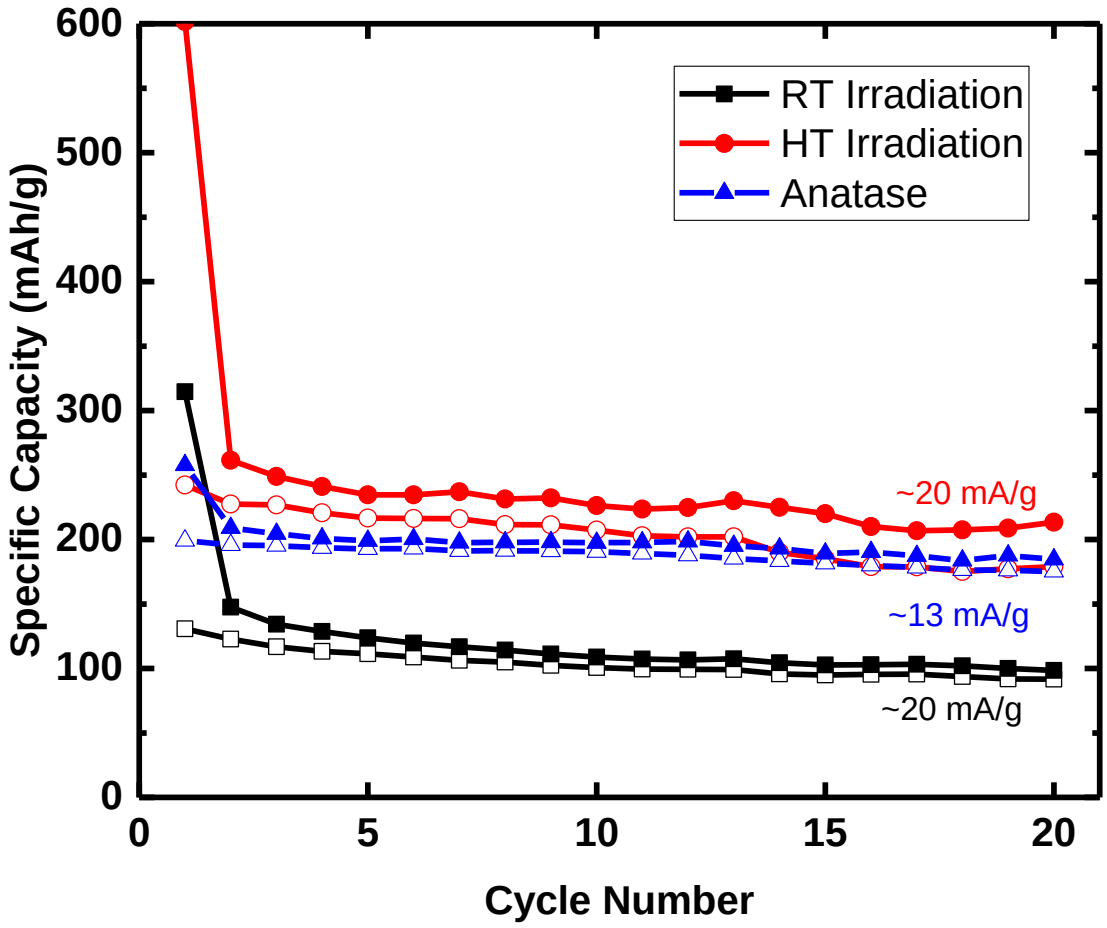

Figure 3.7. Low rate galvanostatic cycling of non-irradiated anatase nanotubes (blue), RT proton irradiated nanotubes (*J. Mat. Chem. A.* 5 11815-11824, 2017)

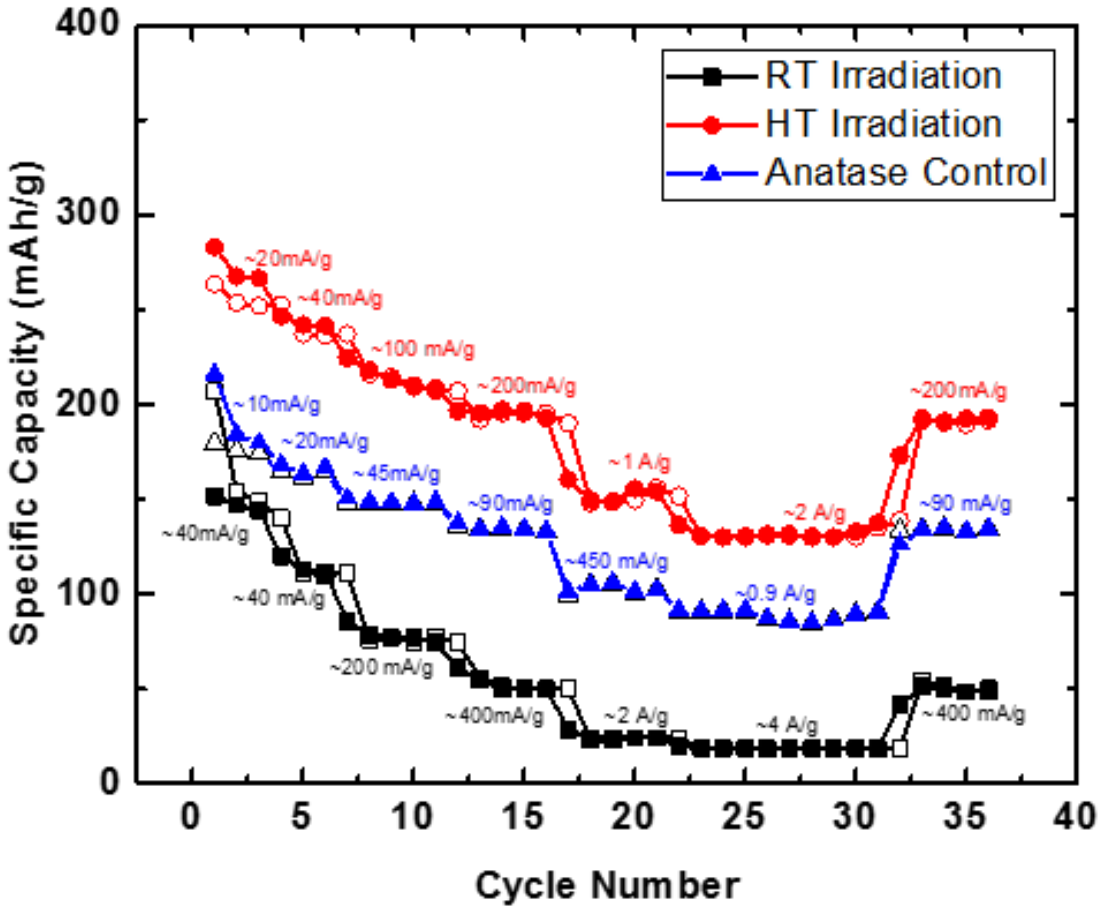

Figure 3.8. Galvanostatic rate study of non-irradiated anatase nanotubes (blue), RT proton irradiated nanotubes (black), and HT proton irradiated nanotubes (red) between 0.9 and 2.5V vs Li/Li$^+$. (*J. Mat. Chem. A.* 5 11815-11824, 2017)

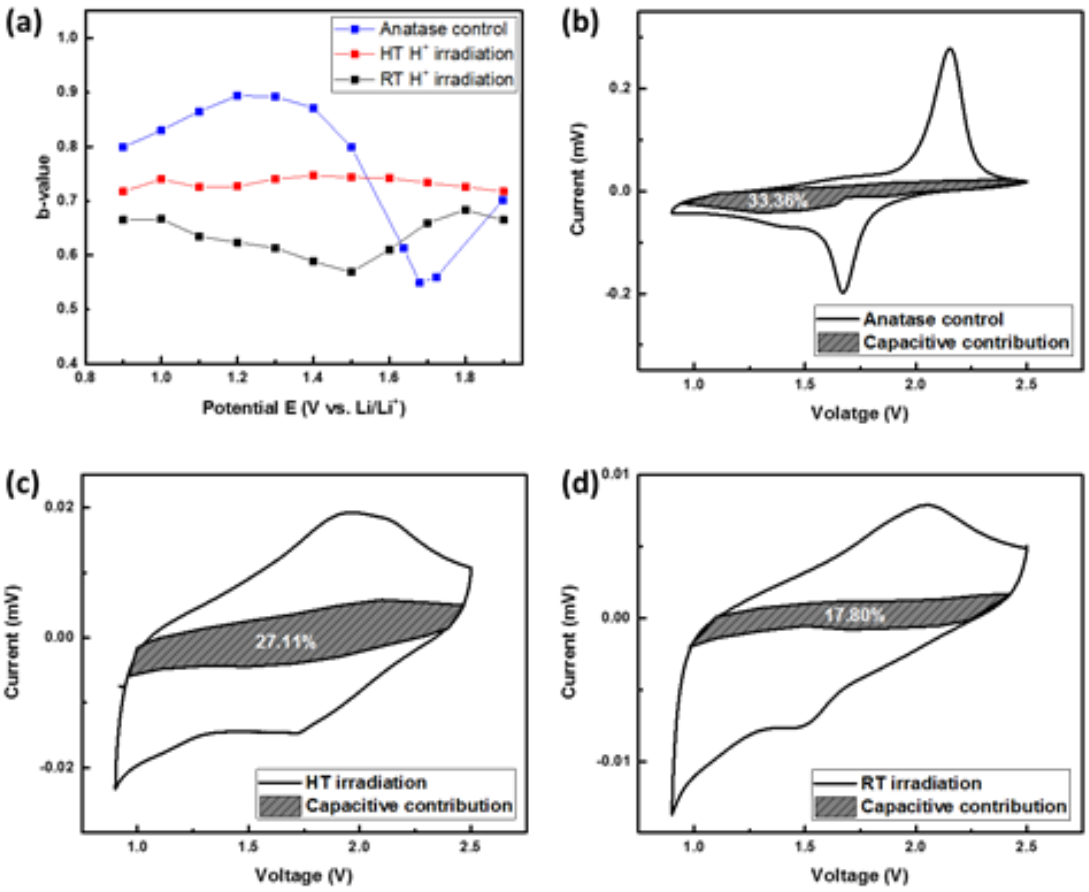

Figure 3.9. (a) *b*-values and voltammetric response (0.5 mV/s) for (b) non-irradiated anatase TiO2-NT , (c) HT proton irradiated TiO2-NT and (d) RT proton irradiated TiO2-NT. The capacitive currents (shaded region) are determined from the data in Supporting Information Figure S3.3. (J. Mat. Chem. A. 5 11815-11824, 2017)

3.7 References

1. D. Deng, M. G. Kim, J. Y. Lee and J. Cho, *Energ Environ Sci*, 2009, **2**, 818-837.

2. Z. G. Yang, D. Choi, S. Kerisit, K. M. Rosso, D. H. Wang, J. Zhang, G. Graff and J. Liu, *J Power Sources*, 2009, **192**, 588-598.

3. G. N. Zhu, Y. G. Wang and Y. Y. Xia, *Energ Environ Sci*, 2012, **5**, 6652-6667.

4. C. D. Joyce, T. McIntyre, S. Simmons, H. LaDuca, J. G. Breitzer, C. M. Lopez, A. N. Jansen and J. T. Vaughey, *J Power Sources*, 2010, **195**, 2064-2068.

5. B. Zachauchristiansen, K. West, T. Jacobsen and S. Atlung, *Solid State Ionics*, 1988, **28**, 1176-1182.

6. P. G. Bruce, B. Scrosati and J. M. Tarascon, *Angewandte Chemie, International Edition*, 2008, **47**, 2930-2946.

7. A. S. Arico, P. Bruce, B. Scrosati, J. M. Tarascon and W. Van Schalkwijk, *Nature Materials*, 2005, **4**, 366-377.

8. M. Wagemaker, W. J. H. Borghols and F. M. Mulder, *J. Amer. Chem. Soc.*, 2007, **129**, 4323-4327.

9. L. Kavan, M. Kalbac, M. Zukalova, I. Exnar, V. Lorenzen, R. Nesper and M. Graetzel, *Chem. Mater.*, 2004, **16**, 477-485.

10. J. Maier, *J Power Sources*, 2007, **174**, 569-574.

11. Y. Wang and G. Z. Cao, *Adv Mater*, 2008, **20**, 2251-2269.

12. A. Manthiram, A. V. Murugan, A. Sarkar and T. Muraliganth, *Energ Environ Sci*, 2008, **1**, 621-638.

13. J. S. Chen, Y. L. Tan, C. M. Li, Y. L. Cheah, D. Luan, S. Madhavi, F. Y. C. Boey, L. A. Archer and X. W. Lou, *J. Amer. Chem. Soc.*, 2010, **132**, 6124-6130.

14. Y. S. Hu, L. Kienle, Y. G. Guo and J. Maier, *Advanced Materials*, 2006, **18**, 1421-+.

15. E. Baudrin, S. Cassaignon, M. Koesch, J. P. Jolivet, L. Dupont and J. M. Tarascon, *Electrochem Commun*, 2007, **9**, 337-342.

16. D. H. Wang, D. W. Choi, Z. G. Yang, V. V. Viswanathan, Z. M. Nie, C. M. Wang, Y. J. Song, J. G. Zhang and J. Liu, *Chem Mater*, 2008, **20**, 3435-3442.

17. B. P. Hahn, J. W. Long and D. R. Rolison, *Accounts Chem Res*, 2013, **46**, 1181-1191.

18. B. Koo, H. Xiong, M. D. Slater, V. B. Prakapenka, M. Baasubramanian, P. Podsiadlo, C. S. Johnson, T. Rajh and E. V. Shevchenko, *Nano Letters*, 2012, **12**, 2429-2435.

19. B. Koo, S. Chattopadhyay, T. Shibata, V. B. Prakapenka, C. S. Johnson, T. Rajh and E. V. Shevchenko, *Chem Mater*, 2013, **25**, 245-252.

20. J. Lee, A. Urban, X. Li, D. Su, G. Hautier and G. Ceder, *Science*, 2014, **343**, 519-522.

21. M. M. Thackeray, S. H. Kang, C. S. Johnson, J. T. Vaughey, R. Benedek and S. A. Hackney, *J Mater Chem*, 2007, **17**, 3112-3125.

22. T. Ohzuku, M. Nagayama, K. Tsuji and K. Ariyoshi, *J Mater Chem*, 2011, **21**, 10179-10188.

23. D. Qian, B. Xu, M. Chi and Y. S. Meng, *Phys Chem Chem Phys*, 2014, **16**, 14665-14668.

24. H. Xiong, H. Yildirim, E. V. Shevchenko, V. B. Prakapenka, B. Koo, M. D. Slater, M. Balasubramanian, S. K. R. S. Sankaranarayanan, J. P. Greeley, S. Tepavcevic, N. M. Dimitrijevic, P. Podsiadlo, C. S. Johnson and T. Rajh, *J Phys Chem C*, 2012, **116**, 3181-3187.

25. H. Xiong, H. Yildirim, P. Podsiadlo, J. Zhang, V. B. Prakapenka, J. P. Greeley, E. V. Shevchenko, K. K. Zhuravlev, S. Tkachev, S. K. R. S. Sankaranarayanan and T. Rajh, *Phys Rev Lett*, 2013, **110**.

26. D. R. Rolison and L. F. Nazar, *Mrs Bull*, 2011, **36**, 486-493.

27. H. A. Shukur, M. Sato, I. Nakamura and I. Takano, *Adv Mater Sci Eng*, 2012, 1-7.

28. L. Z. Qin, B. Liao, X. L. Dong, X. Y. Wu, X. G. Hou and A. D. Liu, *Nucl Instrum Meth B*, 2009, **267**, 1077-1080.

29. N. Matsunami, M. Uebayashi, K. Hirooka, T. Shimura and M. Tazawa, *Nucl Instrum Meth B*, 2009, **267**, 1654-1657.

30. R. Fromknecht, I. Khubeis, S. Massing and O. Meyer, *Nucl Instrum Meth B*, 1999, **147**, 191-201.

31. O. Meyer, I. Khubeis, R. Fromknecht and S. Massing, *Nucl Instrum Meth B*, 1998, **136**, 436-441.

32. O. Meyer, I. Khubeis, R. Fromknecht and S. Massing, *Nucl Instrum Meth B*, 1997, **127**, 624-628.

33. S. K. Zheng, T. M. Wang, C. Wang and G. Xiang, *Nucl Instrum Meth B*, 2002, **187**, 479-484.

34. S. K. Zheng, T. M. Wang, W. C. Hao and R. Shen, *Vacuum*, 2002, **65**, 155-159.

35. D. Su, F. Wang, C. Ma and N. Jiang, *Nano Energy*, 2013, **2**, 343-350.

36. G. s. Was, *Fundamentals of Radiation Materials Science: Metals and Alloys*, Springer, 2007.

37. B. P. Uberuaga and X. M. Bai, *J Phys-Condens Mat*, 2011, **23**.

38. X. M. Bai and B. P. Uberuaga, *Jom-Us*, 2013, **65**, 360-373.

39. T. Hartmann, L. M. Wang, W. J. Weber, N. Yu, K. E. Sickafus, J. N. Mitchell, C. J. Wetteland, M. A. Nastasi, M. G. Hollander, N. P. Baker, C. R. Evans, J. R. Tesmer and C. J. Maggiore, *Nucl Instrum Meth B*, 1998, **141**, 398-403.

40. N. Liu, V. Haublein, X. M. Zhou, U. Venkatesan, M. Hartmann, M. Mackovic, T. Nakajima, E. Spiecker, A. Osvet, L. Frey and P. Schmuki, *Nano Lett*, 2015, **15**, 6815-6820.

41. J. M. Macak, H. Tsuchiya, A. Ghicov, K. Yasuda, R. Hahn, S. Bauer and P. Schmuki, *Curr Opin Solid St M*, 2007, **11**, 3-18.

42. J. F. Ziegler, Biersack, J. P., Littmark, U., *Pergamon Press: New York*, 1985.

43. E. Silva, F. A. La Porta, M. S. Liu, J. Andres, J. A. Varela and E. Longo, *Dalton T*, 2015, **44**, 3159-3175.

44. P. Tengvall, T. P. Vikinge, I. Lundstrom and B. Liedberg, *J Colloid Interf Sci*, 1993, **160**, 10-15.

45. S. Sahoo, A. K. Arora and V. Sridharan, *J Phys Chem C*, 2009, **113**, 16927-16933.

46. Y. Lei, L. D. Zhang and J. C. Fan, *Chem Phys Lett*, 2001, **338**, 231-236.

47. W. B. Hu, L. P. Li, G. S. Li, C. L. Tang and L. Sun, *Cryst Growth Des*, 2009, **9**, 3676-3682.

48. V. Swamy, B. C. Muddle and Q. Dai, *Appl Phys Lett*, 2006, **89**.

49. V. Swamy, A. Kuznetsov, L. S. Dubrovinsky, R. A. Caruso, D. G. Shchukin and B. C. Muddle, *Phys Rev B*, 2005, **71**.

50. S. P. S. Porto, P. A. Fleury and T. C. Damen, *Phys Rev*, 1967, **154**, 522-&.

51. V. Swamy, D. Menzies, B. C. Muddle, A. Kuznetsov, L. S. Dubrovinsky, Q. Dai and V. Dmitriev, *Appl Phys Lett*, 2006, **88**.

52. K. K. Tiong, P. M. Amirtharaj, F. H. Pollak and D. E. Aspnes, *Appl Phys Lett*, 1984, **44**, 122-124.

53. H. Heusler, J. Epping, S. Heusler, E. Richter, N. P. E. Vermeulen and D. D. Breimer, *J Chromatogr*, 1981, **226**, 403-412.

54. J. M. Zhang, M. Lang, R. C. Ewing, R. Devanathan, W. J. Weber and M. Toulemonde, *J Mater Res*, 2010, **25**, 1344-1351.

55. M. Toulemonde, W. J. Weber, G. S. Li, V. Shutthanandan, P. Kluth, T. F. Yang, Y. G. Wang and Y. W. Zhang, *Phys Rev B*, 2011, **83**.

56. M. Toulemonde, J. M. Constantini, C. Dufour, A. Meftah, E. Paumier and F. Studer, *Nucl Instrum Meth B*, 1996, **116**, 37-42.

57. J. M. Costantini, F. Brisard, M. Toulemonde and F. Studer, *Nucl Instrum Meth B*, 1997, **122**, 514-521.

58. A. Tighineanu, Friedrich-Alexander Universität Erlangen-Nürnberg, 2014, p. 183.

59. A. Gloter, C. Ewels, P. Umek, D. Arcon and C. Colliex, *Phys Rev B*, 2009, **80**.

60. Z. Y. Wu, G. Ouvrard, P. Gressier and C. R. Natoli, *Phys Rev B*, 1997, **55**, 10382-10391.

61. G. Bertoni, E. Beyers, J. Verbeeck, M. Mertens, P. Cool, E. F. Vansant and G. Van Tendeloo, *Ultramicroscopy*, 2006, **106**, 630-635.

62. M. Wagemaker, G. J. Kearley, A. A. van Well, H. Mutka and F. M. Mulder, *J Am Chem Soc*, 2003, **125**, 840-848.

63. M. V. Koudriachova, N. M. Harrison and S. W. de Leeuw, *Phys Rev Lett*, 2001, **86**, 1275-1278.

64. J. Wang, J. Polleux, J. Lim and B. Dunn, *J Phys Chem C*, 2007, **111**, 14925-14931.

65. H. Lindstrom, S. Sodergren, A. Solbrand, H. Rensmo, J. Hjelm, A. Hagfeldt and S. E. Lindquist, *J Phys Chem B*, 1997, **101**, 7717-7722.

66. A. J. Bard and L. R. Faulkner, *Electrochemical Methods: Fundamentals and Applications*, John Weiley & Sons, New York, 1980.

67. V. Augustyn, P. Simon and B. Dunn, *Energ Environ Sci*, 2014, **7**, 1597-1614.

68. H. Xiong, M. D. Slater, M. Balasubramanian, C. S. Johnson and T. Rajh, *J Phys Chem Lett*, 2011, **2**, 2560-2565

3.8 Supporting Information

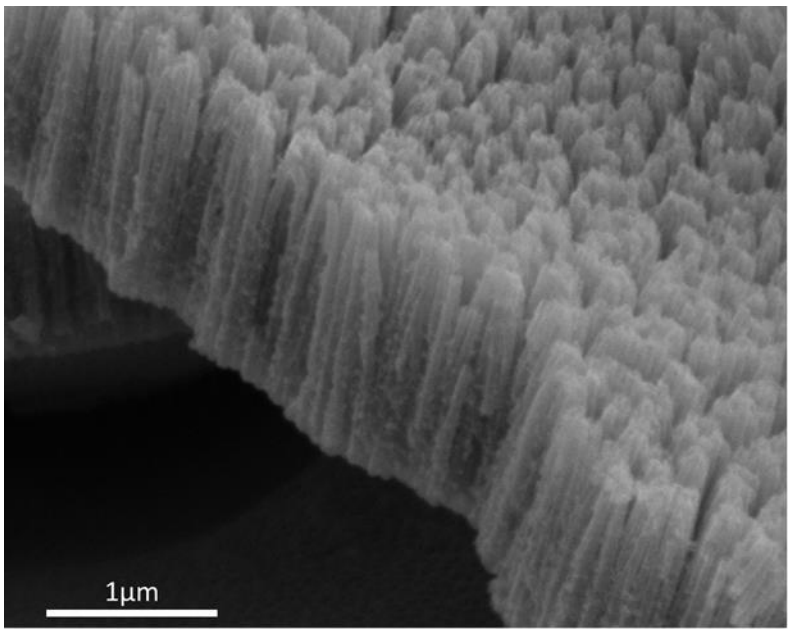

Figure S3.1: SEM cross-section view of TiO_2-NT film before irradiation. The nanotubes are ~1µm tall.

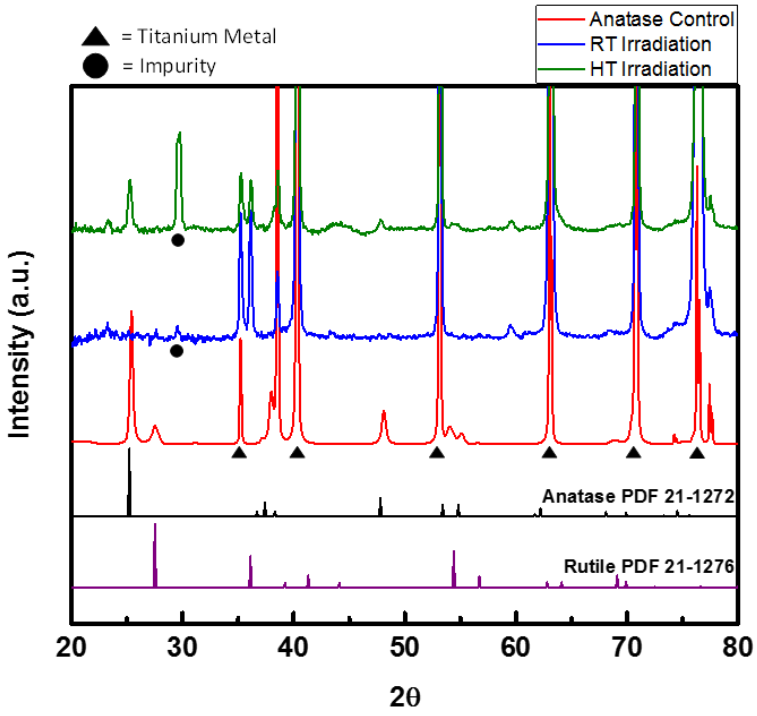

Figure S3.2: X-ray diffraction spectra (XRD) of TiO_2 nanotubes before and after proton irradiation.

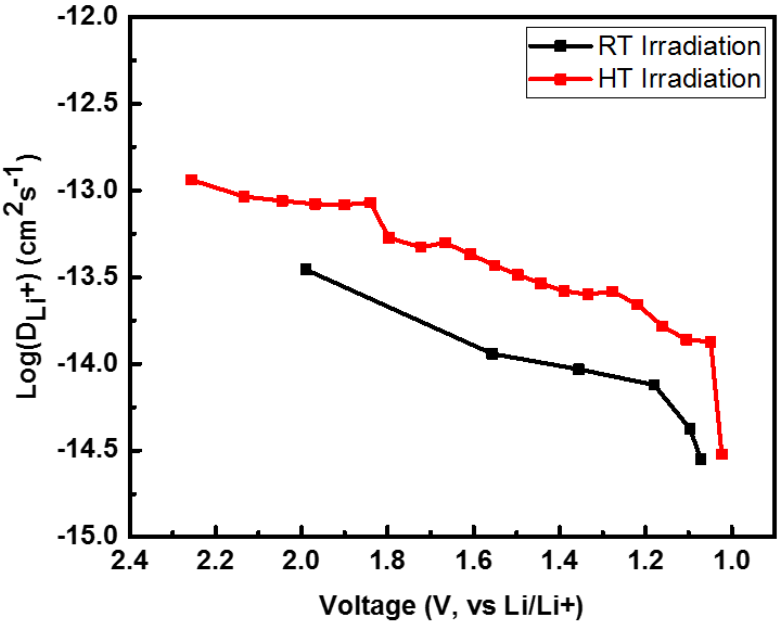

Figure S3.3: Diffusion coefficients for room temperature and high temperature proton irradiated TiO_2 nanotubes as calculated by GITT.

CHAPTER FOUR: Proton Irradiation on Crystalline Titania Lithium Ion Battery Electrodes

This chapter is in preparation for publication.

PROTON IRRADIATION ON CRYSTALLINE TITANIA LITHIUM ION BATTERY ELECTRODES

Kassiopeia A. Smith[a]

Andreas I. Savva[a]

Yongqiang Wang[b]

Khalid Hattar[c]

Darryl P. Butt[d]

Janelle P. Wharry[e]

Hui Xiong[a]

[a]*Micron School of Materials Science and Engineering, Boise State University, Boise ID 83725*

[b]*Ion Beam Materials Laboratory, Los Alamos National Laboratory, Los Alamos, NM*

[c]*Ion Beam Laboratory, Sandia National Laboratory, Albuquerque, NM 87123*

[df]*College of Mines and Earth Sciences, University of Utah, Salt Lake City, Utah*

[e]*School of Nuclear Engineering, Purdue University, West Lafayette, IN 47907*

4.1 Introduction

Rechargeable lithium ion batteries (LIBs) were revolutionary in the development of a myriad of portable electronics, and are currently considered the most promising energy storage devices for a wide range of next generation technologies.[1] Titanium oxide anodes have attracted great attention over the years due to their inherent safety, stability, and cost, as well as their relatively low lithium intercalation potential of approximately 1.5-1.8 V vs Li/Li^+.[2-4] The TiO_2 polymorphs, in particular, have gained increasing interest due to their theoretical capacity of 335 mAh/g (or 1.0 Li per TiO_2), which is comparable to commercial graphite electrodes (372 mAh/g).[4] Anatase is tetragonal body-centered with the space group $I4_1/amd$, and is made up of edge-sharing TiO_6 octahedra.[5] This structure can be visualized as stacking 1D zigzag chains of edge sharing octahedra, resulting in zigzag channels within the framework.[2] The facile diffusion of lithium ions occurs along these channels into the interstitial sites resulting in a transformation to the orthorhombic structure.[3]

The original attempts at using anatase as an anode focused on microcrystalline morphologies which exhibited only moderate specific capacities with a maximum uptake of 0.5 Li per TiO_2 due to limited room temperature conductivity.[6] These limitations spurred development of nanoscale TiO_2 materials, which led to significant improvement in reported electrochemical properties.[1, 7-13] The shift towards size reduction to the nano-scale allows for increased contact area between the electrode and electrolyte, and reduced Li^+ transport distances allowing for higher power applications.[7, 10, 14] The reaction of lithium with TiO_2 can be expressed as: $xLi^+ + TiO_2 + xe^- \leftrightarrow Li_xTiO_2$. When lithium is inserted into the host structure, the charge is distributed between the Ti and O ions which

leads to structural deformation. Interstitial sites or vacancies present in the structure play an important role in the atomic rearrangement of the material, and allow for improved storage capacity.[15] Recent works have suggested that the introduction of intentional structural defects may enhance the electrochemical charge storage properties of transition metal oxide electrodes.[15-18] One such method is to use ion irradiation to generate a significant number of defects within the target material.

It has been widely recognized that ion irradiation promotes the formation of defects within a crystalline solids.[19] As the irradiating particle slows down within the material, it collides with lattice atoms of the solid. Some of these knock-on events transfer enough energy to displace atoms from their original position, which has the potential to displace more and more atoms, resulting in a damage cascade.[20] Eventually the volume immediately surrounding the ion track becomes populated with vacancies, interstitials, and other defects. As the fluence of the irradiating species increases, the damage cascades overlap resulting in the overall disordering of the material. Over time, this irradiation damage maybe annealed out of the substrate, which is known as a self-healing, and significantly reduced the retention of defects formed during the damage cascade.[20]

In recent years, several studies have brought attention to the effect of irradiation on TiO_2. Density functional theory simulations on this topic have suggested that rutile may have better resistance to amorphization than anatase TiO_2 polymorphs due to atomic packing densities.[21-23] This was supported by the works from Uberuagua, Qin, and Lumpkin, with studies which further elucidated on the mechanisms of defect accumulation and amorphization resistance.[22, 24, 25] In addition to polymorph behavior,

Li et al. studied the effect of temperature dependence, showing that higher temperatures allow for point defect mobility and increased instances of damage recovery, whereas at room temperature irradiation produces more stable point defects.[26] Hartmann et al. later suggested that using lighter irradiation species, such as He^{+}, is more likely to amorphize target substrates than heavy noble gases such as Xe^{2+} and Ne^{+}.[27] Schmuki et al. recently studied the effect of proton irradiation on anatase TiO_2 films for photocatalytic evolution, and showed that proton implantation induced specific defects which created co-catalytic centers and enhanced photocatalytic activity.[28] Finally, in our previous study, it was shown that when irradiated with protons at 250 ˚C, amorphous TiO_2 undergoes a phase transformation to disordered rutile leading to an increase in capacity and rate capabilities.[15]

In this study, we investigate the effect of proton irradiation both at room temperature and at elevated temperature on anataseTiO_2 nanotube (TiO_2-NT) electrodes. Implantations were carried out at an energy of 190 keV with an average dose of 0.17 displacements per atom (dpa). Structural characterizations by Raman spectroscopy, and X-ray diffraction suggest that no major change in microstructure occurs, however, the enhanced electrochemical performance suggests defect formation. Electrochemical impedance spectroscopy (EIS) was conducted and it was found that both irradiated samples exhibit reduced charge transfer resistance, and increase lithium diffusivity. Furthermore, both the sample irradiated at 250 ˚C and 25 ˚C demonstrates improved capacity at low rate and superior rate capability compared to the non-irradiated anatase TiO_2-NT.

4.2 Experimental

4.2.1 Materials

TiO_2 nanotubes were synthesized by electrochemical anodization described previously.[29, 30] To summarize, pure titanium foil (0.0127mm, 99.8%, Alfa Aesar) was electropolished[31], followed by a three step sonication in acetone, isopropyl alcohol and D.I. water. The back of the Ti foil was protected by tape to ensure uniform current distribution. The anodization was carried out in a two-electrode cell with Pt mesh as the counter electrode. The anodization was carried out for 10 minutes under a constant voltage of 15 V in an electrolyte of 0.36 M ammonium fluoride (Aldrich) in 95 vol % formamide (Fisher) and 5 vol % DI water. The anodized samples were then ultrasonically cleaned in DI water for 30 seconds. Anatase TiO_2 was made by annealing the as-prepared TiO_2 NTs in a mixture of ultra-pure 20% O_2/balance Ar gas at 450°C for 4 hours.

4.2.2 Irradiation

The TiO_2-NT films were irradiated with 195 keV protons in a 200 kV Varian ion implanter at Los Alamos National Laboratory. The accelerator beam line was maintained at 4×10^{-7} torr throughout the experiment. Specimens were mounted onto a copper irradiation stage, which was electrically isolated from the accelerator beam line, to allow for accurate charge collection. Thermocouples were mounted onto the copper stage and used to control the temperatures throughout the implantation.

The damage depth profile and displacement damage were calculated using the Stopping and Range of Ions in Matter (SRIM-2013) program using the “Quick Calculation” mode and the displacements were obtained from the resulting vacancy.txt file. One downside of this software is the inability to model precise nano-structures, so

for these calculations a compact layer of TiO_2 (density of 4.23 g cm^{-3}) was used. Displacement energy for titanium and oxygen were set to 25 and 28 eV respectively. The 195 keV proton flux produces a relatively uniform damage profile through ~900nm, which ensured that the length of the nanotubes would receive a consistent irradiation dose. Using the "Quick Calculation" mode the number of displacements per ion-angstrom was 3.06×10^{-3} vacancies per ang-ion at the peak implantation depth, which was converted to a fluence of 2.18×10^{17} ions cm^{-2} to reach the average accumulated proton dose of 0.17 dpa.

4.2.3 Electrochemical Testing

Li half-cells were assembled in coin-type cells (Hohsen 2032) with Li metal foil as the negative electrode, a 2325 type polymer separator, and 1.2 M $LiPF_6$ in ethylene carbonate/ethyl methyl carbonate (3:7 weight ratio) electrolyte (Tomiyama) . Half-cells were cycled galvanostatically at varying currents between 2.5 and 0.9 V vs. Li/Li^+ using an automated Maccor battery tester at ambient temperatures. Three-electrode cells were made using ECC-Ref cells (EL-Cell) with Lithium metal as both counter and reference electrode. EIS and Mott-Schottky measurements were carried out in three-electrode cells using a Bio-Logic Science Instruments potentiostat/galvanostat. Mott-Schottky analysis was performed using the SPEIS program on a Bio-Logic VMP-300 in a three-electrode cell. Samples were masked with Kapton tape with a 15 mm diameter area left exposed. A Pt mesh was used as the counter electrode in an aqueous 1 M KOH solution. A Ag/AgCl reference electrode was used. Samples were subsequently analyzed in a frequency range from 100 kHz to 100 mHz with an excitation voltage of 10 mV from 0.1 to -1 V vs. Ag/AgCl in 0.05 V increments. Electrochemical impedance spectroscopy (EIS) was done

on a Bio-Logic VMP-300 using a three-electrode cell (EL-CELL). Samples were analyzed in a frequency range from 100 kHz to 5 mHz at open circuit voltages by applying a sinusoidal voltage with an amplitude of 5 mV. The mass of the TiO_2 nanotube film was not used in this case. Electropolishing the Ti metal before anodization allows for formation of uniform, well adhered nanotubes. In this case, areal capacity was considered in order to remove the chance of error of improperly stripping the active oxide from the Ti metal substrate. Accurate area measurements of the electrodes were conducted by microscopy.

4.2.4 Electron Microscopy

Scanning electron microscopy (SEM) images were recorded with a FEI Teneo field emission microscope operating at 5 kV. Transmission electron microscopy (TEM) images, including HRTEM, and SAED, were recorded with a JEOL JEM-2100HR operating at 200 kV at Boise State University.

4.2.5 Raman Spectroscopy

Raman spectroscopy was conducted using a Horiba Scientific LabRAM HR Evolution spectrometer using the 442 nm He:Cd laser with signal accumulations of three 30s scans. After instrument calibration, samples were scanned at room temperature under ambient conditions. The incident laser power was 100 mW, and samples were viewed at a magnification of 100x. Scattered light was collected with a thermoelectrically cooled Si CCD detector. Data was acquired using the LabSpec 6 Spectroscopy Suite software, and analyzed using OriginPro software.

4.3 Results and Discussion

Electrochemical anodization was used to synthesize the vertically oriented TiO_2-NTs by a method described in detail elsewhere.[30, 31] It is beneficial to use anodization to create the electrodes in this study, as the as-prepared TiO_2-NTs are inherently connected to the Ti substrate, which acts as both a current collector and a rigid backing for handling and characterization. This type of synthesis eliminates the need for conductive carbon additives and polymer binders which are typically used in electrodes for lithium-ion batteries. After anodization, the nanotubes are annealed at 450 ˚C under an oxygen atmosphere to facilitate a phase transformation to the anatase crystal structure. Figure 4.1a is the SEM top view of the nanotubes after anodization and annealing. The as-prepared TiO_2-NT film is about 1 μm in length and has an outer diameter of about 60 nm with a 10 nm wall thickness. As reported previously, the stability of the TiO_2 substrate is maintained after irradiation (Figure 4.1b).[15]

TiO_2-NT films were ion implanted with protons (p^+) at an energy of 195 keV with a fluence of 2.18×10^{17} ions/cm^2 resulting in an average accumulated proton dose of 0.17 DPA. The implantations were carried out under either 25°C or at 250°C to study the low and high temperature effect of implantation on the crystal structure. Figure 4.2 shows the damage depth distribution for a compact layer of TiO_2 according to Monte Carlo simulations using SRIM 2013.[32] These calculations result in a maximum damage peak at a depth of 1.1 μm. This simulation was carried out based on compact TiO_2 (without compensation for nano-structure). It has been suggested by Schmuki et al. that the actual damage depth in TiO_2-NT film may be greater due to the porosity of the film.[28] The anodization parameters were tailored such that the irradiation damage would be uniform

throughout the nanotube length by ensuring that the tube length would be less than the calculated depth of the damage peak.

In order to evaluate the effect of irradiation on the microstructural evolution of the TiO_2-NT, a number of techniques were employed. Raman spectroscopy is a useful tool in determining the structure and degree of ordering of a crystalline material.[33-39] Anatase TiO_2 has six characteristic Raman active vibrational modes which are located at 144, 196, 639 cm^{-1} and are designated as $E_{g(1)}$, $E_{g(2)}$ and $E_{g(3)}$, respectively, two B_{1g} modes at 397 and 519 cm^{-1}, designated as $B_{1g(1)}$, and $B_{1g(2)}$, respectively, and an A_{1g} mode at 513 cm^{-1}. The comparison of both the high temperature and room temperature irradiated samples to the non-irradiated control sample is shown in Figure 4.3. After irradiation, there is no significant change to the shape or location of the peaks, indicating the that the overall atomic structure has been maintained. There is a slight reduction in intensity of the peaks in the samples after irradiation, indicating that the vibrational modes have been weakened likely due to the introduction of disorder into the lattice.

Each of the irradiated samples, as well as the anatase control and the pure Ti foil was subsequently characterized by XRD (Figure 4.4). As expected, strong Ti peaks are present in all of the spectra due to diffraction from the substrate. Additionally, during annealing a fraction of the oxide is transformed to the rutile phase, which mainly locates at the barrier layer according to previous study,[40] and as such a small rutile peak can be observed in the subsequent spectra. Similar to the Raman spectra, no significant changes were observed in the spectra due to irradiation. It is of interest to note, that in both of the ion irradiated samples there is a slight reduction in diffraction angle which may be attributed to expansion of the lattice due to the increase in defects within the oxide, however this shift is within the margin of instrumental error.

After microstructural characterization, the electrodes were evaluated as anodes in half-cells. The non-irradiated anatase control sample has an initial charge capacity of 4.37 x 10^{-2} mAh/cm^2, which leveled off to 3.57x10^{-2} mAh/cm^2 at C/12 after 10 cycles (Figure 4.5). This capacity is significantly lower than what was observed for the irradiated nanotube electrodes. The TiO_2 electrode irradiated at 25 ˚C has an initial charge capacity of 6.92x10^{-4} mAh/mm^2 which stabilized at 5.39x10^{-2} mAh/cm^2 after 10 cycles, whereas the electrode irradiated at 250 ˚C exhibited a charge capacity of 8.35x10^{-2} mAh/cm^2, which leveled off at 6.69x10^{-2} mAh/cm^2 by the tenth cycle. This correlates to a 33% and 46% increase in capacity for the 25 ˚C and 250 ˚C irradiations, respectively. Additionally, the Coulombic efficiency for the electrodes were 91.5% for the non-irradiated control, 94.6% for the 25 ˚C irradiated sample, and 92.3% for the 250 ˚C irradiated sample at the 10^{th} cycle.

Figure 4.6 compares the charge/discharge profiles of the irradiated and control anatase samples cycled between 0.9 and 2.5 V (vs Li/Li$^+$) at a low current rate. Lithium insertion in the anatase TiO_2 NT electrodes via a two-phase mechanism which occurs at the characteristic plateau of approximately 1.7 V vs Li/Li$^+$, indicating the coexistence of a Li-poor phase $Li_{0.05}TiO_2$, which maintains the original anatase structure (space group:*I4$_1$/amd*) and a Li-rich phase $Li_{0.5}TiO_2$ (space group: *Imma*). After irradiation, both the high temperature and room temperature samples display this two-phase region. The overall capacity contribution from the sloping regions is 78%, 66%, and 58% for the sample irradiated at 250 °C, 25 °C and the non-irradiated sample, respectively, meaning that the increase in capacity is attributed to larger sloping regions due to the increased presence of defects sites which facilitate lithium intercalation. The capacity contribution

values are calculated by taking the capacity from the sloping regions over the total capacity of the cell.

In order to better understand the charge storage and transport mechanism behind the variance in electrochemical performance, electrochemical impedance spectroscopy (EIS) was used. In short, a modulating potential is applied to a cell, and the resulting current is recorded, which allows for exploration of charge storage behavior.[40] Nyquist plots for the irradiated and control samples are shown in Figure 4.7. These plots contain overlapping semi-circles at the high/medium frequency range, followed by a straight line at lower frequencies. The equivalent circuit used to model this system is shown in the inset of Figure 4.7. In this equivalent circuit the R_1 is the bulk resistance of the cell (electrolyte, separator, electrode), C_2 and R_2 belong to the capacitance and resistance of the passivation layer on the surface of the TiO_2. C_2 and R_2 are minimized in this experiment by uncycled TiO_2 electrodes, thereby minimizing the formation of solid electrolyte interphase (SEI). C_3 and R_4 correspond to the main semi-circle, which represents capacitance and resistance for the charge-transfer resistance, and W is the Warburg impedance from the diffusion of Li^+ ions within the electrode.[42-43] The Nyquist plots show that the charge transfer resistance of the TiO_2-NT sample irradiated at 250 ˚C is lower than that of the TiO_2-NT sample irradiated at 25 ˚C, while both irradiated samples have a lower charge transfer resistance than the non-irradiated anatase control, suggesting better charge transfer kinetics in the irradiated samples. Once the data has been carefully fit to an equivalent circuit, lithium diffusivity values (Table 4.1) can be calculated from the Warburg impedance by the equation[40]:

$$D_{Li} = \frac{R^2T^2}{2C_{Li}^2\sigma^2n^4F^4A^2}$$

where R is the gas constant, T is the absolute temperature, C_{Li} is the Li concentration in the electrolyte, n is the transferred charge, F is Faraday's constant, and A is the geometric surface area. The electrodes exhibit diffusivities of $2.3x10^{-13}$ cm^2/s, $1.0x10^{-12}$ cm^2/s, and $1.3x10^{-11}$ cm^2/s for the non-irradiated control, 25 ˚C irradiation, and 250 ˚C irradiation respectively. The improvement to the diffusivity may be attributed to the vacancies within the anatase structure allowing for improved reaction kinetics, as shown in Chapter Two.

Rate capability measurements were taken to determine how irradiation affects the electrochemical performance of the TiO_2 nanotubes at elevated current rates (Figure 4.8). At C/2, it is apparent that the high temperature proton irradiated electrode has the best performance with 0.0005 mAh/mm^2 compared to less than 0.0003 mAh/mm^2 for the non-irradiated specimen. Even at very high rates of 20C, both irradiated conditions have higher capacity than the non-irradiated anatase, and at 100C the capacity of both room temperature and non-irradiated anatase nanotubes drops off drastically while the high temperature specimen maintains about 20% of the low rate charge storage capacity. The increase of in lithium diffusivity of the high temperature irradiated electrode enhances the high rate performance, allowing for enhanced kinetic behavior. It is possible that the increase in electrochemical behavior at higher temperatures is caused by promotes rapid defect accumulation, and possibly the formation of atomic scale defect clusters within the anatase crystal structure.

4.5 Conclusions

In this study, the effect of irradiation on anatase TiO_2 NT electrodes was evaluated. It was found that while structural integrity and phase composition is

maintained, there is still significant alterations to the electrochemical response of the TiO_2 NT after it has been irradiated with protons at 25 °C and 250 °C. Results from Raman spectroscopy and XRD indicate that under both irradiation conditions the final structure remains primarily anatase. Both high temperature and room temperature irradiated samples exhibit two-phase intercalation mechanisms, and the increase in capacity can be attributed to the increase of lithium diffusion into defect sites, as apparent by the increased contribution to capacity of the sloping regions. It is likely that irradiating at higher temperatures promotes more rapid defect accumulation, and possibly the formation of atomic scale defect clusters, within the anatase crystal structure. While defects are more mobile at elevated temperatures, 250 °C is not high enough to cause rapid annealing of defects out of the anatase structure. It is suggested then, that while defects are formed in the room temperature irradiated sample as evident by the change in electrochemical behavior, the rate of defect accumulation is increased in the high temperature irradiated anatase. When tested in a lithium half-cell, the irradiated cells exhibit a 33% and 47% increase in capacity for the 25 °C and 250 °C proton irradiation, respectively.

4.6 Figures and Tables

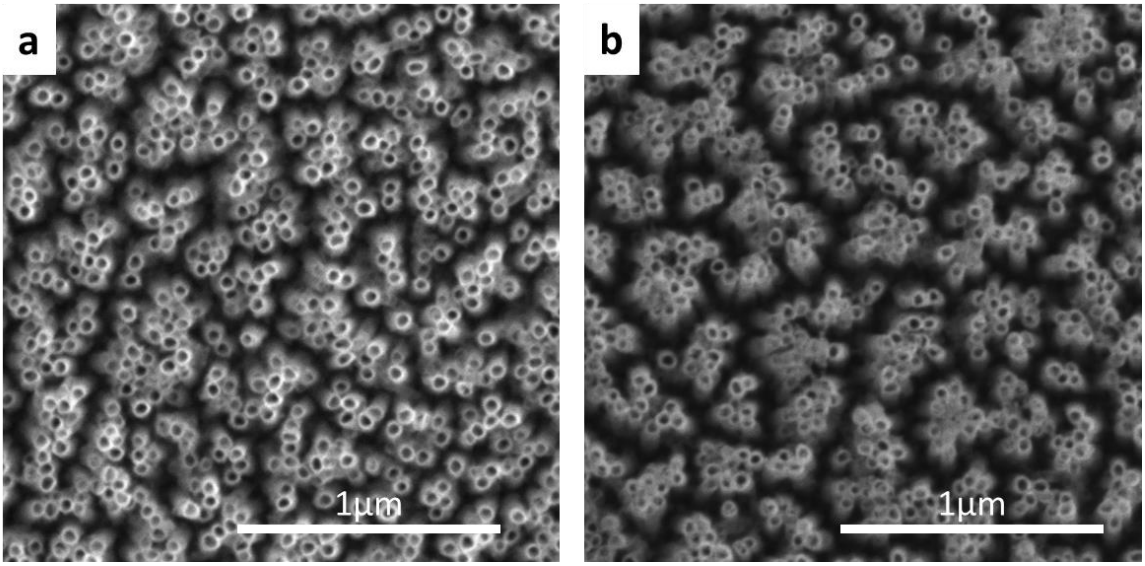

Figure 4.1: a) as-prepared amorphous TiO_2 nanotubes, b) TiO_2 nanotubes after annealing and irradiating with protons at 25 ˚C. (In Submission)

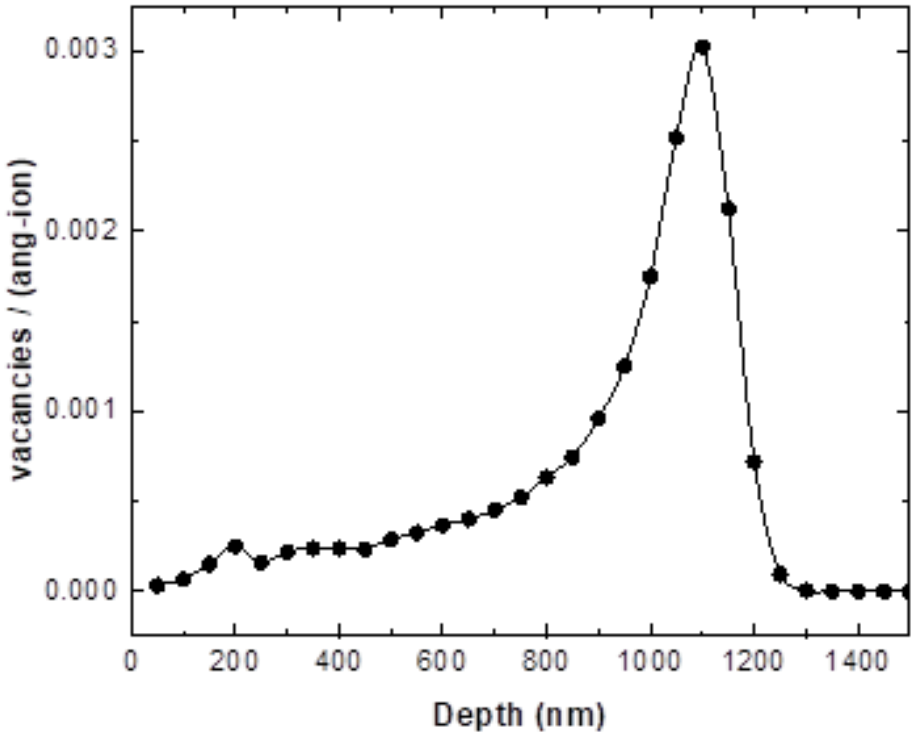

Figure 4.2: Damage depth distribution calculation of H^+ ions on anatase. (In Submission)

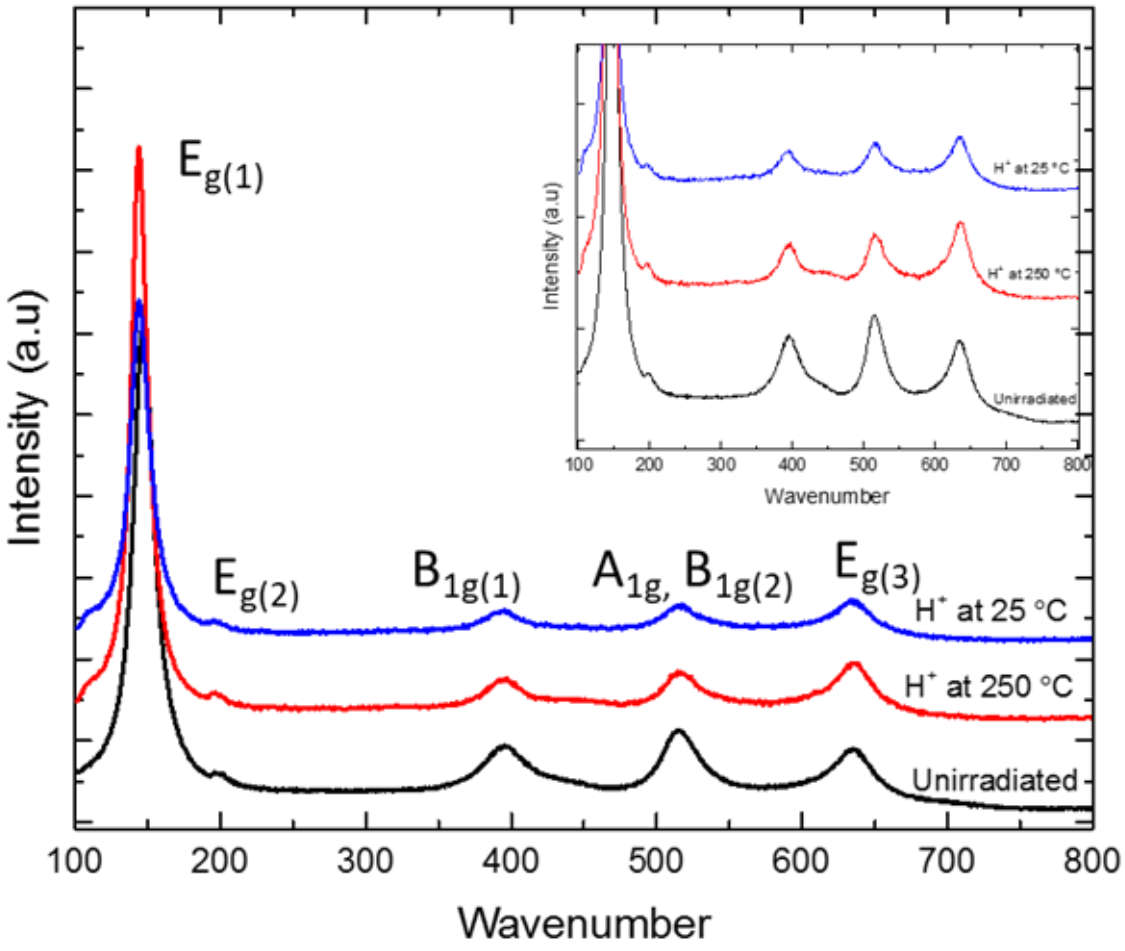

Figure 4.3: Raman spectra of non-irradiated anatase nanotubes (black), 250 °C H^+ irradiated anatase (red) and 25 °C H^+ irradiated anatase (blue). (In Submission)

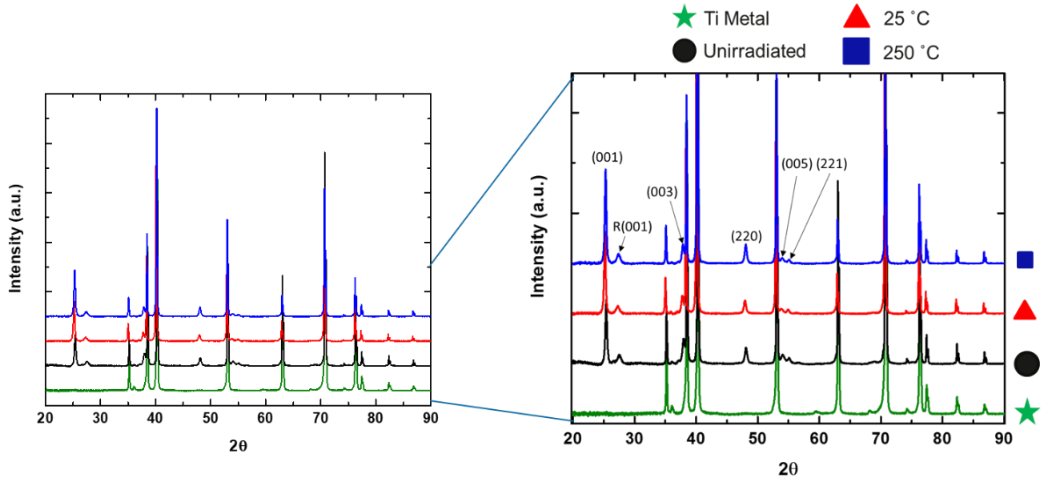

Figure 4.4: X-ray diffraction spectra (XRD) of TiO_2 nanotubes before and after proton irradiation. (In Submission)

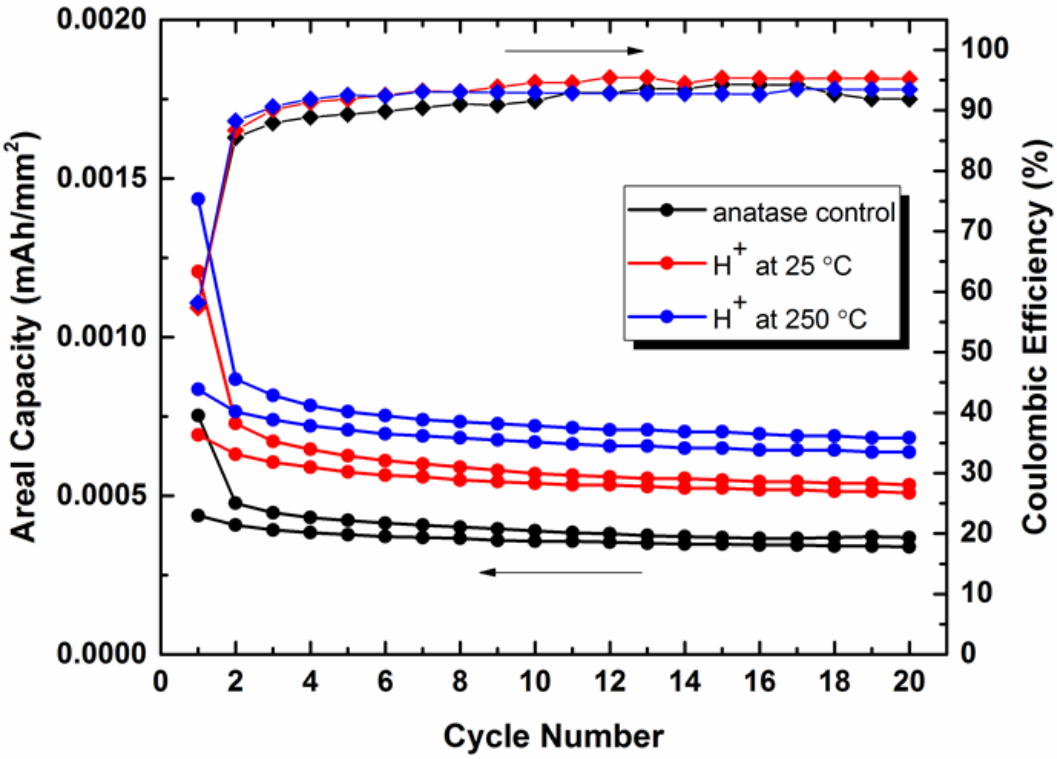

Figure 4.5: Low rate galvanostatic cycling of non-irradiated anatase nanotubes (black), 25 °C H^+ irradiated nanotubes, and 250 °C H^+ irradiated nanotubes. (In Submission)

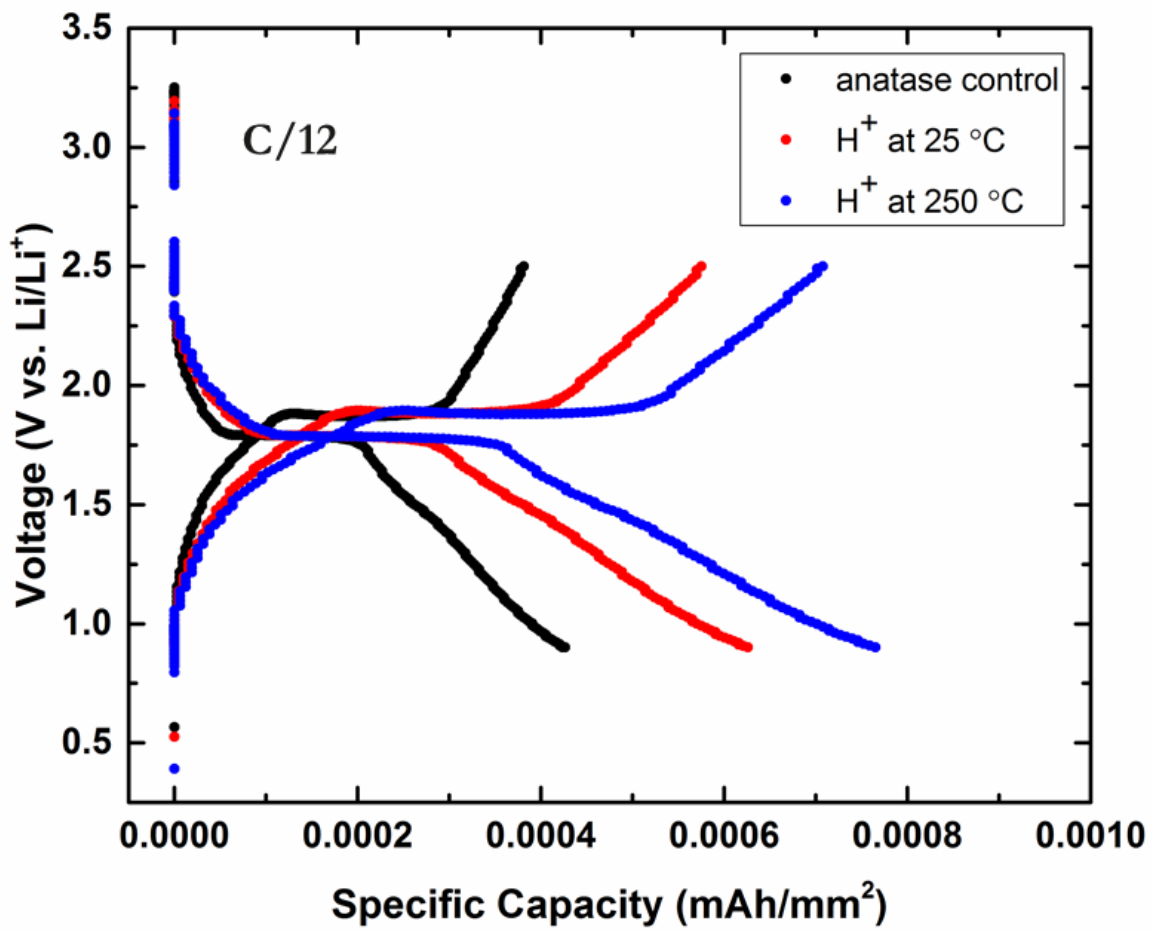

Figure 4.6: Charge/discharge plots comparing the 5th cycle of the non-irradiated (black), room temperature proton irradiated (red) and high temperature proton irradiated (blue) anatase electrodes. (In Submission)

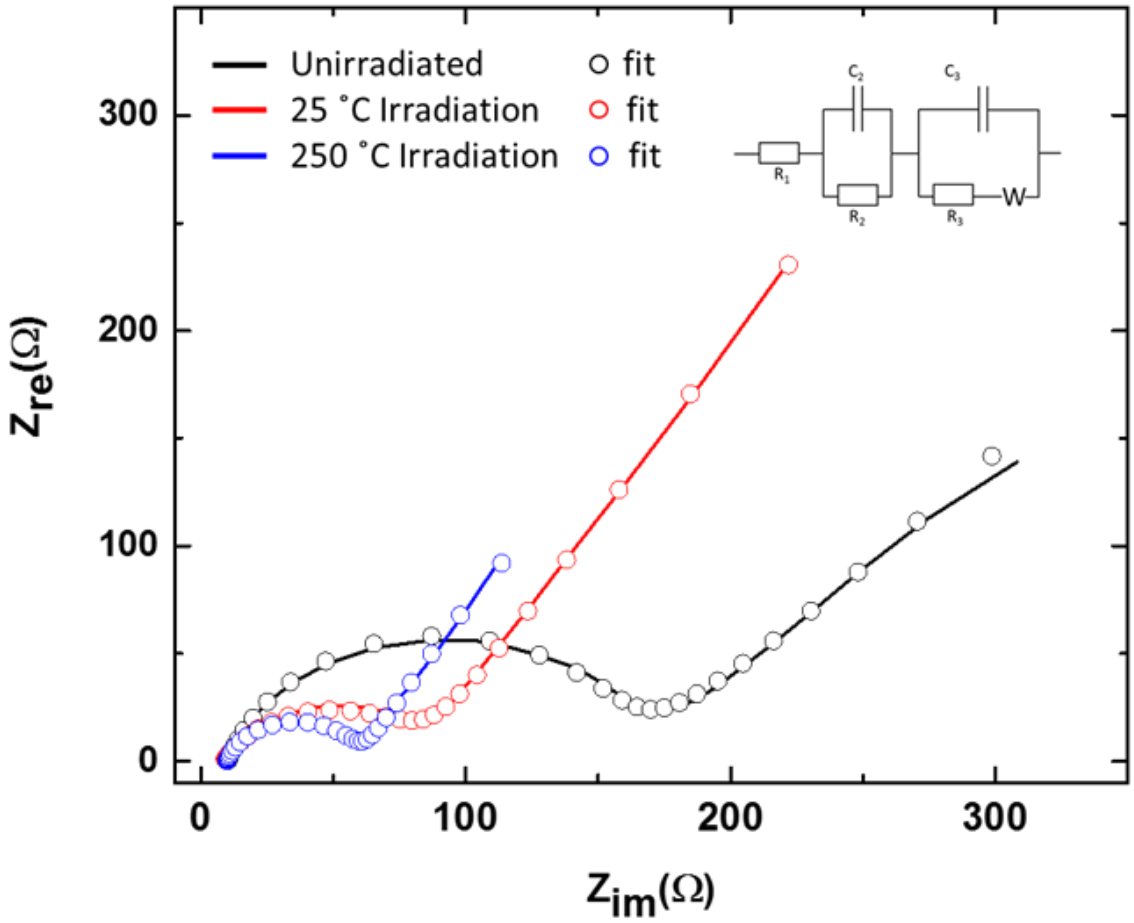

Figure 4.7: Nyquist plots of non-irradiated, room temperature irradiated, and high temperature irradiated anatase nanotube electrodes. (In Submission)

Table 4.1: Lithium diffusivity values calculated from Warburg impedance measured by EIS of the non-irradiated and irradiated anatase nanotube electrodes. (In Submission)

Electrode	Li Diffusivity (cm^2/s)
Non-irradiated	2.3×10^{-13}
Proton at 25 °C	1.0×10^{-12}
Proton at 250 °C	1.3×10^{-11}

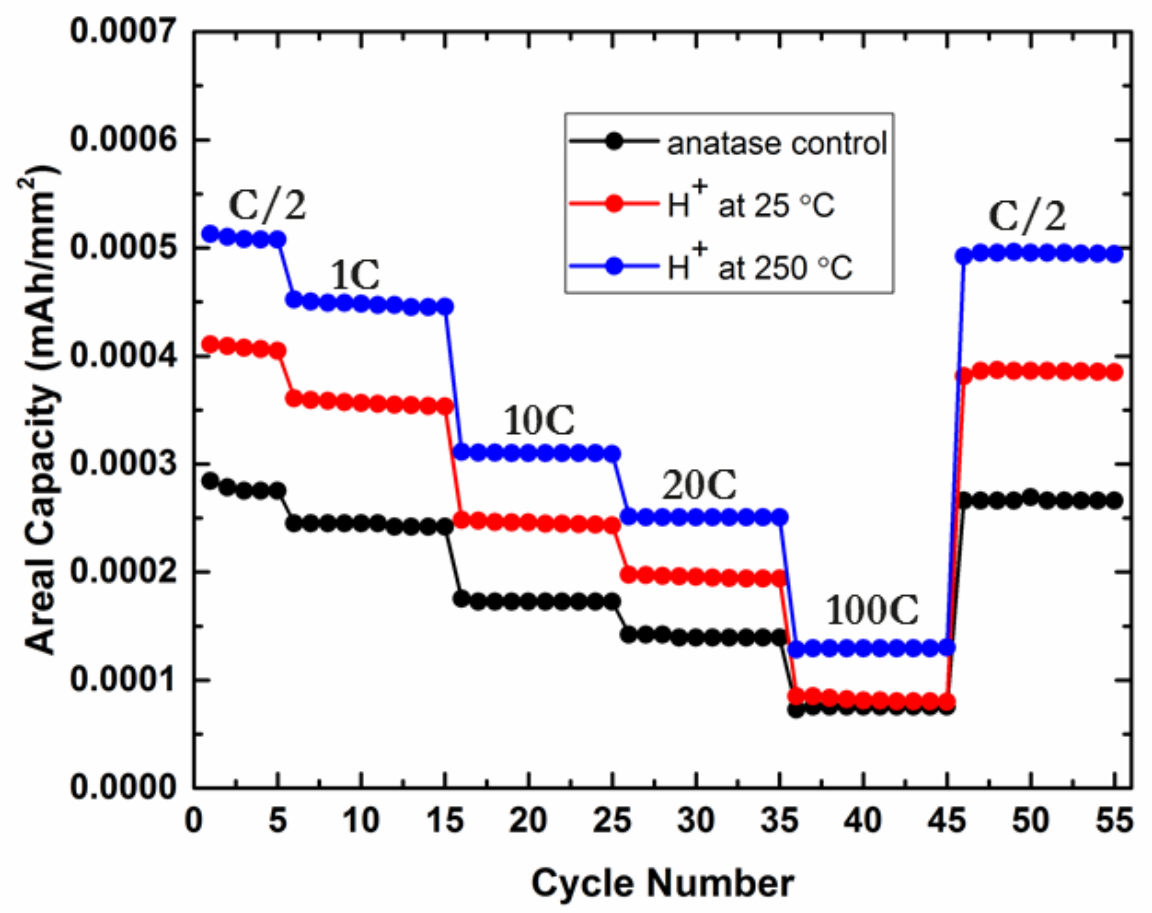

Figure 4.8 Rate capability plot of non-irradiated, room temperature irradiated, and high temperature irradiated anatase nanotubes. (In Submission)

4.7 References

1. P. G. Bruce, B. Scrosati and J. M. Tarascon, *Angew. Chem., Int. Ed.*, 2008, **47**, 2930-2946.
2. D. Deng, M. G. Kim, J. Y. Lee and J. Cho, *Energ Environ Sci*, 2009, **2**, 818-837.
3. Z. G. Yang, D. Choi, S. Kerisit, K. M. Rosso, D. H. Wang, J. Zhang, G. Graff and J. Liu, *J Power Sources*, 2009, **192**, 588-598.
4. G. N. Zhu, Y. G. Wang and Y. Y. Xia, *Energ Environ Sci*, 2012, **5**, 6652-6667.
5. C. J. Howard, T. M. Sabine and F. Dickson, *Acta Crystallogr., Sect. B: Struct. Crystallogr. Cryst. Chem.*, 1991, **47**, 462-468.

6. B. Zachauchristiansen, K. West, T. Jacobsen and S. Atlung, *Solid State Ionics*, 1988, **28**, 1176-1182.

7. A. S. Arico, P. Bruce, B. Scrosati, J. M. Tarascon and W. Van Schalkwijk, *Nat Mater*, 2005, **4**, 366-377.

8. J. S. Chen, Y. L. Tan, C. M. Li, Y. L. Cheah, D. Luan, S. Madhavi, F. Y. C. Boey, L. A. Archer and X. W. Lou, *J. Amer. Chem. Soc.*, 2010, **132**, 6124-6130.

9. L. Kavan, M. Kalbac, M. Zukalova, I. Exnar, V. Lorenzen, R. Nesper and M. Graetzel, *Chem Mater*, 2004, **16**, 477-485.

10. J. Maier, *J Power Sources*, 2007, **174**, 569-574.

11. A. Manthiram, A. V. Murugan, A. Sarkar and T. Muraliganth, *Energ Environ Sci*, 2008, **1**, 621-638.

12. M. Wagemaker, W. J. H. Borghols and F. M. Mulder, *J. Amer. Chem. Soc.*, 2007, **129**, 4323-4327.

13. Y. Wang and G. Z. Cao, *Adv Mater*, 2008, **20**, 2251-2269.

14. J. M. Tarascon and M. Armand, *Nature*, 2001, **414**, 359-367.

15. K. A. Smith, A. I. Savva, C. Deng, J. P. Wharry, S. Hwang, D. Su, Y. Wang, J. Gong, T. Xu, D. P. Butt and H. Xiong, *J. Mater. Chem. A.*, 2017, DOI: 10.1039/C7TA01026E.

16. B. P. Hahn, J. W. Long and D. R. Rolison, *Accounts. Chem. Res.*, 2013, **46**, 1181-1191.

17. B. Koo, S. Chattopadhyay, T. Shibata, V. B. Prakapenka, C. S. Johnson, T. Rajh and E. V. Shevchenko, *Chem. Mater.*, 2013, **25**, 245-252.

18. B. Koo, H. Xiong, M. D. Slater, V. B. Prakapenka, M. Baasubramanian, P. Podsiadlo, C. S. Johnson, T. Rajh and E. V. Shevchenko, *Nano. Lett.*, 2012, **12**, 2429-2435.

19. G. S. Was, *Fundamentals of radiation materials science : metals and alloys*, Springer, Berlin, 2007.

20. H. A. Shukur, M. Sato, I. Nakamura and I. Takano, *Adv Mater Sci Eng*, 2012, **2012**, 1-7.

21. G. R. Lumpkin, K. L. Smith, M. G. Blackford, B. S. Thomas, K. R. Whittle, N. A. Marks and N. J. Zaluzec, *Phys. Rev. B: Condens. Matter*, 2008, **77**.

22. H. Rath, P. Dash, T. Som, P. V. Satyam, U. P. Singh, P. K. Kulriya, D. Kanjilal, D. K. Avasthi and N. C. Mishra, *J. Appl. Phys.*, 2009, **105**, 074311.

23. B. P. Uberuaga and X. M. Bai, *J. Phys.: Condens. Matter*, 2011, **23**.

24. M. J. Qin, E. Y. Kuo, K. R. Whittle, S. C. Middleburgh, M. Robinson, N. A. Marks and G. R. Lumpkin, *J. Phys.: Condens. Matter*, 2013, **25**, 355402.

25. F. Li, P. Lu and K. E. Sickafus, *J. Nucl. Mater.*, 2002, **306**, 121-125.

26. T. Hartmann, L. M. Wang, W. J. Weber, N. Yu, K. E. Sickafus, J. N. Mitchell, C. J. Wetteland, M. A. Nastasi, M. G. Hollander, N. P. Baker, C. R. Evans, J. R. Tesmer and C. J. Maggiore, *Nucl. Instrum. Methods Phys. Res., Sect. B*, 1998, **141**, 398-403.

27. N. Liu, V. Haublein, X. M. Zhou, U. Venkatesan, M. Hartmann, M. Mackovic, T. Nakajima, E. Spiecker, A. Osvet, L. Frey and P. Schmuki, *Nano Lett*, 2015, **15**, 6815-6820.

28. H. Xiong, M. D. Slater, M. Balasubramanian, C. S. Johnson and T. Rajh, *J Phys Chem Lett*, 2011, **2**, 2560-2565.

29. H. Xiong, H. Yildirim, E. V. Shevchenko, V. B. Prakapenka, B. Koo, M. D. Slater, M. Balasubramanian, S. K. R. S. Sankaranarayanan, J. P. Greeley, S. Tepavcevic, N. M. Dimitrijevic, P. Podsiadlo, C. S. Johnson and T. Rajh, *J Phys Chem C*, 2012, **116**, 3181-3187.

30. P. Barnes, A. Savva, K. Dixon, H. Bull, L. Rill, D. Karsann, S. Croft, J. Schimpf and H. Xiong, *Surf. Coat. Technol.*, 2018, **347**, 150-156.

31. J. F. Ziegler, Biersack, J. P., Littmark, U., *Pergamon Press: New York*, 1985.

32. E. Silva, F. A. La Porta, M. S. Liu, J. Andres, J. A. Varela and E. Longo, *Dalton T*, 2015, **44**, 3159-3175.

33. P. Tengvall, T. P. Vikinge, I. Lundstrom and B. Liedberg, *J Colloid Interf Sci*, 1993, **160**, 10-15.

34. S. Sahoo, A. K. Arora and V. Sridharan, *J Phys Chem C*, 2009, **113**, 16927-16933.

35. Y. Lei, L. D. Zhang and J. C. Fan, *Chem Phys Lett*, 2001, **338**, 231-236.

36. W. B. Hu, L. P. Li, G. S. Li, C. L. Tang and L. Sun, *Cryst Growth Des*, 2009, **9**, 3676-3682.

37. V. Swamy, B. C. Muddle and Q. Dai, *Appl Phys Lett*, 2006, **89**.

38. V. Swamy, A. Kuznetsov, L. S. Dubrovinsky, R. A. Caruso, D. G. Shchukin and B. C. Muddle, *Phys Rev B*, 2005, **71**.

39. O. Varghese, D. Gong, M. Paulose, C. Grimes, E. Dickey, *J. Mater. Res.*, 2011, **18**, 156-165.

40. M. E. Orazem and B. Tribollet, *Electrochemical impedance spectroscopy*, Wiley, Hoboken, N.J., 2008.

41. M. D. Levi, G. Salitra, B. Markovsky, H. Teller, D. Aurbach, U. Heider and L. Heider, *J. Electrochem. Soc.*, 1999, **146**, 1279-1289.

42. R. Ruffo, S. S. Hong, C. K. Chan, R. A. Huggins and Y. Cui, *J Phys Chem C*, 2009, **113**, 11390-11398.

43. B. L. He, B. Dong and H. L. Li, *Electrochem Commun*, 2007, **9**, 425-430.

CHAPTER FIVE: Effects of Intermediate Energy Heavy-ion Irradiation on the Microstructure of Rutile TiO_2 Single Crystal

This chapter is published by John Wiley and Sons in the *Journal of the American Ceramic Society* and should be referenced appropriately.

Reference:

K. Smith[a], A. Savva[a], Y. Wu[b], D. Tenne[c], D. Butt[d], H. Xiong[a], and J. Wharry[e] " Effects of intermediate energy heavy-ion irradiation on the microstructure of rutile TiO_2 single crystal" *J. Amer. Ceram. Soc.* **9** 4357-4366 (2018).

*This chapter includes modifications from the originally published version.

Effects of Intermediate Energy Heavy-ion Irradiation on the Microstructure of Rutile TiO_2 Single Crystal

Kassiopeia A. Smith[a]

Andreas I. Savva[a]

Yaqiao Wu[b]

Dmitri Tenne[c]

Darryl Butt[d]

Hui Xiong[a]

Janelle Wharry[e]

[a]*Micron School of Materials Science & Engineering, Boise State University, 1910 University Drive, Boise ID 83725*

[b]*Center for Advanced Energy Studies, 995 University Boulevard, Idaho Falls ID 83401*

[c]*Department of Physics, Boise State University, 1910 University Drive, Boise ID 83725*

[d]*College of Mines and Earth Sciences, University of Utah, 115 S 1460 E, Salt Lake City, UT 84112*

[e]*School of Nuclear Engineering, Purdue University, 400 Central Drive, West Lafayette IN 47907*

5.1 Abstract

This study reports the microstructure evolution of single crystal rutile TiO_2 under 3 MeV Nb^+ ion irradiation, with the irradiating ions incident on the {100} plane. A complex, multi-layered microstructure evolution is observed with four distinct regions: (1) short-range disorder in the first 60 nm below the specimen surface, (2) dislocation loops oriented parallel to the incident ion beam direction, located along the increasing slope of the irradiation damage profile at ~60-650 nm from the surface, (3) loops oriented perpendicular to the incident ion beam direction, at depths encompassing the ion implantation and irradiation damage peaks ~650-1250 nm, and (4) a high density of nano-scale atomic rearrangements with long-range order, located at depths ~1250-1750 nm. These results present evidence that multiple defect mechanisms occur during irradiation including ion channeling, nuclear stopping, and electronic stopping interactions as a function of depth and disorder accumulation.

5.2 Introduction

Titanium dioxide (TiO_2) is an important material used across many scientific and industrial sectors with applications ranging from cosmetics and plastics to water purification and energy storage.[1-3] TiO_2 is widely regarded as an ideal functional material because of its low cost, high chemical stability, and safety in terms of both human and environmental impact. TiO_2 is also an important material for a variety of sensor, optoelectrical, nuclear waste, and absorption applications, during which the material will be exposed to irradiation. Hence, the effects of irradiation on the TiO_2 must be understood. In recent years, a body of work has been generated on the effects of irradiation on TiO_2.

Separate studies by Zheng et al.[4] and Qin et al.[5] indicated that photovoltaic properties were increased in thin film anatase substrates when irradiated with low energy metal ions to nominal doses (10^{13} to 10^{16} ions cm^{-2}), though Zheng et al.[6] later argued that higher doses (10^{17} ions cm^{-2}) caused recombination centers to form resulting in reduced overall photocatalytic activity. In addition to photocatalytic applications, Jensen et al.[7] observed that irradiating with Fe ions at doses of 10^{16} ions cm^{-2} induced ferromagnetic behavior. Other studies have shown enhancement of UV and optical absorption, and water splitting behaviors in anatase thin films with similar irradiation conditions.[8, 9] In studying rutile thin films, it has been observed that rutile has better resistance to amorphization than other TiO_2 polymorphs, possibly due to atomic packing densities.[8, 10, 11] Computational simulations by Uberuagua, Qin, and Lumpkin have supported these experiments and given details into the mechanisms of defect accumulation and amorphization resistance.[10, 12, 13] Temperature dependence studies by Li et al.[14] have shown that when irradiating at higher temperatures, point defects were more mobile and allowed for damage recovery. Conversely, at room temperature the irradiation damage was more likely to form stable irradiation-induced point defects which was later supported by Zhang and coworkers.[15] Hartmann et al.[16] showed that using lighter irradiation species such as He^{+} are more likely to amorphize target substrates than heavy noble gases such as Xe^{2+} and Ne^{+}. Our recent study showed that proton irradiation could induce phase transformation in amorphous TiO_2 nanotubes to a disordered rutile phase at temperature of 250 ˚C.[17]

Although these recent studies have shed light on the effects of irradiation on the order and functionality of TiO_2, there remains limited understanding of the underlying

microstructure-based mechanisms for these irradiation-induced changes. Fundamental microstructural phenomena are difficult to ascertain because many of these aforementioned irradiation studies of TiO_2 have utilized low-energy implantations (i.e. tens to a few hundred keV) on polycrystalline substrates. The shallow damage profiles from ~keV irradiation renders it difficult to resolve differences in microstructure evolution as a function of depth, a task which is further complicated by the presence of interfaces and grain boundaries in polycrystalline materials. Basic irradiation-induced microstructure evolution mechanisms may be more readily observed if a single crystal specimen is irradiated with intermediate-energy heavy ions. Nb^+ ions have been chosen in this case, as niobium doping has widely been used to enhance a variety of properties of TiO_2.[18-26]

The objective of this study is to examine the defect microstructures, which arise from Nb^+ ion irradiation on the {100} orientation of rutile single crystal TiO_2. Though rutile is thought to be more resistant to irradiation-induced amorphization, it is selected for this study because the mechanism for atomic rearrangement and the resulting disordered crystalline matrix is not yet known. Microstructure characterization utilizes a combination of x-ray diffraction, Raman spectroscopy, and transmission electron microscopy. Results from each technique will be presented individually and then integrated to understand the complex layered microstructure evolution.

5.3 Experimental

5.3.1 Materials and Irradiation

Rutile single crystal TiO_2 (100) specimens, 5x5x0.5 mm, were obtained from MTI Corp. for ion irradiation. The surface finish was <5 Å to reduce the amount of surface

residual stress and damage, to which the near-surface ion irradiation damage layer is sensitive. Specimens were oriented such that the (100) plane was perpendicular to the ion beam. Irradiation with 3 MeV Nb^{+} ions was conducted using a raster-scanned beam at high vacuum ($<10^{-7}$ torr) in the 1.7 MV General Ionex Tandetron at the Michigan Ion Beam Laboratory with an average current of 52.8 nA, and a fluence of $4.03x10^{11}$ ions/s over a 0.4 cm^2, which translates to a dose rate of $9.28x10^{-4}$ dpa/s. Raster scanning occurred at a frequency of 2061 Hz in the vertical direction and 255 Hz in the horizontal direction. The duration of one scanning cycle was 0.48 ms in the vertical and 3.92 ms in the horizontal. The ratio of the vertical to horizontal scanning cycles was a non-integer number, such that that the beam path was offset from the previous scan cycle, ensuring good spatial uniformity of the scanned beam area. Because the beam scanning occurred at such a rapid frequency, and because the beam cycle fully and uniformly covered the specimen, the thermal effect on the specimen was uniform (i.e. non-localized) heating. We utilized a thermal imaging system to initially calibrate the specimen to the desired room temperature and then monitored the specimen temperature continually throughout the experiment. The thermal imaging system had temperature resolution ±2°C and spatial resolution 5-14 μm (depending on the distance between the specimen and the thermal imaging system's focal plane). This spatial resolution was significantly lower than the 3 mm diameter of the rastered beam and thus would be sufficient to detect local heating from the beam. During irradiation, the specimen back temperature was maintained using a combination of a liquid nitrogen cooling loop and a cartridge heater. This combined heating and cooling approach enabled higher precision control of the specimen

temperature. Temperatures recorded throughout the experiment show that all regions of the specimen never exceeded more than 20°C above room temperature.

The irradiation damage profile (Fig. 5.1) was calculated from the "Quick Calculation" or Kinchin-Pease mode 26 within Stopping Range of Ions in Matter (SRIM) 2013.[27] Displacements were obtained from the vacancy.txt file. SRIM calculations used a 0.5 mm compact layer of TiO_2, with a density of 4.23 g/cm^2, and displacement energies of 25 eV and 28 eV for Ti and O, respectively. The damage profile corresponded to a dose of 6.5 displacements per atom (dpa) at the sample surface, rising to 23 dpa at the damage peak, which was located ~900 nm from the surface. The Nb^+ implantation peak was located approximately 1100 nm below the sample surface with a maximum implantation depth of ~1.45 μm.

5.3.2 Electron Microscopy

Site-specific transmission electron microscopic (TEM) lamella lift-out specimens were made using the FEI Quanta 3D FEG FIB at the Microscopy and Characterization Suite (MaCS) Center for Advanced Energy Studies (CAES).[28] Prior to milling, a layer of platinum was deposited to protect the original irradiated surface. The TEM lamellae were bulk milled at 30 kV to form a rectangular cross section that was approximately 15 μm x 10 μm x 100 nm, followed by further milling at 5 kV to a thickness of about 50-100 nm. Last, a 2 kV cleaning step was applied to reduce surface damage incurred on the surface of the sample by the milling steps. Two sets of TEM lamellae were made in order to observe the microstructure in two directions: the first set was oriented perpendicular to the irradiated surface (i.e. parallel to the ion beam direction), such that the ion irradiation

damage profile was observed through the depth of the specimen, while the second set was perpendicular to the ion beam direction.

TEM specimens were analyzed using an FEI Tecnai TF30-FEG STwin STEM at CAES, which had a point-to-point resolution of 0.19 nm in TEM mode. In order to characterize the mesoscopic irradiated microstructure, specimens were tilted to the pole axis and observed in bright field imaging mode.[29] High resolution-TEM (HR-TEM) imaging was subsequently utilized to ascertain information about crystallinity.

5.3.3 Raman Spectroscopy and X-Ray Diffraction

The single crystal samples were evaluated using Raman spectroscopy and X-ray diffraction (XRD). Raman has long been used to characterize the local and long-range order of crystalline samples by giving insight to dynamic interactions of the lattice structure, and has been widely used to investigate the various polymorphs of TiO_2. Hence, there is a wide body of literature on the Raman response of this material.[30-36] XRD is a complimentary technique, which provides information on the overall crystallinity and phase of the material.[37]

Raman spectra were measured in backscattering geometry using a Jobin Yvon T64000 triple spectrometer equipped with a liquid nitrogen cooled multichannel charge coupled device detector. The 325 nm line of He-Cd laser and 514.5 nm line of Ar ion lasers were used for excitation; maximum laser power density is 0.5 W/mm^2 at the sample surface. Spectra are recorded at 10 K using an evacuated closed cycle helium cryostat. XRD was obtained by Rigaku Miniflex diffractometer with Cu K_α irradiation at λ = 1.5406 Å.

5.4 Results and Discussion

TiO_2 is a wide band-gap material and absorbs light in the ultraviolet (UV) region. The Nb-ion irradiated rutile TiO_2 (100) samples evolved from transparent to an opaque black color, which was indicative of defect production that altered the band structure of TiO_2. The irradiation-induced structural and microstructural changes were studied using TEM, Raman and XRD.

5.4.1 Structural Characterization

Rutile is the most thermodynamically stable form of TiO_2 with a tetragonal $P4_2/mnm$ space-group, where $a = b = 4.625$ Å and $c = 2.959$ Å. The unit cell is comprised of two TiO_2 molecules with each Ti atom having 6 oxygen nearest neighbors. The four Raman active vibrational modes found in rutile TiO_2 are B_{1g} (143 cm^{-1}), E_g (447 cm^{-1}), A_{1g} (612 cm^{-1}), and B_{2g} (826 cm^{-1}).[35,38] Raman spectroscopy can be conducted at a range of energies by altering the laser excitation wavelength, which in turn affects which vibrational modes are activated, in addition to the depth of the investigation.

Raman spectra were first obtained using a UV laser (325 nm wavelength), which sampled the top 5-10 nm of the specimen.[50] In this region (Fig. 5.2a), both the non-irradiated and Nb^+ irradiated samples exhibited a broad band near 213 cm^{-1}, which was attributed to a combinatorial band[52], as well as a sharp peak at 612 cm^{-1} corresponding to the A_{1g} band. These two bands were largely unaltered by the irradiation. On the other hand, in the Nb^+ irradiated sample, a sharp B_{2g} peak emerged at 826 cm^{-1}. This band is not commonly observed in TiO_2, and when it does appear, it is typically a weak signal[56] unlike the clearly defined peak shown herein. The B_{2g} vibrational mode represents an antisymmetric Ti-O distortion of the TiO_6 octahedra, which is sensitive to the local

environment of the Ti ions. [39,40] This marked increase in the B_{2g} mode suggests that the local Ti environment changed, leading to an increase in the vibrational intensity of this mode.

Raman spectra were also obtained using an argon laser (514.4 nm wavelength), which sampled depths of approximately 1 μm for TiO_2.[33] There was no significant difference between the Raman spectra of the non-irradiated and irradiated samples at this wavelength (Fig. 5.2b). Results from both excitation wavelengths (325 nm and 514.4 nm) collectively suggest that while the majority of the irradiated region appears to maintain long-range order, the surface 5-10 nm region of the specimen has an altered binding state containing a higher concentration of defects.

The XRD spectrum (Fig. 5.3) exhibited 2θ peaks at approximately 39.3° and 84.3°, which correspond to the 100 rutile structure. After Nb^+ irradiation, these peaks shifted to smaller angles by ~0.1-0.2°, suggesting that the irradiated rutile structure has larger unit cell. This finding corroborates the Raman results, which indicate disorder at the surface of the specimen. The irradiated rutile XRD spectrum also exhibited peak broadening and a reduction in intensity, which can be attributed to the disorders induced by irradiation.

5.4.2 Microstructural Characterization

TEM revealed microstructure evolution induced by Nb^+ irradiation. Cross-sectional TEM lamellae were prepared from the ion-implanted crystals to examine the nature and distribution of defects as a function of depth along the damage profile. In-plane lamellae were also prepared to characterize the spatial extent of defects at depths of

interest as determined by the results of imaging the cross-sectional lamellae. Results from both lamellae orientations are presented below.

The cross-sectional TEM lamella revealed four distinct damage regions (Fig. 5.4), ranging from the surface to a depth of ~1700 nm. It is not unusual for irradiated rutile single crystals to exhibit different damage microstructures near the damage and implantation peaks, as compared to the near-surface region.[41-44] However, none of these previous studies reported such a complex, multi-layered defect structure as that observed herein. The multi-layered damage structure could be associated with the energy of the irradiation ion, which is an order of magnitude larger than those reported. [41-44] Characteristics of each of these four layers are described below in greater detail.

Region 1 – The damage region within 60 nm of the initial irradiated surface, which corresponds to an irradiation dose of ~9 dpa, exhibits a homogenous bright field (BF) contrast. From the HR-TEM imaging of this region (Fig. 5.5a, b), we see that within the first 10 nm of Region 1 the sample is heavily disordered and the corresponding convergent beam electron diffraction (CBED) of the region indicates reorientation into the 101 direction (Fig. 5.5c). Since this region is only about 60 nm, CBED technique is selected rather than general selected area electron diffraction (SAED) technique. This result is consistent with an earlier report from Li et al., in which rutile 100 single crystals were irradiated with 360 KeV Xe^{2+} ions, and the 12 nm region nearest to the surface was reoriented into the 011 orientation. [45] This finding is in agreement with our UV Raman result, which shows short-range disorder of the surface region while maintaining long-range order.

Region 2 – This 650 nm region contains defects, potentially ion tracks or dislocation loops, that tend to be aligned parallel to the ion beam direction (Fig. 5.6a, b). However, it has been reported that ion tracks only form in rutile TiO_2 under swift heavy ion irradiation when electronic stopping exceeds 6.2 keV/nm.[46,47] Since the 2.5 MeV Nb^+ ions herein do not provide sufficient electronic stopping, amorphous ion tracks are not expected to form. In-plane TEM lamellae from this region clearly reveal a network of dislocations (Fig. 5.6d-f), ranging from 125 to 582 nm in length with a non-uniform branching structure. The dislocation loops appear as dark contrasting regions and exhibit significant disorder, while the lighter surrounding material consists of highly-ordered [45] oriented rutile regions. The order-disorder morphology of the loops and their immediate surroundings suggests that the loop formation mechanisms may partly be associated with electronic energy losses.[48, 49]

In-plane TEM characterization revealed that the shape of the pristine material between dislocations is amebic and ~12 nm ± 4 nm in width, and are spaced 20-160 nm apart (Fig. 5.6d). In Region 2, the dislocations tend to form perpendicular to the highly stable {100} plane. Incoming Nb ions create a knock-on effect in the direction of irradiation causing dislocations to form in their path along the ⟨010⟩ direction. As Raman spectroscopy indicates, long-range order is maintained and so the {100} plane is unchanged with irradiation. Towards the peak of the SRIM calculated damage cascade, the microstructure transitions into Region 3.

Region 3 – Dislocation loops were observed in the same lace-like microstructure as in Region 2, but are instead oriented perpendicular to the ion beam direction, or along the {100} plane (viz. 90° change in orientation from the loops in Region 2). Region 3

overlaps with the SRIM-calculated Nb ion implantation peak and encompasses the irradiation damage peak. This peak dose is 23 dpa and is approximately a factor of two larger than the dose in Region 2, which can explain the increased density of dislocation loops in Region 3 as compared to that in Region 2. Because the implanted ions come to rest as interstitials, the material must accommodate the excess volume. It is therefore reasonable that interstitial agglomerations or loops would be oriented on the {100} habit plane, enabling accumulation of defects along the [100] direction.[66] This is because the atoms on the (100) plane tend to reconstruct when broken due to the high energy of the plane, causing the natural direction for growth and expansion in rutile TiO_2 to be in the [001] direction.

Region 4 – The final damage regime begins immediately beyond the Nb^+ implantation zone, then extends a further 500 nm into the substrate. The defects in this region are densely packed and comprised of nano-scale atomic rearrangements, maintaining the long-range crystalline ordering, as observed by SAED (Fig. 5.7b). While the presence of defects deeper than the irradiation damage and implantation peaks may initially seem unusual, it is likely that ionic channeling is occurring as the ion beam is aligned with a major symmetry direction. While some of the incoming Nb^+ ions interact with the specimen as modeled, a percentage of the ions do not come close enough to the atomic rows to cause scattering until farther along the ion trajectory. Similar results were shown by Weber et al. when comparing channeling to non-channeling orientations of SiC, whereas the channeling conditions experienced ionic penetration at much greater depths.[50]

5.4.3 Energy Deposition Mechanisms through Depth

The multi-layered defect structure, and the nature of these defects, can provide information about the unique energy loss mechanisms occurring at various depths.

Crystal reorientation in Region 1 may be attributed to ion channeling or one of several other mechanisms. Ion beam-induced or ion beam-assisted crystalline reorientation has been readily observed in a variety of materials, including transition metal ceramics[51-53], using ion beams as low as a few hundred eV.[53] The reorientation can be understood to be driven by the ion channeling mechanism.[53-57] However, other mechanisms such as sputtering, surface energy, and deformation energy, are also plausible and all lead to the same reorientation as channeling.[52] The reorientation is also influenced by factors such as ion energy, defect population, and system temperature.[57] It has also been shown that bombardment with noble metal ions (e.g. Nb used in this study) induces more extensive reorientation in ceramics than does bombardment with noble gas ions.[58]

In Region 2, defect formation is an effect of irradiation damage. However, irradiation damage induced by "intermediate" energy ions (i.e. within the range ~0.5-5.0 MeV) is not well understood. The intermediate energy range has been most extensively studied by Backman and co-workers[59,60] for Au ions incident on silica (SiO_2). Within this energy range, both nuclear and electronic stopping are important to the defect and microstructure evolution. Nuclear stopping is understood through binary collision approximation (BCA), while electronic stopping is understood through the inelastic thermal spike model.[61,62] The thermal spike model uses dense electronic excitations to transfer energy to the material through electron-phonon coupling, resulting in local

heating along the ion trajectory (which often culminates in the formation of visible ion tracks). Backman's results are noteworthy because they reveal that nuclear and electronic stopping exhibit a nonlinear synergy within the ion energy range of interest, resulting in a higher local defect density than would result from sequential evolution of atomic recoil processes and an inelastic thermal spike.[59,60] The synergistic effects of nuclear and electronic stopping have been described in the intermediate ion energy range in several ceramic systems.[63-66]

Although nuclear stopping is the dominant mechanism for defect creation for 3 MeV Nb ions, Backman's work implies that electronic stopping processes can also contribute to damage creation. This is consistent with the order-disorder morphology of the loops and their local surroundings in Region 2 – loops are created primarily by nuclear stopping event, but the disordering may partly be associated with inelastic thermal spike-type electronic stopping.[48]

Once the incident ion has lost its energy, it is likely that the microstructure evolution is influenced by the accumulation of defects in Region 3. As defects accumulate within Region 3, which corresponds to the peak of the calculated damage profile, the loop structures collapse along the (100) plane perpendicular to the ion beam. Because the ion fluence is not constant through the studied depth, it is worthwhile to consider the role of fluence on the microstructure evolution. Through Region 2, the fluence varies by approximately a factor of two, with a higher fluence occurring deeper into the material. While this factor is not sufficient to induce an entirely different microstructure, it could potentially explain the appearance of a slightly higher density of defects deeper into Region 2 than at the shallower portion of Region 2. The fluence peaks

within Region 3, which could explain the higher density of defects in Region 3 than in Region 2.

5.5 Conclusions

We examined the microstructure evolution of single crystal rutile TiO_2 irradiated with 3 MeV Nb^+ ions, in which the ions are incident on the {100} plane. Characterization by TEM revealed a complex microstructure evolution, marked by four distinct layers or regions of damage. The TEM results, together with XRD and Raman spectroscopy, help to understand the four-region structure. The regions contain: (1) near-surface short-range disorder, (2) dislocation loops parallel to the incident ion beam direction, (3) loops perpendicular to the incident ion beam direction, and (4) high-number density defects beyond the SRIM damage and implantation peaks.

The microstructures within each region are consistent with theories of varying irradiation damage mechanisms as a function of energy loss along the ion range. Ion-channeling-based damage is thought to account for crystallite reorientation and defect formation when the electronic stopping energy is high (i.e. near the surface of the specimen); this explains the formation of a high density of disorder in Region 1. When electronic stopping energy is lower, however (viz. deeper into the specimen), damage occurs primarily through nuclear stopping with a nonlinear synergetic effect from electronic stopping inducing additional disorder. Near and beyond the ion implantation peak, buildup of defects cause collapse of the dislocation loops in Region 3, while ionic channeling can account for the accumulation of damage in Region 4, beyond the SRIM calculated damage profile.

5.6 Figures and Tables

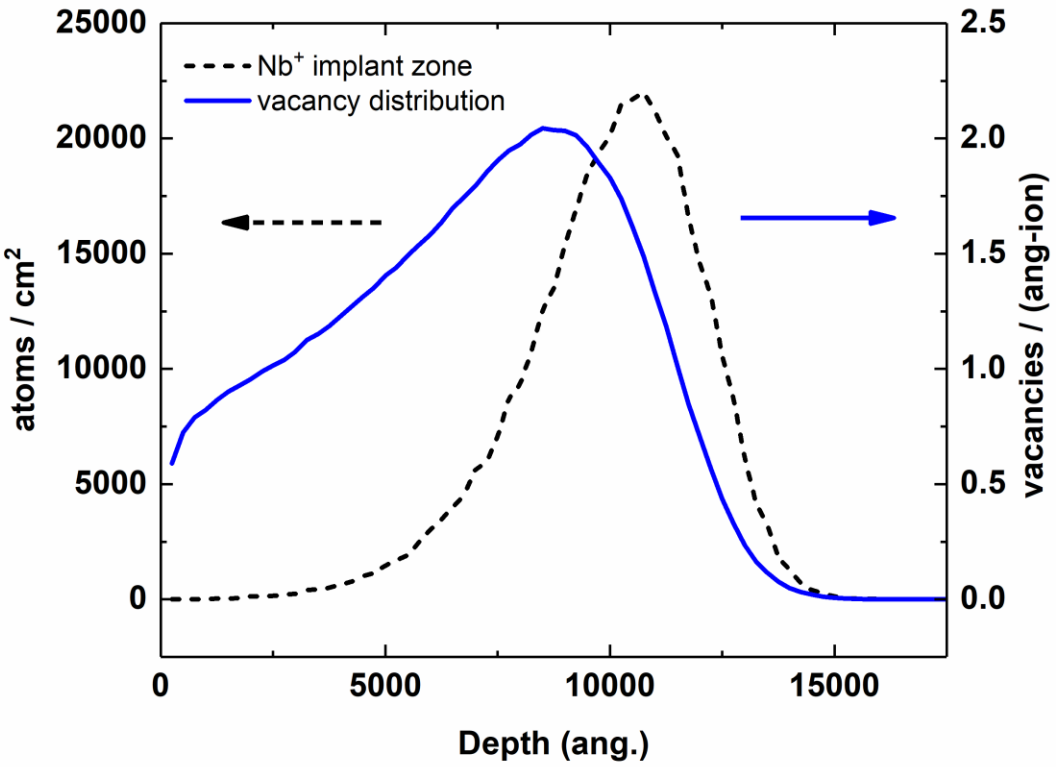

Figure 5.1: SRIM calculation of implanted Nb^+ ions (dashed line, left axis) and the resulting irradiation damage profile (solid line, right axis) for rutile TiO_2. *(J. Amer. Ceram. Soc.* 9 4357-4366, 2018)

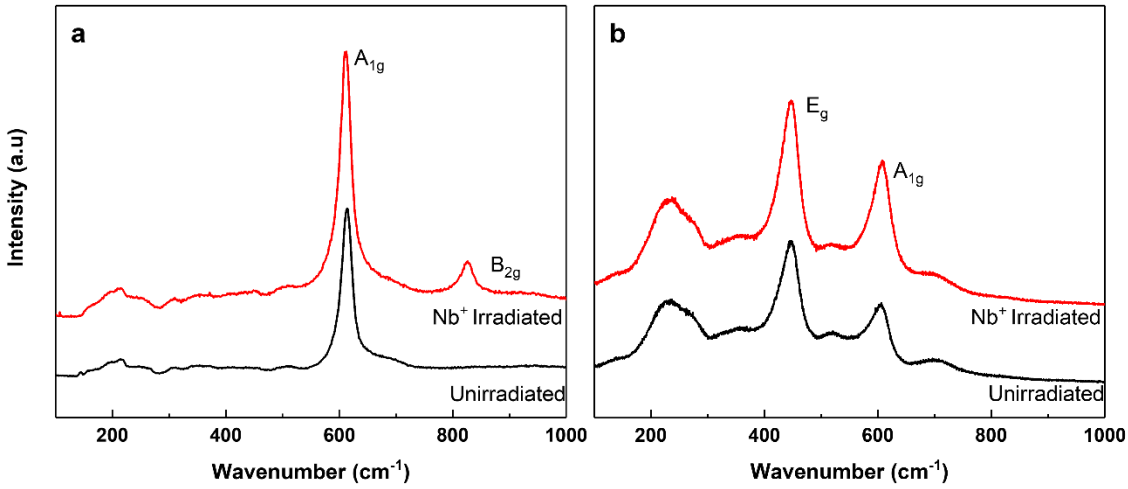

Figure 5.2: Raman spectra of non-irradiated rutile TiO_2 single crystal (black), and niobium-irradiated rutile single crystal (red) using a) 325 nm laser wavelength with ~ 10 nm sampling depth and b) 514.5 nm wavelength laser with ~ 1000 nm sampling depth. *(J. Amer. Ceram. Soc.* 9 4357-4366, 2018)

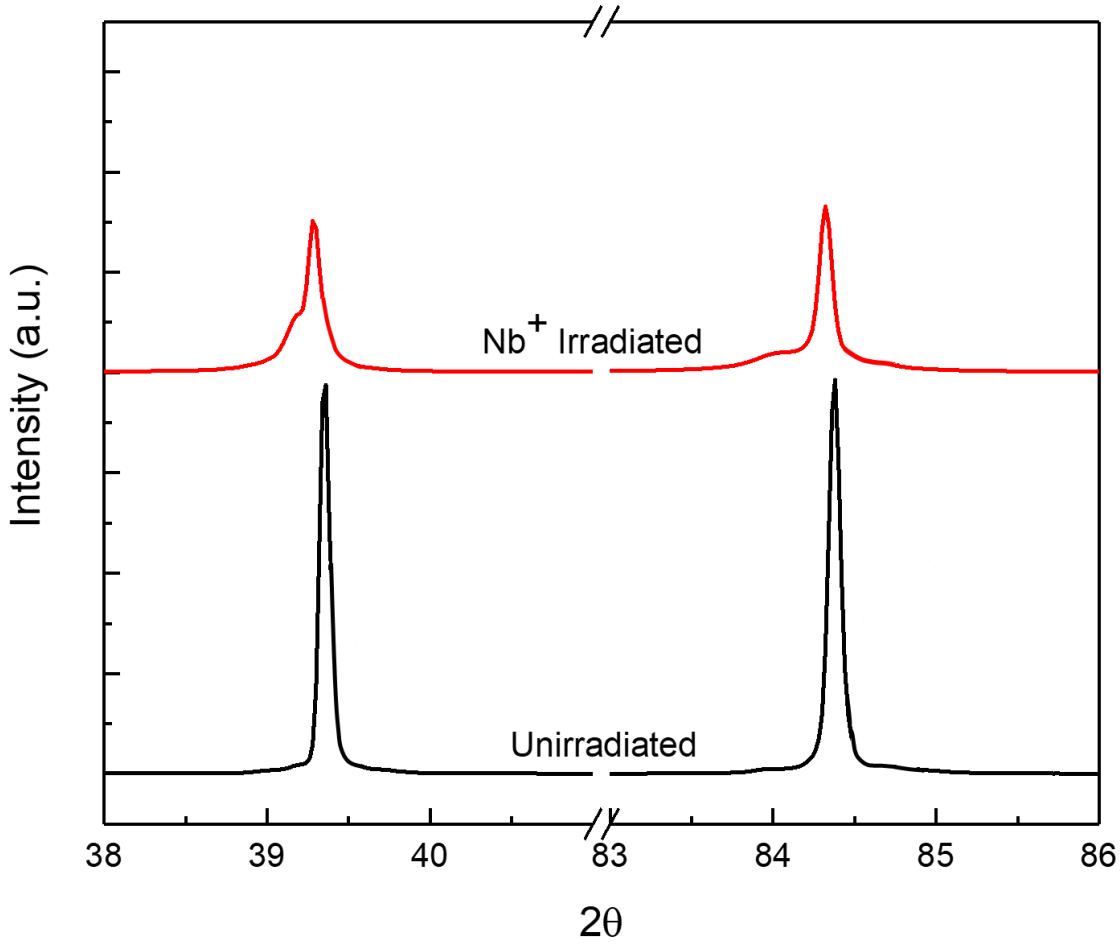

Figure 5.3: XRD spectra of non-irradiated rutile single crystal TiO_2 (black) and Nb^+ irradiated single crystal TiO_2 (red). *(J. Amer. Ceram. Soc.* 9 4357-4366, 2018)

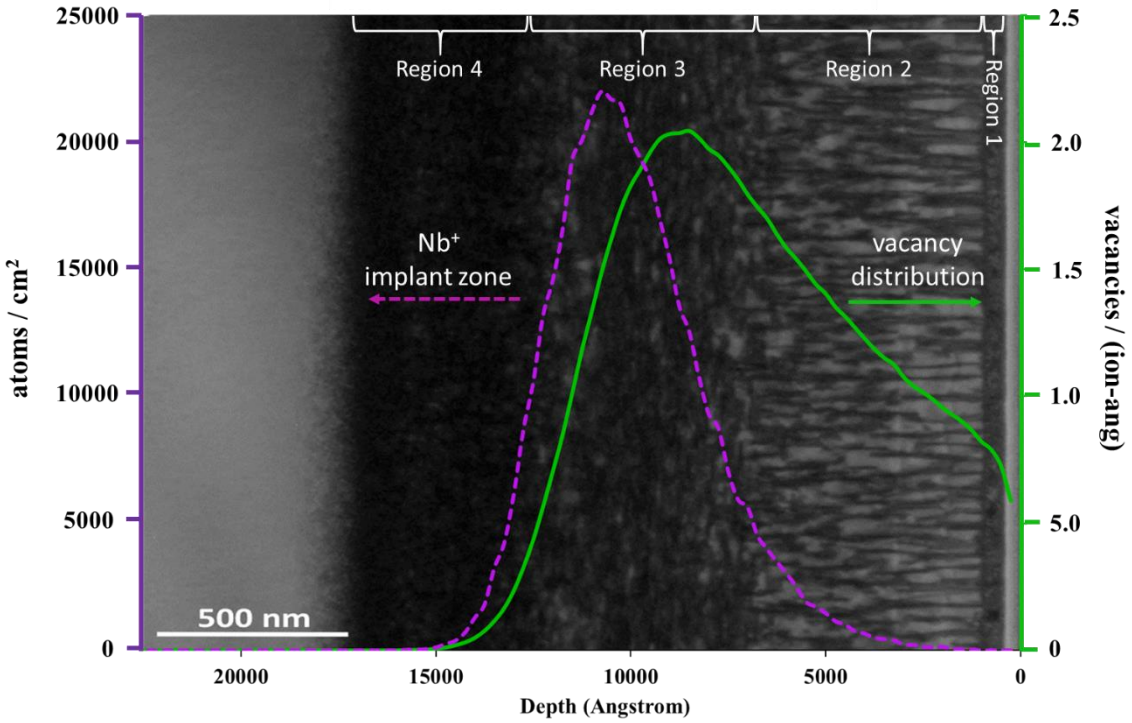

Figure 5.4: Cross-sectional TEM micrograph of four distinct damage regions created in rutile single crystal TiO_2, with SRIM calculated damage profile (solid) and Nb+ implantation profile (dashed) overlaid. *(J. Amer. Ceram. Soc.* 9 4357-4366, 2018)

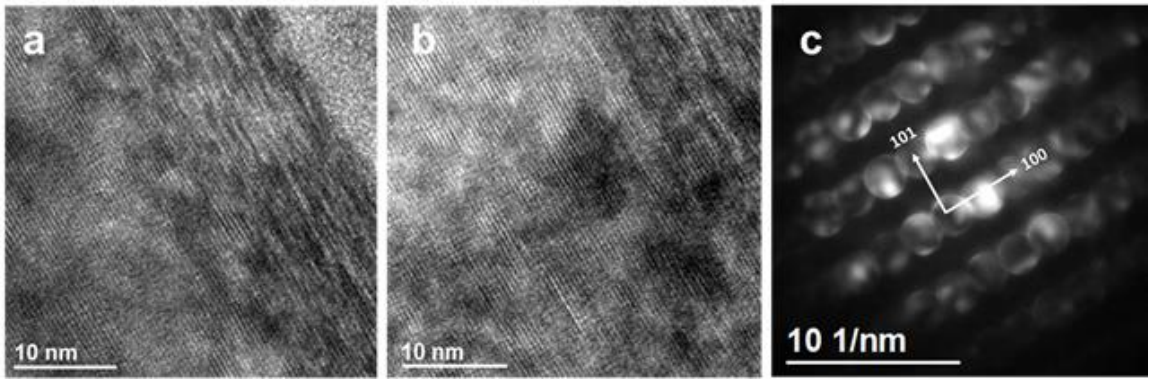

Figure 5.5 HR-TEM a) and b) of the damage Region 1 in Nb+ irradiated single crystal TiO_2, and c) corresponding CBED pattern. *(J. Amer. Ceram. Soc.* 9 4357-4366, 2018)

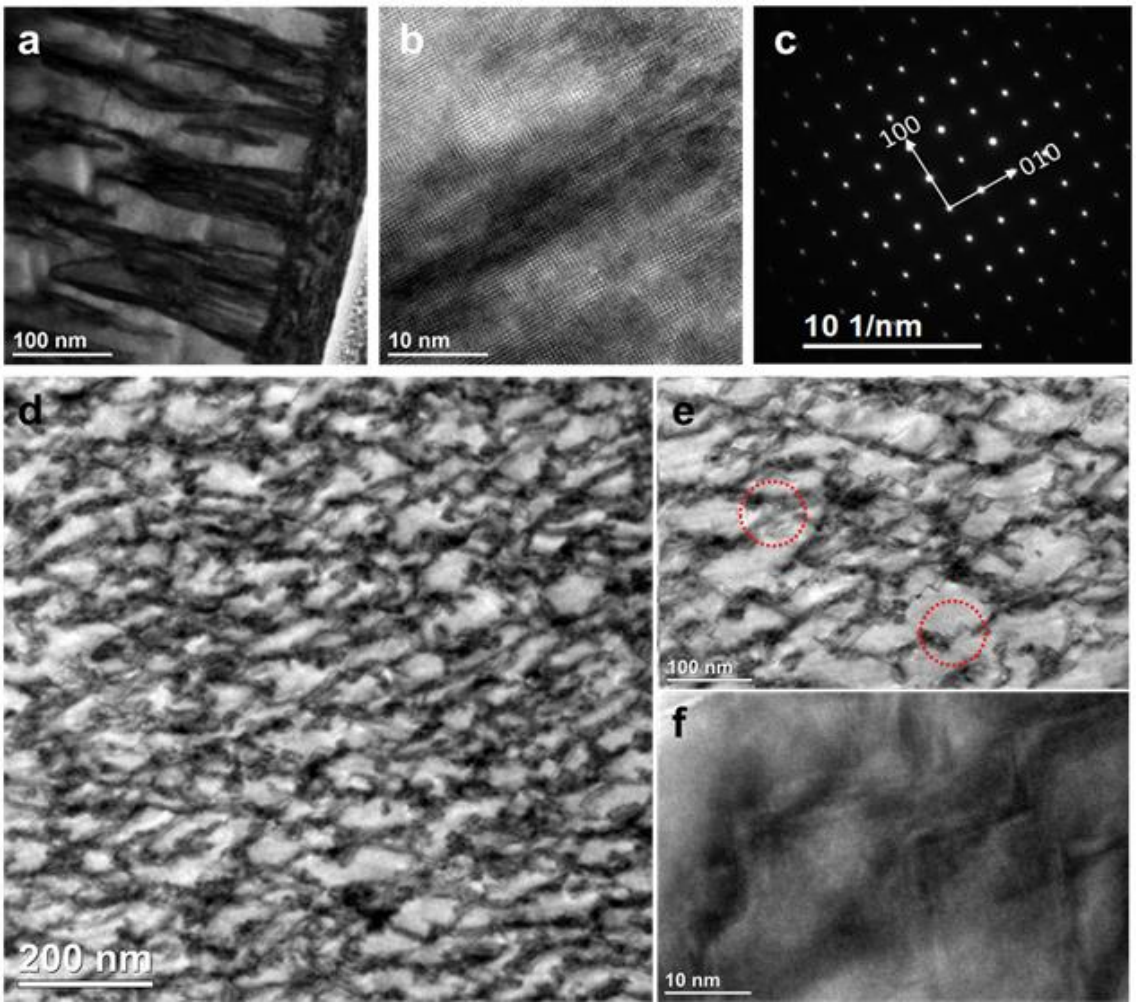

Figure 5.6: a) Bright field cross-sectional TEM of the transition between Region 1 and Region 2 of the irradiated single crystal, b) HR-TEM showing dislocations parallel to the ion beam direction, and c) corresponding SAED diffraction of Region 2. The in-plane TEM of Region 2 showing d) low magnification and e-f) high resolution TEM images of the defect regions. *(J. Amer. Ceram. Soc.* 9 4357-4366, 2018)

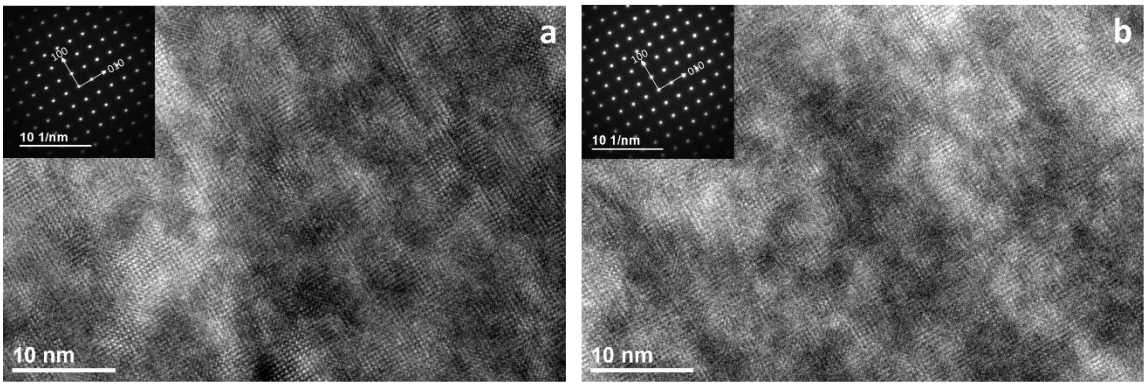

Figure 5.7: HR-TEM and corresponding SAED patterns from a) Region 3 and b) Region 4 of the Nb+ irradiated rutile single crystal TiO_2. *(J. Amer. Ceram. Soc. 9 4357-4366, 2018)*

5.7 References

1. A. J. Bard, *J. Phys. Chem.*, 1982, **86**, 172-177.
2. N. Serpone, D. Dondi and A. Albini, *Inorg. Chim. Acta*, 2007, **360**, 794-802.
3. N. Rahimi, R. A. Pax and E. M. Gray, *Prog. Solid State Chem.*, 2016, **44**, 86-105.
4. L.-Z. Qin, B. Liao, X.-L. Dong, X.-Y. Wu, X.-G. Hou and A.-D. Liu, *Nucl. Instrum. Methods Phys. Res., Sect. B*, 2009, **267**, 1077-1080.
5. S. K. Zheng, Wang, T. M., Wang, C., Xiang, G. , *Vacuum*, 2001, **65**, 155-159.
6. S. K. Zheng, Wang, T. M., Wang, C., Xiang, G. , *Nucl. Instrum. Methods Phys. Res., Sect. B*, 2002, **187**, 479-484.
7. J. Jensen, R. Sanz, D. Martin, A. Surpi, T. Kubart, M. Vázquez, M. Hernandez-Velez and I.-P. S. Africa, *Nucl. Instrum. Methods Phys. Res., Sect. B*, 2009, **267**, 2725-2730.
8. H. A. Shukur, M. Sato, I. Nakamura and I. Takano, *Adv. Mater. Sci. Eng.*, 2012, **2012**, 1-7.
9. R. Fernandes, N. Patel, R. Dholam, M. Adami and A. Miotello, *Surf. Coat. Technol.*, 2009, **203**, 2579-2583.
10. G. R. Lumpkin, K. L. Smith, M. G. Blackford, B. S. Thomas, K. R. Whittle, N. A. Marks and N. J. Zaluzec, *Phys. Rev. B: Condens. Matter*, 2008, **77**.

11. H. Rath, P. Dash, T. Som, P. V. Satyam, U. P. Singh, P. K. Kulriya, D. Kanjilal, D. K. Avasthi and N. C. Mishra, *J. Appl. Phys.*, 2009, **105**, 074311.

12. B. P. Uberuaga and X. M. Bai, *J. Phys.: Condens. Matter*, 2011, **23**.

13. M. J. Qin, E. Y. Kuo, K. R. Whittle, S. C. Middleburgh, M. Robinson, N. A. Marks and G. R. Lumpkin, *J. Phys.: Condens. Matter*, 2013, **25**, 355402.

14. F. Li, P. Lu and K. E. Sickafus, *J. Nucl. Mater.*, 2002, **306**, 121-125.

15. J. Zhang, J. Lian, F. Namavar, J. Wang, H. Haider, K. Garvin and R. C. Ewing, *J. Phys. Chem. C*, 2011, **115**, 22755-22760.

16. T. Hartmann, L. M. Wang, W. J. Weber, N. Yu, K. E. Sickafus, J. N. Mitchell, C. J. Wetteland, M. A. Nastasi, M. G. Hollander, N. P. Baker, C. R. Evans, J. R. Tesmer and C. J. Maggiore, *Nucl. Instrum. Methods Phys. Res., Sect. B*, 1998, **141**, 398-403.

17. K. A. Smith, A. I. Savva, C. J. Deng, J. P. Wharry, S. Hwang, D. Su, Y. Q. Wang, J. Gong, T. Xu, D. P. Buttf and H. Xiong, *J. Mater. Chem. A*, 2017, **5**, 11815-11824.

18. M. Z. S. Atashbar, H.T.; Gong, B.; Wlodarski, W.; Lamb, R. , *Thin Solid Films*, 1998, **326**, 238-244.

19. J. F. Baumard and E. Tani, *J. Chem. Phys.*, 1977, **67**, 857.

20. T.-F. Yi, Y. Xie, J. Shu, Z. Wang, C.-B. Yue, R.-S. Zhu and H.-B. Qiao, *J. Electrochem. Soc.*, 2011, **158**, A266.

21. C. P. Valentin, G.; Selloni, A., *Journal of Physical Chemistry C*, 2009, **113**, 20543–20552.

22. S. X. Zhang, D. C. Kundaliya, W. Yu, S. Dhar, S. Y. Young, L. G. Salamanca-Riba, S. B. Ogale, R. D. Vispute and T. Venkatesan, *J. Appl. Phys.*, 2007, **102**, 013701.

23. A. M. D. Ruiz, G.; Arbiol, J.; Cornet, A.; Morante, J.R., *Chem. Mater.*, 2004, **16**, 862-871.

24. J. Arbiol, J. Cerdà, G. Dezanneau, A. Cirera, F. Peiró, A. Cornet and J. R. Morante, *J. Appl. Phys.*, 2002, **92**, 853-861.

25. D. D. Morris, Y.; Rebane, J.; Mitchell, C.E.J.; Egdell, R.G., *Phys. Rev. B: Condens. Matter*, 2000, **61**.

26. R. E. Stoller, M. B. Toloczko, G. S. Was, A. G. Certain, S. Dwaraknath and F. A. Garner, *Nucl. Instrum. Methods Phys. Res., Sect. B*, 2013, **310**, 75-80.

27. J. F. Ziegler, 2013.

28. L. A. Giannuzzi and F. A. Stevie, Introduction to focused ion beams : instrumentation, theory, techniques, and practice, http://public.eblib.com/choice/publicfullrecord.aspx?p=226458).

29. C. M. Parish, K. G. Field, A. G. Certain and J. P. Wharry, *J. Mater. Res.*, 2015, **30**, 1275-1289.

30. R. S. Katiyar and R. S. Krishnan, *Phys. Lett. A*, 1967, **25**, 525-526.

31. B. Dayal, *Proc. Indian Acad. Sci.*, 1950, **Vol: 32A**, 304-312.

32. F. Matossi, *J. Chem. Phys.*, 1951, **19**, 1543-1546.

33. R. L. McCreery, *Raman spectroscopy for chemical analysis*, John Wiley & Sons, New York, 2000.

34. V. Swamy, B. C. Muddle and D. Qing, *Appl. Phys. Lett.*, 2006, **89**.

35. S. P. S. Porto, P. A. Fleury and T. C. Damen, *Phys. Rev.* , 1967, **154**, 522-526.

36. O. Frank, M. Zukalova, B. Laskova, J. Kürti, J. Koltai and L. Kavan, *Phys. Chem. Chem. Phys.*, 2012, **14**, 14567-14572.

37. J. Zhang, M. J. Li, Z. C. Feng, J. Chen and C. Li, *J. Phys. Chem. B*, 2006, **110**, 927-935.

38. U. Balachandran and N. G. Eror, *J. Solid State Chem.*, 1982, **42**, 276-282.

39. S. Zhou, K. Potzger, M. Krause, G. Talut, M. Helm, J. Fassbender, H. Schmidt, E. Cizmar, S. A. Zvyagin and J. Wosnitza, *Phys. Rev. B: Condens. Matter*, 2009, **79**.

40. Y. Zhang, C. X. Harris, P. Wallenmeyer, J. Murowchick and X. Chen, *J. Phys. Chem. C*, 2013, **117**, 24015-24022.

41. M. Ishimaru, Y. Hirotsu, F. Li and K. E. Sickafus, *Appl. Phys. Lett.*, 2000, **77**, 4151.

42. Y. Aoki, S. Yamamoto, H. Takeshita and H. Naramoto, *Nucl. Instrum. Methods Phys. Res., Sect. B*, 1998, **136**, 400-403.

43. F. Li, P. Lu, M. Ishimaru and K. Sickafus, *Philos. Mag. B*, 2000, **80**, 1947-1954.

44. F. Li, M. Ishimaru, P. Lu, I. V. Afanasyev-Charkin and K. E. Sickafus, *Nucl. Instrum. Methods Phys. Res., Sect. B*, 2000, **166-167**, 314-321.

45. F. X. Li, P. Lu, M. Ishimaru and K. E. Sickafus, *Philos. Mag. B*, 2000, **80**, 1947-1954.

46. K. Nomura, T. Nakanishi, Y. Nagasawa, Y. Ohki, K. Awazu, M. Fujimaki, N. Kobayashi, S. Ishii and K. Shima, *Phys. Rev. B: Condens. Matter*, 2003, **68**.

47. K.-i. Nomura, T. Nakanishi, Y. Nagasawa, Y. Ohki, K. Awazu, M. Fujimaki, N. Kobayashi, S. Ishii and K. Shima, *Phys. Rev. B: Condens. Matter*, 2003, **68**, 64106.

48. G. Bonfiglioli, A. Ferro and A. Mojoni, *J. Appl. Phys.*, 1963, **32**.

49. U. Diebold, *Surf. Sci. Rep.*, 2003, **48**, 53-229.

50. Y. W. Zhang, H. Z. Xue, E. Zarkadoula, R. Sachan, C. Ostrouchov, P. Liu, X. L. Wang, S. Zhang, T. S. Wang and W. J. Weber, *Curr. Opin. Solid State Mater. Sci.*, 2017, **21**, 285-298.

51. G. K. Wolf, *Surf. Coat. Technol.*, 1990, **43**, 920-935.

52. B. Rauschenbach and J. W. Gerlach, *Cryst. Res. Technol.*, 2000, **35**, 675-688.

53. C. H. Ma, J. H. Huang and H. Chen, *Thin Solid Films*, 2004, **446**, 184-193.

54. B. Holzapfel and V. Betz, *IEEE Trans. Appl. Supercond.*, 1999, **9**.

55. G. N. Van Wyk and H. J. Smith, *Radiat Eff. Defects Solids*, 1978, **38**, 245-247.

56. G. N. Van Wyk, *Radiat Eff. Defects Solids*, 2011, **57**, 45-50.

57. G. Carter, *Phys. Rev. B*, 2000, **62**, 8376-8390.

58. G. N. Van Wyk, *Radiat Eff. Defects Solids*, 2006, **57**, 187-192.

59. M. Backman, F. Djurabekova, O. H. Pakarinen, K. Nordlund, Y. Zhang, M. Toulemonde and W. J. Weber, *Nucl. Instrum. Methods Phys. Res., Sect. B*, 2013, **303**, 129-132.

60. M. Backman, F. Djurabekova, O. H. Pakarinen, K. Nordlund, Y. Zhang, M. Toulemonde and W. J. Weber, *J. Phys. D: Appl. Phys.*, 2012, **45**.

61. M. Toulemonde, C. Dufour, A. Meftah and E. Paumier, *Nucl. Instrum. Methods Phys. Res., Sect. B*, 2000, **166-167**, 903-912.

62. M. Toulemonde, C. Dufour and E. Paumier, *Phys. Rev. B: Condens. Matter*, 1992, **46**, 14362-14369.

63. E. Zarkadoula, H. Xue, Y. Zhang and W. J. Weber, *Scripta Mater.*, 2016, **110**, 2-5.

64. M. C. Ridgway, F. Djurabekova and K. Nordlund, *Curr. Opin. Solid State Mater. Sci.*, 2015, **19**, 29-38.

65. W. Weber and O. R. T. N. Oak Ridge National Laboratory, *Acta Mater.*, 2016, **105**, p. 429-437.

66. W. J. Weber, D. M. Duffy, L. Thomé and Y. Zhang, *Curr. Opin. Solid State Mater. Sci.*, 2015, **19**, 1-11.

CONCLUSIONS

Ion irradiation produces a range of phenomena in TiO_2, which alters charge storage behavior when used as an electrode in lithium ion batteries. Chapter Two discussed the study of defects generated by heat treatment which show that oxygen and titanium vacancies can be generated in TiO_2 nanotubes by annealing under oxygen-deficient (Ar and N_2) and water vapor atmospheres. The presence of oxygen vacancies increase the electrical conductivity of the electrodes while Ti vacancies result in a slight decrease of conductivity. The Ar- and N_2-treated samples have an increase in capacity by 10% and 25%, respectively, while the water vapor treatment results in a 24% capacity increase. The results of increased capacity even with reduced electrical conductivity suggests that electrical conductivity may not be the most significant indicator as to whether battery performance can be improved.

Chapter Three shows that phase transformations occur in amorphous TiO_2 when irradiated with protons at both room and elevated temperatures. Raman spectroscopy and TEM indicate that under room temperature irradiation, short-range-ordered crystallites were observed and the final structure is a mixture of anatase, amorphous and rutile domains while high temperature proton implantation results in a phase transformation from amorphous to a primarily disordered rutile phase. The room temperature irradiated samples exhibit reduced capacity, possibly due to the combination of anatase, rutile and amorphous phases present resulting in reduced ion mobility. On the other hand, in the high temperature exhibits improved capacity due to the disordered rutile structure. GITT

results suggest that Li^+ diffusivity in the high temperature irradiated sample is higher than that of the room temperature irradiated sample, which is further confirmed by the enhanced rate capability of the high temperature irradiated sample.

Chapter Four discusses the changes in anatase nanotube electrodes under similar irradiation conditions. While Raman and XRD show that the overall crystallinity of the nanotubes are maintained, electrochemical testing exhibits distinct increases to the electrochemical charge storage behavior of anatase when irradiated with protons at high room temperature and elevated temperatures. Electrochemical impedance spectroscopy shows that of the three conditions, the non-irradiated nanotubes exhibit the highest charge transfer resistance, follows by the room temperature irradiated, whereas the high temperature irradiation has the lowest. Furthermore, lithium diffusivity is highest in the high temperature irradiated sample. The generation defects by irradiation results in a 33% and 47% increase in specific capacity to the room temperature and elevated temperature proton irradiated samples, respectively.

Finally, we evaluated the microstructural evolution of single crystal rutile TiO_2 during irradiation with 3 MeV Nb^+ ions. TEM revealed a complex microstructure, with four distinct layers of damage. The regions contain: (1) near-surface short-range disorder, (2) dislocation loops parallel to the incident ion beam direction, (3) loops perpendicular to the incident ion beam direction, and (4) high-number density defects beyond the SRIM damage and implantation peaks. Ion-channeling-based damage is thought to account for crystallite reorientation and defect formation near the surface of the specimen. When electronic stopping energy is lower damage occurs primarily through nuclear stopping with a nonlinear synergetic effect from electronic stopping inducing additional disorder.

Near and beyond the ion implantation peak, buildup of defects cause collapse of the dislocation loops.

Overall, the study of how irradiation effects electrochemical behavior of TiO_2 for use in lithium ion batteries is non-trivial. With this study, we have broadened the field of knowledge on how both polycrystalline and single-crystal metallic oxide materials react in irradiation environments. Nanostructures provide a unique challenge in that they have many defect sinks, and so by including single crystals we are better able to see how irradiation promotes defects in these oxides. Furthermore, we were able to distinguish how irradiation may promote defects within metallic oxides, specifically TiO_2, which lead to enhanced charge storage capabilities.